

**Investigation of Enhancing Drill Cuttings Cleaning and Penetration Rate Using
Cavitating Pressure Pulses**

By

© Sadegh Babapour

A Thesis submitted to the

School of Graduate Studies

in partial fulfillment of the requirements for the degree of

Master of Engineering

Faculty of Engineering and Applied Science

Memorial University of Newfoundland

May, 2014

St. John's

Newfoundland

ABSTRACT

Drilling efficiency is governed by rock cuttings removal by hydraulic forces. The mechanical force introduced by the drill bit removes the rock chips from the parent rock. The chips will be held down until the downward forces due to overburden pressure are overcome. The turbulent jet that flushes away these chips consists of static impingement and dynamic pressure fluctuations. Instead of providing high pressure and hence enhancing the pressure fluctuations of the turbulent jet by rig pumps, the existing fluid pressure can be used more effectively.

A fluid passing a Convergent-Divergent venturi demonstrates significant pressure fluctuations due to the cavitation phenomenon. As the fluid passes the vena-contracta, according to the Bernoulli's principle, the fluid velocity increases and hence the pressure decreases. If pressure drops below the fluid vapor pressure, cavitation occurs and bubbles are created.

Different prototypes were designed to investigate the probability of cavitation occurrence by using CFD simulations. The successful designs were venturis with diameters of 4 mm and 12 mm. Simulation software applies tetrahedral meshing to the prototype geometry for robust simulation results when geometry of the tool is complex. The results obtained confirmed the pressure pulses and occurrence of cavitation.

An experimental setup consisting of a 12 mm venturi, two pressure sensors at upstream and downstream, and 3 load cells in a triangular combination, and a flow meter was used. The flow rate range was from 10 USGPM to 70 USGPM. The cavitation started at 25 USGPM with a shear noise that is the characteristics of a

cavitating flow and the sensors recorded the pressure pulses at this point. The magnitude of pressure peaks ranged from 150 psi up to 600 psi.

The second stage of the experiments was to investigate the effect of venturi and axial compliance in drilling. Compliant element used in these experiments consists of two plates with rubber mounts embedded between these two plates in an equilateral configuration. The rubber mounts enable the displacement of the upper plate on the base plate. An 8 mm venturi was also mounted on the drill string behind the bit as the vibration source.

The experimental results show that the tool starts to cavitate and produce vibrations. The tool was tested with compliance and without compliance to seek the effects of the compliant element. Results show that when rigid (no compliance), the vibrations produced, did not have any significant effect on the rate of penetration (ROP). However, with integration of the compliant element, the vibrations produced by the tool intensified the natural vibration of the compliant element and the penetration rate increased.

ACKNOWLEDGEMENTS

First and foremost, my sincerest gratitude must go to my supervisor, Dr. S. D. Butt for funding my research, and his invaluable and constructive support in all stages of this thesis. I would also like to thank him for his insightful comments and suggestions which aided me to shape my interests and ideas.

Furthermore, I would also like to thank our project manager, Farid Arvani and project engineer, Brock Gillis, for their technical assistance in preparing and conducting my experiments.

I wish to thank my fellow members of the Advanced Drilling Group (ADG) who were involved in my experiments. Special thanks to Olsekii Pronin for his assistance introducing the pulse-cavitation subject. I would also like to express my deepest appreciation to my friends, Yousef Gharibi, Mohammad Mozaffari, Ahmed Elnahas, Pushpinder Rana and all the other members of ADG.

Last but not the least; I owe a very important debt to my family for their support and encouragement.

This research was conducted at the Advanced Drilling Group laboratory of Memorial University of Newfoundland and was funded by the Atlantic Canada Opportunities Agency (AIF contract No. 781-2636-1920044), Husky Energy, Suncor Energy, and Research and Development Corporation of Newfoundland and Labrador.

Table of Contents

ABSTRACT.....	ii
ACKNOWLEDGEMENTS.....	iv
Table of Contents.....	v
List of Tables.....	viii
List of Figures.....	ix
List of Symbols, Nomenclature and Abbreviations.....	xvi
List of Appendices.....	xix
1. Introduction.....	1
1.1 Introduction to oilfield drilling operations.....	1
1.2 Research scope and objective.....	3
1.3 Significance of Research.....	4
1.4 Thesis Outline.....	5
2. Literature Review.....	7
2.1 Characteristics of the cavitation phenomenon.....	7
2.1.1 Introduction to cavitation.....	7
2.1.2 Types of cavitation in hydrodynamics.....	9
2.1.3 Factors affecting the formation of cavitation.....	10
2.1.4 The effects of cavitation.....	10
2.1.5 Cavitation number.....	11

2.1.6 Vapor Pressure	13
2.2 Principles of Bernoulli's Equation	15
2.2.1 Bernoulli's Equation derivation	15
2.2.2 Physical interpretation of Bernoulli's Equation	18
2.3 Periodic Cavitation shedding in a cylindrical orifice	19
2.3.1 Introduction to different cavitation patterns	19
2.3.2 Periodic cloud cavity	25
2.3.3 Measurements of spray angle variation with cavitation	27
2.4 Development and testing of a Polycrystalline Diamond Compact (PDC) bit with passively-pulsating cavitating nozzles	29
2.5 Cavitation damage to geomaterials in a flowing system	33
2.6 Summary of literature review	37
3. CFD Simulations	38
3.1 Summary of CFD method	38
3.2 Simulation results of the 4 mm venturi	40
3.3 Simulations results of the 12 mm venturi	46
3.4 8 mm venturi insert in drill pipe simulation	56
4. Pulse Cavitation Tool Experiments	68
4.1 Testing setup description	68
4.2 Data Acquisition (DAQ) System	70
4.3 Sensors	71

4.4 Experiments plan and results	72
4.5 Cavitation pitting	90
5. Drilling Experiments.....	91
5.1 Experimental setup description.....	91
5.2 Compliance	96
5.3 Experiments Procedure	97
5.4 Drilling experiments results.....	99
5.5 Effect of compliance	113
6. Conclusions.....	124
6.1 Summary of pulse cavitation simulations and flow tests.....	124
6.2 Drilling experiments and axial compliance	125
Bibliography	128
Appendix A.....	133
Appendix B	134
Appendix C	135
Appendix D.....	136

List of Tables

Table 1. 4 mm venturi experiments plan.	73
Table 2. 12 mm venturi experiments plan.	74
Table 3. Drill pipe drilling plan	98
Table 4. 8 mm venturi drilling plan	98
Table 5. Drill pipe bit pressure drop.	108
Table 6. Venturi insert bit pressure drops.	108

List of Figures

Figure 1. Phase diagram of water presenting boiling and cavitation process [8]. ...	7
Figure 2. Fixed and detached cavity in vena contracta [9].	9
Figure 3. Streamline pressure drop behavior in an orifice [10].	12
Figure 4. Phase diagram presenting vapor pressure [11].	13
Figure 5. Schematics of an arbitrary conduit with flow rate Q [12].	15
Figure 6. Schematic of venturi.	19
Figure 7. Flow behavior in venturi with different cavitation numbers [15].	21
Figure 8. Schematics of the orifice inside the pressure vessel [7].	22
Figure 9. Classification of different flow behavior and the relevant fixed cavity length [15].	23
Figure 10. Flow behavior at the outlet of the nozzle with increasing fixed cavity length [16].	24
Figure 11. Schematics of the shedding phenomenon inside the nozzle [7].	25
Figure 12. Sequence of bubbles cluster shedding [7].	26
Figure 13. Spray angle variation with cavitation number [15].	27
Figure 14. Half-spray angle relationship with cavitation number [7].	28
Figure 15. Comparison of non-cavitating and cavitating jet [18].	30
Figure 16. Passively pulsating nozzle schematics [17].	31
Figure 17. ROP versus WOB for Crab Orchard Sandstone [17].	32
Figure 18. ROP versus WOB for Sierra White Granite [17].	33
Figure 19. Different zones under cavitating jet impact [22].	35

Figure 20. Sequence of cavitation bubbles damage on rock surface [23].....	36
Figure 21. Schematics of 4 mm venturi.	39
Figure 22. Schematics of the main housing for venturis in the assembly.....	39
Figure 23. Exploded view of the assembly.	40
Figure 24. View of imported model into Flow3D simulation.	40
Figure 25. 2D presentation of fluid passing venturi and initiation of bubbles growth.	41
Figure 26. Fixed and detached cavity clouds in Flow3D.....	42
Figure 27. Detached cavity clusters travel along the pipe.	43
Figure 28. Pressure peaks and flow pressure behavior at different locations after venturi.	45
Figure 29. Schematics of 12 mm venturi.	46
Figure 30. Particle tracing (representing flow streamlines) in simulated control volume.....	47
Figure 31. Tetrahedral meshing of the assembly.	49
Figure 32. VOF results of the simulation presenting liquid vapor after venturi. ...	50
Figure 33. Front view of the tool outlet with pressure contours.....	51
Figure 34. 2D representation of Cavitation vapor volume fraction inside 12 mm venturi.	51
Figure 35. Fixed cavity growth inside 12 mm venturi represented with CVF.....	52
Figure 36. Pressure recorded with probe at k=250 after venturi.....	53
Figure 37. CVF presentation of flow at k=302.	54
Figure 38. Density of the flow at k=302.	55
Figure 39. Velocity magnitude of the flow at K=302.....	56

Figure 40. Exploded View of the venturi insert for drilling setup.	57
Figure 41. Dimension of 8 mm venturi.	57
Figure 42. Cavitation initiation in 8 mm venturi throat section.	58
Figure 43. Bubble cluster detached from venturi throat, exiting venturi.	59
Figure 44. Cavity clusters exiting the venturi after shedding presented by VOF. .	60
Figure 45. Vapory texture of the flow after venturi.	61
Figure 46. Fluid velocity profile	62
Figure 47. Pressure fluctuations of the fluid at $k=150$	62
Figure 48. Venturi pressure profile along tool length.	63
Figure 49. Fluid density after venturi during simulation time.	64
Figure 50. Cavitation vapor volume fraction of the fluid after venturi.	64
Figure 51. 3D representation of the cavitation clusters with pressure contours in 8 mm venturi.	65
Figure 52. Pressure probe fluctuation at $k=27$ after venturi during 21 s simulation.	66
Figure 53. Test frame components.	68
Figure 54. Test frame piping section.	69
Figure 55. Restriction plate schematics.	70
Figure 56. Mobile DAQ system and its power supply.	71
Figure 57. Triangular configuration for load cells.	72
Figure 58. Outlet pressure of 12 mm venturi at 8 USGPM.	75
Figure 59. Outlet pressure of 12 mm venturi at 12 USGPM.	76
Figure 60. Outlet pressure of 12 mm venturi at 15 USGPM.	76
Figure 61. Outlet pressure of 12 mm venturi at 20 USGPM.	77

Figure 62. Outlet pressure of 12 mm venturi at 23 USGPM.	77
Figure 63. Outlet pressure of 12 mm venturi at 26 USGPM.	78
Figure 64. Outlet pressure of 12 mm venturi at 30 USGPM.	79
Figure 65. Outlet pressure of 12 mm venturi at 33 USGPM.	79
Figure 66. Outlet pressure of 12 mm venturi at 37 USGPM.	80
Figure 67. Outlet pressure of 12 mm venturi at 40 USGPM.	80
Figure 68. Comparison of pressure pulses amplitude at different flow rates during cavitation.	81
Figure 69. Comparison of outlet pressure with and without cavitation.	82
Figure 70. Outlet pressure of 12 mm venturi at 30 USGPM with 200 psi back pressure.	83
Figure 71. Comparison of outlet pressure at 30 USGPM without back pressure and with back pressure.	84
Figure 72. Outlet pressure of 4 mm venturi at 6.5 USGPM.	84
Figure 73. Outlet pressure of 12 mm venturi at 50 USGPM.	85
Figure 74. Outlet pressure of 12 mm venturi at 60 USGPM.	86
Figure 75. Outlet pressure of tool with no venturi at 50 USGPM.	86
Figure 76. Outlet pressure of tool with no venturi at 60 USGPM.	87
Figure 77. Schematics of a nozzle flow acting on a plate [29].	87
Figure 78. Load cell 1 data of 12 mm venturi at 60 USGPM.	88
Figure 79. Load cell 2 data of 12 mm venturi at 60 USGPM.	89
Figure 80. Load cell 3 data of 12 mm venturi at 60 USGPM.	89
Figure 81. Different views of the eroded regions of the restrictor plate.	90
Figure 82. SSDS-I Drill rig components.	92

Figure 83. Inside view of the pressure cell with synthetic rock sample secured with rock holding disk [31].	93
Figure 84. 2-cutter PDC bit & nozzle schematics [31].	93
Figure 85. Location of LVDT measuring bit travel and suspended weight.	94
Figure 86. Drill cuttings filter [31].	95
Figure 87. Different sections of the compliant element for SSDS-I setup.	96
Figure 88. ROP for venturi with and without compliant element at different flow rates.	100
Figure 89. MSE for venturi with and without compliant element at different flow rates.	100
Figure 90. ROP for drill pipe with and without compliant element at different flow rates.	101
Figure 91. MSE for drill pipe with and without compliant element at different flow rates.	101
Figure 92. ROP for venturi with and without compliant element at different flow rates at low WOB.	102
Figure 93. MSE for venturi with and without compliant element at different flow rates at low WOB.	103
Figure 94. ROP for venturi with and without the compliant element at 300 psi back pressure.	104
Figure 95. MSE for venturi with and without the compliant element at 300 psi back pressure.	104
Figure 96. ROP for drill pipe with and without the compliant element at 300 psi back pressure.	105

Figure 97. MSE for drill pipe with and without the compliant element at 300 psi back pressure.....	106
Figure 98. ROP comparison of venturi and drill pipe at 300 psi back pressure at high flow rates.....	106
Figure 99. ROP of venturi versus drill pipe at high WOB with compliance.	107
Figure 100. MSE of venturi versus drill pipe at high WOB with compliance.....	107
Figure 101. Bit pressure drop comparison.	109
Figure 102. Drill pipe bit pressure drop and system pressure losses.	110
Figure 103. Venturi insert pressure drops.....	110
Figure 104. HSI versus Flow rate.	111
Figure 105. Drill pipe pressure pattern versus flow level.	112
Figure 106. Venturi insert pressure pattern versus flow level.	112
Figure 107. Applied load versus displacement of compliant element.	114
Figure 108. WOB and displacement before and while drilling.	115
Figure 109. ROP of venturi insert with and without compliance.	116
Figure 110. MSE of venturi insert with and without compliance.....	116
Figure 111. WOB comparison at 18.5 USGPM.	117
Figure 112. WOB comparison at 22.6 USGPM.	118
Figure 113. Displacement FFT at 18.6 USGPM with and without compliance..	119
Figure 114. WOB FFT at 18.6 USGPM with and without compliance.....	119
Figure 115. FFT analysis of load of drill pipe at 88 and 71 ft/hr.....	120
Figure 116. FFT analysis of compliance displacement at 88 and 71 ft/hr.	121
Figure 117. FFT analysis of load of venturi insert at 88 and 71 ft/hr.	121

Figure 118. FFT analysis of compliance displacement of venturi insert at 88 and
71 ft/hr..... 122

List of Symbols, Nomenclature and Abbreviations

ROP	Rate of Penetration
UBD	Under Balanced Drilling
PDC	Polycrystalline Diamond Compact
MSE	Mechanical Specific Energy
WOB	Weight On Bit
USGPM	U.S. Gallons Per Minute
RPM	Revolution Per Minute
ρ	Density
g	Gravity
BHA	Bottom Hole Assembly
CFD	Computational Fluid Dynamics
TVD	True Vertical Depth
OBD	Over Balanced Drilling
C	Critical Point
P_1	Inlet Pressure
P_v	Vapor Pressure

P_2	Outlet Pressure
K	Cavitation Number
K_i	Cavitation Inception Number
V	Fluid Velocity
T_r	Triple Point
Q	Flow Rate
A	Area
m	Mass
UCS	Unconfined Compressive Strength
θ	Half Spray Angle of Jet
Re	Reynolds Number
W	Work
E	Total Mechanical Energy
y	Height
Δt	Time
L	Orifice Length
D	Orifice Diameter

PDE	Partial Differential Equation
FVM	Finite Volume Method
CV	Control Volume
CC	Cell Centered Control Volume
VC	Vertex Centered Control Volume
CAD	Computer Assisted Drawing
B.C	Boundary Condition
VOF	Volume of Fluid
CVF	Cavitation Vapor Volume Fraction
F	Force
LVDT	Linear Variable Displacement Transducer
N	Bit Revolution
T	Torque
FFT	Fast Fourier Transform

List of Appendices

Appendix A: 4 mm venturi drawing

Appendix B: 12 mm venturi drawing

Appendix C: 8 mm venturi drawing

Appendix D: Drill bit nozzle drawing

1. Introduction

1.1 Introduction to oilfield drilling operations

Original drilling techniques used to explore for oil and gas were based on the ancient methods used to find water. The need for more energy resulted in exploring in the harshest environments, and deepest depth that was not practical before. This led to numerous developments in technology which would overcome these barriers and facilitate extraction of crude oil from petroleum reservoirs in deep water and also in harsh environments of the Arctic [1].

Drilling is a costly operation and oil and gas companies always try to optimize the drilling process. If the operation is in its optimum condition, it means faster drilling or minimum cost. Drilling time consists of two tasks. The major part is when drilling is proceeding and the drill bit is penetrating the rock and moving forward. The second part is the time required to pull the drill string out of the hole to change the bit or Bottom Hole Assembly (BHA); this time cannot be reduced due to the requirements and the nature of the operation. This means that, the efforts to reduce drilling time and save costs is solely achieved by reducing the time when the bit is penetrating the formation and hence increasing the rate of penetration ROP [2].

Many investigators have been working on increasing ROP, using different tools and different methods. Conventional drilling utilizes mud densities which would provide hydrodynamic pressure higher than the pore pressure, also known as the Over Balanced Drilling (OBD). New techniques in which the bottom hole pressure is

slightly lower than the pore pressure also known as Under Balanced Drilling (UBD) are also in use, but they also have their own difficulties [3].

There are some tools that promise increase in ROP that are compatible with conventional drilling operation. Many different tools and mechanisms are suggested such as applying a static Weight on Bit (WOB) with an oscillatory dynamic WOB, to utilize these vibrations to penetrate rocks more effectively.

Other tools focus on the drilling fluids and bit nozzles. The idea behind these tools is to increase the bottom hole cleaning efficiency and reduce the forces that push down the drill cuttings known as chip hold down effect. Higher jet velocity gives higher lift forces which could flush larger cutting chips, which would need to be reground and become smaller in case of relatively low jet velocities [4].

1.2 Research scope and objective

From the early stages of drilling, one of the main goals was to increase the rate of penetration (ROP), in order to reach reservoir sources more rapidly and reduce the heavily costs. Many attempts have been conducted to solve this issue by introducing new tools and techniques to bring new dimensions to the conventional drilling such as introducing vibratory tools, UBD and increasing cleaning efficiency by modifying nozzle geometry, percussion drilling, etc.

One of the promising techniques is to apply pressure pulsations and hence, oscillatory forces to the bit, hence the bit can vibrate and penetrate rock material faster. Another aspect of this method was to solely take advantage of the nature of pressure pulsations. The pulsating mud jet would have higher and better impact on the rock and assist the bit in penetrating. The pulsating jet also increases the cleaning efficiency of the bit by introducing high lifting forces that would flush larger cutting sizes. This eliminates the time required for the cuttings to be reground until they would be small enough to be lifted up by the fluid moving upward in the annulus [5].

Pulse-cavitation is a tool that is capable of turning a steady state flow into a pulsating flow field by introducing cavitation into the flow system. The other advantage of this tool is that a portion of liquid changes into vapor, and flow after the venturi is basically a two phase flow with a density lower than the liquid entering the venturi resulting in higher jet velocities. Also, direct collapse of cavity bubbles over time will reduce rock resistance and hence increase the ROP.

In this investigation, two different prototypes were used in order to investigate the proper candidates for a pulse-cavitation tool. Two different sets of experiments with

high and low flow rates were conducted. Prior to prototype manufacture, comprehensive simulations were conducted with different Computational Fluid Dynamics (CFD) software packages to predict that the optimum results will be achieved. Flow rate, pressure and force were measured before and after the tool to study the venturi effect.

1.3 Significance of Research

Research confirms that as the true vertical depth (TVD) increases, the rate at which the bit penetrates the rock and moves forward decreases [2]. As a result, researchers are investigating to overcome the barriers on increasing ROP due to increase in depth.

Cavitation phenomenon is known to have undesirable effects such as damaging pumps, eroding valves, metal pitting, noise and vibration introduced to the hydraulic system [4]. However, this phenomenon due to its high energy nature can be utilized in rock drilling to enhance ROP. Although the collapse of a cavity cloud is relatively low energy event, localized collapses on material surface can cause significant damage, such as eroding hard steels, a phenomenon known as cavitation pitting [6].

This study aimed to develop a prototype that could be used in field and laboratory scales to utilize the pressure pulsations, and hence the forced vibration introduced to the bit. The enhanced jet velocities also improve cleaning efficiency. Another advantage of cavitating flow is its erosive nature. Collapses of cavity clouds on rock surfaces introduce new cracks or extend the in-situ cracks and assist in easier rock deformation and also save bit life.

Finally, the effect of a cavitation in drilling operation was investigated by conducting a multitude of drilling tests with varying flow rates. Penetration rates were compared when the flow was single phase with no cavitation with the cavitating flow. This helped in analyzing the effect of cavitation bubbles in drilling.

Cavitation venturi and the produced pressure fluctuations were the source of vibration. A compliant element was included in the drill rig to see the effects of vibration with and without conversion of oscillatory forces to displacement. This was conducted to validate the simulation results from previous works done on investigating a compliant element effect.

1.4 Thesis Outline

In chapter two the basic concepts of cavitation phenomenon and the related properties of a cavitating flow are discussed. The relationship between pressure and the velocity of the fluid is also reviewed. This section reviews the research done on cavitation phenomenon in different fields of science.

Chapter 3 describes the numerous CFD simulations of pulse cavitation tool prototypes. Different properties of the fluid were under study in order to better understand the cavitating flow.

Chapter 4 summarizes the experimental procedures and plans for the flow tests done with pulse cavitation prototypes. Different flow rates were applied and pressures at the inlet and outlet of the tool were recorded. The corresponding forces were also measured by means of three load cells in an equilateral configuration.

In chapter 5 the sensitivity of drilling operation to cavitation vibrations and axial compliance is investigated. Different flow rates with high and low WOB, with constant bit revolution, and two compliant element configurations were the variables in the drilling experiments. Robust data analysis was performed and different aspects of the experiments such as time series and spectral analyses were conducted.

2. Literature Review

2.1 Characteristics of the cavitation phenomenon

2.1.1 Introduction to cavitation

The origin of the word cavitation comes from the Latin word “*Cavitas*” which means cavity or hollow space. Cavitation is the name of the phenomenon which may occur inside a liquid when it is under pressure fluctuations. If lowering liquid pressure to a low critical pressure is reached, and liquid bonds are weakened, voids filled with vapors from liquid, as well as other dissolved gases in it are produced. When these voids are subjected to sudden abrupt compression, they implode and cause pressure surges in the liquid [8]. Figure 1 shows boiling and cavitation process in a Pressure-Temperature diagram.

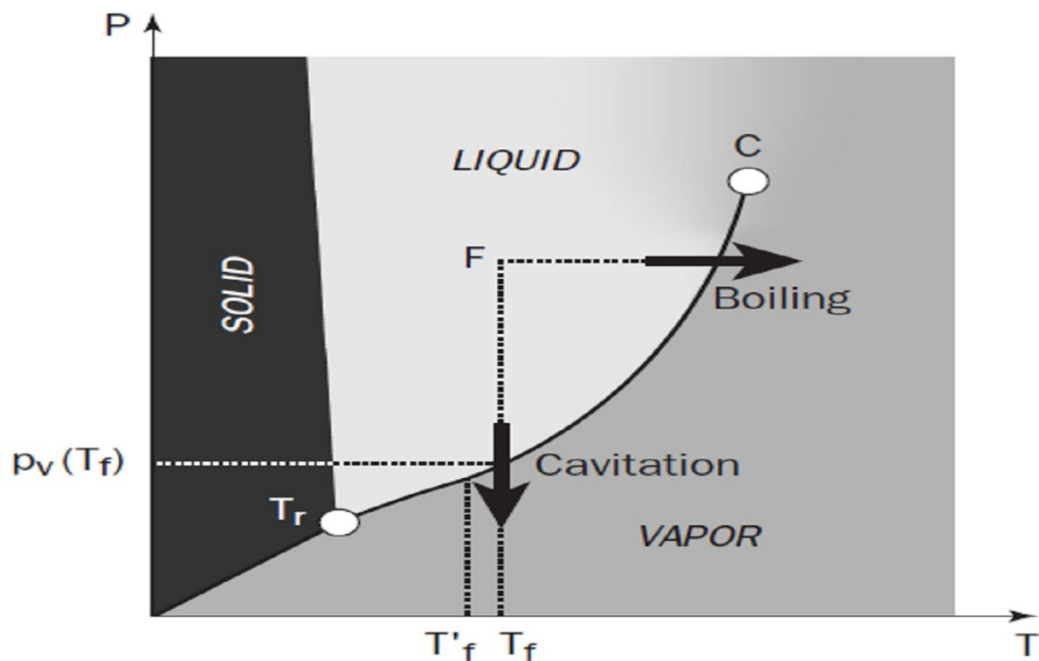


Figure 1. Phase diagram of water presenting boiling and cavitation process [8].

The isobaric process of making bubbles inside a liquid is called boiling. Cavitation also produces the same result. However, cavitation is an isothermal process in which the pressure of the liquid is lowered to its saturated vapor pressure, in order to turn in to its gaseous phase. We should keep in mind that cavitation is a discrete phenomenon which means that the bubbles are produced and released from the parent liquid throughout the liquid volume [7].

The spherical cavitation bubbles are mostly filled with liquid vapor and to some extent with other dissolved gases, if they are present in the liquid. When the pressure falls, these bubbles are produced and released from the liquid. Moreover, as the pressure reduction continues, bubbles size increases, and when they are introduced to higher pressure, they start to implode and make pressure fluctuations in the fluid [6].

Many different processes are suggested in order to make cavitation phenomenon occur inside a liquid, but the most common one with the least number of equipment is the hydrodynamic process. The idea behind the hydrodynamic process is to reduce the static pressure of a flowing fluid with changes in the geometry of the conduit of the passing fluid by introducing constrictions or curved channels. In this case, the liquid bonds are pulled apart by great expansive forces which are the result of sudden pressure drop [7].

2.1.2 Types of cavitation in hydrodynamics

There are many different classifications in the literature for cavitation according to the different aspects of this phenomenon. A simple classification which is based on the bubbles position in the liquid is presented here [9]:

1. Surface cavitation — developed on the surface of the constricting body in the flow and remains attached
2. Detached cavitation — carried along the liquid flow

Figure 2 represents the two types of cavitation.

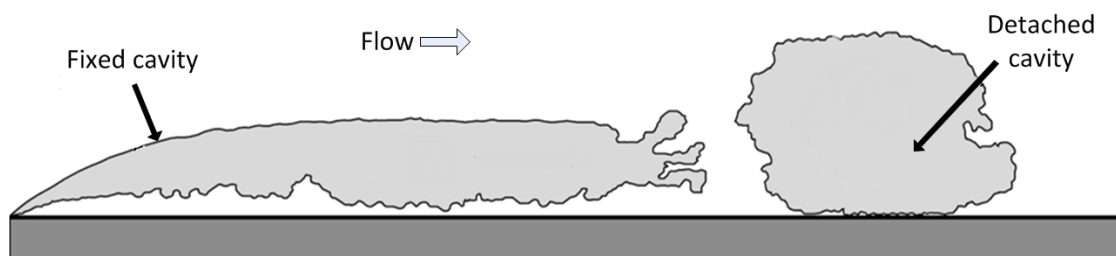


Figure 2. Fixed and detached cavity in vena contracta [9].

Surface cavitation occurs when there is a bluff body in the flow. The cavitation nuclei present on the surface of the bluff body are the potential initiation points for cavitation. As the cavitation continues, the attached cavity increases until a certain critical radius is reached, then the cavity becomes unstable and a portion of this cavity cloud is released from the front part and is carried away as a detached cavity. The attached cavity is the main source for the detached bubbles after the venturi, but there will also be individual bubbles created depending on the liquid pressure, since the

cavitation phenomenon is discrete and different locations are prone to go under cavitation depending on the local pressure [6].

2.1.3 Factors affecting the formation of cavitation

There are many different factors that affect the cavitation phenomenon. The most important factors are gaseous impurities dissolved in the liquid, other liquid impurities and also the physical properties of the flowing liquid such as its thermal state [8].

We should note that the nuclei present throughout the liquid in the forms of gaseous and vapor micro bubbles, are crucial in the cavitation inception. They play an important role in reducing the liquid surface tension. They also assist enhancing liquid capability to transfer tensile stresses and pull liquid molecules apart [7].

If we consider an ideal case where the liquid is pure and lacks any impurities, the phase transition from liquid to gas phase is almost impossible. Furthermore, large tensile stresses in the form of negative pressure reductions are necessary in order to initiate cavitation. However, in reality, and in nature, liquids are filled with large number of cavitation nuclei such as colloids, suspensions and other dissolved substances [8].

2.1.4 The effects of cavitation

Cavitation effects can be split into mechanical and physicochemical effects, depending on the changes that occur within the bubbles and their relative location in the flowing fluid. The mechanical effects include, cavitation erosion, cavitation noise and flow throttling induced by formation of vapor clouds. Furthermore, there are high frequency vibrations with low amplitudes in the cavitating zones. The two important

attributes of the cavitation phenomenon are the noise and the temperature rise in the vicinity of the venturi nozzles in hydrodynamic cavitation [7].

2.1.5 Cavitation number

Cavitation phenomenon in mathematical terms is best described by a dimensionless number K , known as cavitation number. K is defined as [6]:

$$K = \frac{P_1 - P_v}{P_1 - P_2} \quad (1)$$

Or

$$K = \frac{P_1 - P_v}{\frac{1}{2} \rho V^2} \quad (2)$$

Where:

- P_1 is the upstream pressure, pressure of the fluid before entering the constriction area
- P_2 is the downstream pressure, pressure of the fluid after exiting the constriction
- P_v is the vapor pressure of the fluid at a given temperature
- ρ is the density of the fluid
- And V is the velocity of the fluid in the constricted minimum area

Cavitation number relates the intensity of the cavitation with flow conditions. The cavitation number at which the inception of cavitation occurs is called cavitation inception number or K_i . If the flow condition results in a K value higher than K_i ,

cavitation will not occur. However, if the K value of the flow condition is equal to or less than K_i , cavitation will begin and start to grow [10]. This could be summarized as:

$$K_{\text{flow}} > K_i \quad : \text{ No Cavitation}$$

$$K_{\text{flow}} \leq K_i \quad : \text{ Cavitation inception and growth}$$

Figure 3 depicts the pressure changes while fluid is entering an orifice.

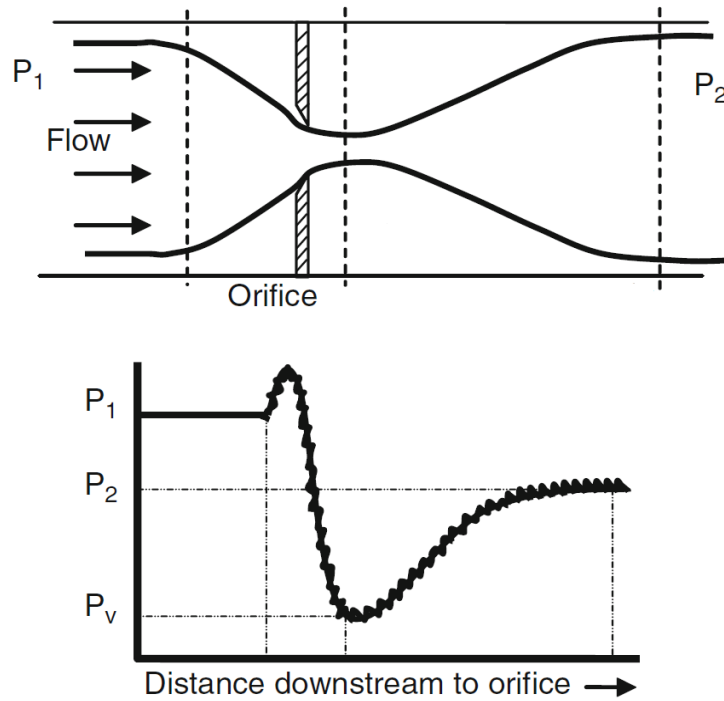


Figure 3. Streamline pressure drop behavior in an orifice [10].

It should be noted that K_i is strongly dependent on flow geometry. Consequently, different orifice sizes will have different K_i values. Orifices with the same diameter but different angles for divergent and convergent sections will also have different K_i

values and flow conditions at which cavitation occurs will be different for each geometry [7].

2.1.6 Vapor Pressure

In order to fully understand the vapor pressure concept, the classical thermodynamics point of view will be discussed. Cavitation in a flowing liquid occurs by transformation of liquid phase to vapor at constant temperature [11]. In the phase diagram of a liquid such as water, the liquid domain and vapor domain are separated with a curve starting at the triple point T_r to the critical point C. Figure 4 shows the Triple Point and Critical Point.

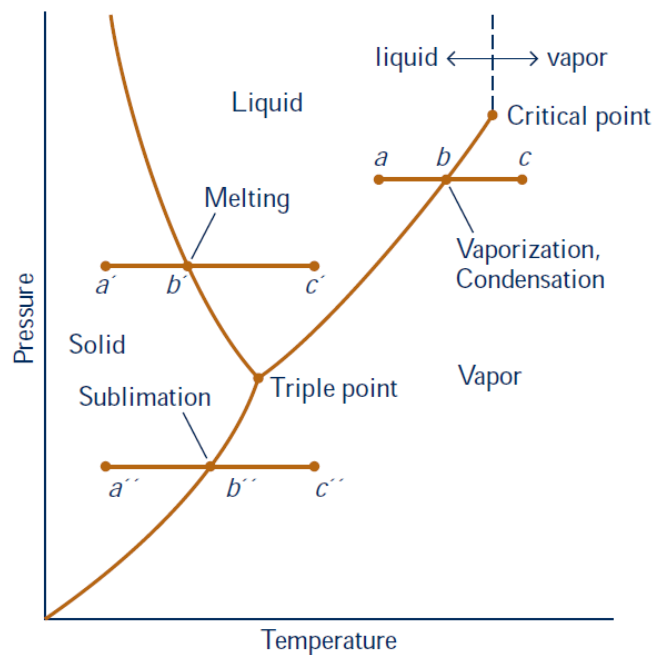


Figure 4. Phase diagram presenting vapor pressure [11].

Any reversible transformation from one phase to another such as evaporation or condensation under equilibrium conditions can be presented at the phase diagram by crossing the curve at pressure P_v , the vapor pressure. Cavitation occurs in a liquid by

lowering the static pressure at a constant temperature. Thus, this phenomenon is similar to boiling, except the driving mechanism is not a change in the temperature but a pressure change which can be applied by altering flow dynamics [7].

This process is approximately isothermal. To fully understand it, let us consider cold water. In order to form a significant amount of vapor, a relatively small amount of heat is employed. The surrounding liquid which acts as a heat source shows only a minute change in temperature and hence the overall liquid temperature remains constant which means the process is isothermal [6].

From a theoretical point of view, the first instants of cavitation can be divided into several steps [6]:

- 1- Breakdown of liquid or void creation
- 2- Filling of voids with vapor
- 3- Saturation of voids with vapor

However, we should keep in mind that in reality all these steps happen almost simultaneously.

2.2 Principles of Bernoulli's Equation

2.2.1 Bernoulli's Equation derivation

For simplicity, an incompressible fluid with constant density ρ , such as water, flowing with a constant volume flow rate of $Q = A_1 v_1 = A_2 v_2 \text{ m}^3/\text{s}$ is discussed. Figure 5 shows an arbitrary flow path with mentioned conditions. The pressure is constant as long as the radius and elevation are constant and the friction losses are insignificant [12].

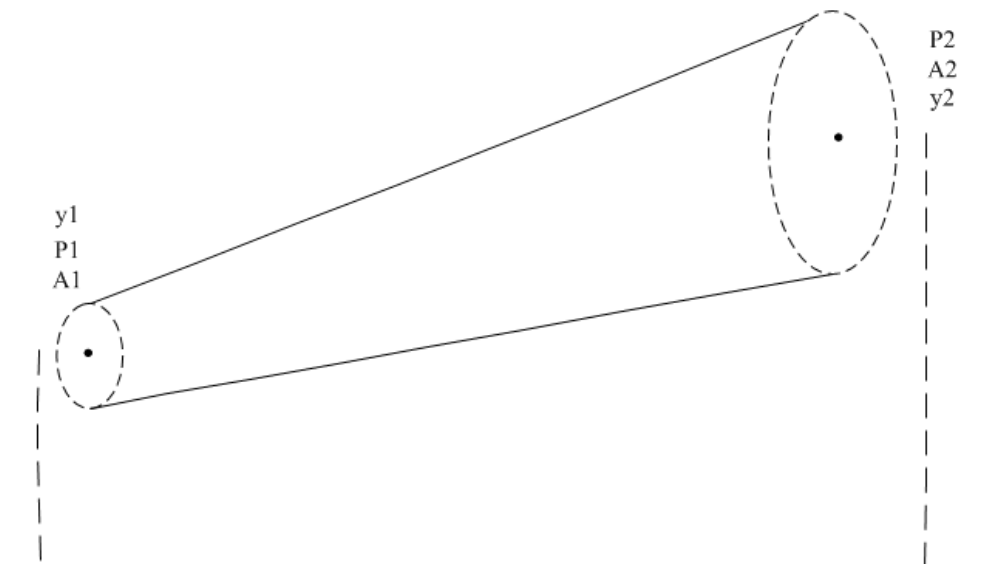


Figure 5. Schematics of an arbitrary conduit with flow rate Q [12].

The pressure changes in a volume of fluid in a pipe flowing first at point #1, and then at point #2 is studied. According to the conservation of mass law, volume flow rate at both points of the pipe is constant.

The total mechanical energy of the volume element at position #1, E_1 is [13]:

$$E_1 = \text{Kinetic energy} + \text{Potential energy} = (1/2)\Delta m_1 v_1^2 + \Delta m_1 g y_1 \quad (3)$$

Where v_1 is velocity, y_1 is elevation, and Δm_1 is mass. Similarly at position #2, its total mechanical energy, E_2 is:

$$E_2 = \text{Kinetic energy} + \text{Potential energy} = (1/2) \Delta m_2 v_2^2 + \Delta m_2 g y_2 \quad (4)$$

Based on our assumption which is constant volume flow and incompressible fluid, the mass is constant for both volume elements during the flow, so that we may substitute:

$$\Delta m_1 = \Delta m_2 = \Delta m \quad (5)$$

Clearly, if the velocities were constant i.e. ($v_1 = v_2 = v$), and if there was no change in height ($y_1 = y_2 = y$), then there would be no change in the total mechanical energy of the fluid [11]. However, if any of these parameters change between position #1 and position #2, there will be changes in the total mechanical energy of the fluid:

$$E_2 - E_1 = (1/2) \Delta m v_2^2 + \Delta m g y_2 - (1/2) \Delta m v_1^2 - \Delta m g y_1 \quad (6)$$

This difference in mechanical energy comes from the net work done on the fluid between point #1 and point #2. Net Work = $W_{in} - W_{out}$

At point #1,

$$W_{in} = [\text{Force}] [\text{Distance}] = [\text{Pressure Area}] [\text{Velocity Time interval}] \quad (7)$$

$$= (P_1 A_1) (v_1 \Delta t) \quad (8)$$

(Δt is the time to move an element length)

Now, we multiply the above by $\rho / \rho = 1$,

$$=P_1 (A_1 v_1 \Delta t) (\rho / \rho) = P_1 (\rho A_1 v_1 \Delta t) / \rho \quad (9)$$

$(v_1 \Delta t)$ is simply the length of the volume element. Also, A_1 is its cross-sectional area. These two multiplied together gives us its volume, and density times volume equals mass. Thus, $(\rho A_1 v_1 \Delta t)$ is the mass of volume element at position #1. Therefore,

$$W_{in}=P_1 \Delta m / \rho \quad (10)$$

The same is valid at point #2. $W_{out} = P_2 \Delta m / \rho$

Thus, the net work done on the fluid, which is the work done on the system minus the work done by the system, is

$$W_{in} - W_{out} = (P_1 \Delta m / \rho) - (P_2 \Delta m / \rho) = (P_1 - P_2) \Delta m / \rho \quad (11)$$

This net work is the source of the mechanical energy difference, $E_2 - E_1$, so we will have:

$$E_2 - E_1 = \Delta m \left[(1/2) (v_2^2 - v_1^2) + g (y_2 - y_1) \right] \quad (12)$$

The net work and the change in mechanical energy must equal each other according to the work-energy theorem, therefore,

$$(P_1 - P_2) \Delta m / \rho = \Delta m \left[(1/2) (v_2^2 - v_1^2) + g (y_2 - y_1) \right] \quad (13)$$

Since the fluid is incompressible, the mass terms cancel,

$$P_1 - P_2 = \rho \left[(1/2) (v_2^2 - v_1^2) + g (y_2 - y_1) \right] \quad (14)$$

$$= (1/2) \rho v_2^2 - (1/2) \rho v_1^2 + (\rho g y_2 - \rho g y_1) \quad (15)$$

Now we move all negative terms to the opposite side of the equation,

$$P_1 + ((1/2) \rho v_1^2) + (\rho g y_1) = P_2 + ((1/2) \rho v_2^2) + (\rho g y_2) \quad (16)$$

which gives us Bernoulli's Equation in its normal presentation [11] as:

$$P_1 + \frac{1}{2} \rho v_1^2 + \rho g y_1 = P_2 + \frac{1}{2} \rho v_2^2 + \rho g y_2 = \text{constant everywhere in the fluid [11].}$$

2.2.2 Physical interpretation of Bernoulli's Equation

We should first note that, if the cross-sectional areas at points #1 and #2 are the same, then the two velocities are equal and the $(\frac{1}{2} \rho v^2)$ terms cancel each other [13]. Further, if the pipe is horizontal and there is no difference in heights at points #1 and #2, the two $(\rho g y)$ terms cancel each other. If both are true, then no matter what happens to the pipe size and elevation between these two points, the pressure at these two points will be equal: $P_1 = P_2$ with no friction present [14].

If we examine the case where only the elevation is constant, then we get:

$$P_1 + \frac{1}{2} * \rho v_1^2 = P_2 + \frac{1}{2} \rho v_2^2 \quad (17)$$

What this equation tells us is that, as the velocity increases the pressure decreases. To understand this we need to remember that the two sides of the equation must remain equal. If v_2 increases because of a decrease in A_2 , then P_2 must decrease in order for their sum to maintain its equality with the left side of the equation [13].

2.3 Periodic Cavitation shedding in a cylindrical orifice

2.3.1 Introduction to different cavitation patterns

Many studies have been done on high speed liquid jets and the results indicate that cavitation within the nozzles significantly enhances the atomization of these jets. It has been reported that cavitation reduces jet break up length and hence increases jet spray angle [15].

In nozzles, cavitation is initiated in the high shear layer of the nozzle entrance where inertial forces reduce the local pressure below the vapor pressure of the liquid. Surface microscopic roughness, other impurities and dissolved gases are the potential nucleation sites for cavitation bubbles growth [7].

As discussed before, cavitation is described by cavitation number:

$$K = \frac{P_1 - P_v}{P_1 - P_2} \quad (1)$$

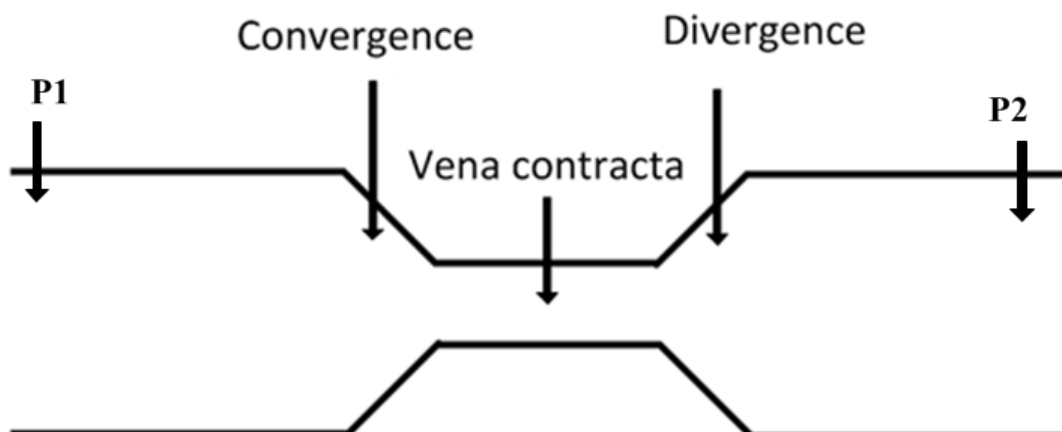


Figure 6. Schematic of venturi.

Figure 6 shows a typical convergent-divergent venturi and location of pressure sensors measuring inlet and outlet pressures of the passing liquid in order to calculate cavitation number for this flow condition. P_1 is pressure upstream of the nozzle or injection pressure, P_2 is the ambient pressure, and P_v is the vapor pressure. Increasing injection pressure P_1 or reducing ambient pressure P_2 , causes the cavitation structure to grow and move further in the vena contracta [15]. As discussed before, for each flow condition and geometry of the conduit, there is a specific cavitation inception number K_i .

If the K is greater than K_i , cavitation does not exist. However, as K decreases and reaches $K_{i, \text{fixed}}$ cavity cavitation structure starts to grow. If cavitation intensity increases, and therefore the K value decreases, the fixed cavity length starts to grow. Figure 7, compares the intensity and fixed cavity length for both high and low K values. If this growth continues and cavitation structure reaches the exit plane of the venturi, this phenomenon is called supercavitation [7].

Atomization of the jet decreases the jet break up length and hence better cleaning is achieved since a larger area is under jet influence. However, as the cavitation intensity grows and supercavitation is reached, there would be no improvement for jet atomization [6]. This means that when flow is experiencing supercavitation, no further improvement in increasing jet spray angle or atomization is possible. If P_1 starts increasing or P_2 decreasing even after supercavitation, then the jet will be completely detached from the venturi wall and it will be surrounded by vapor and hence the jet break up length will be increased due to the fact that there is no surface resistance and

no internal perturbations are present anymore. This condition is referred to as hydraulic flip [7].

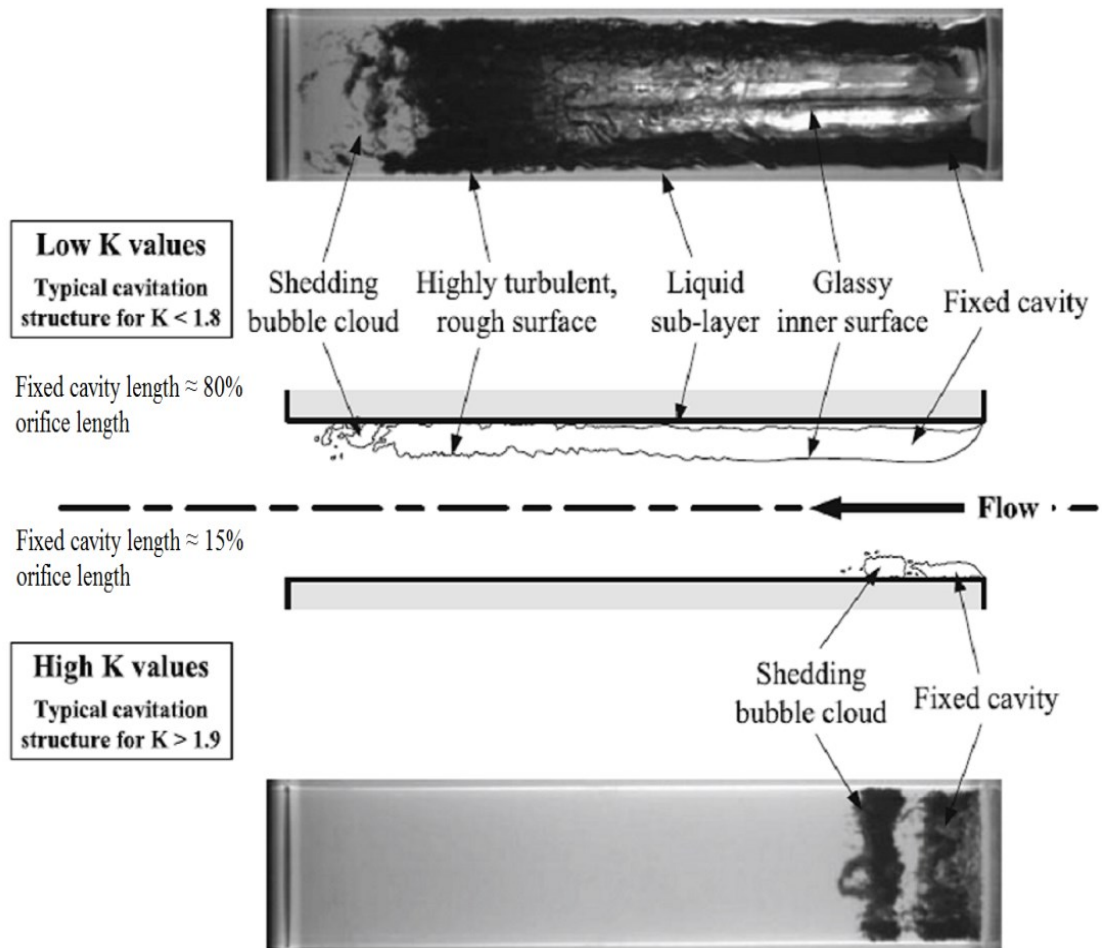


Figure 7. Flow behavior in venturi with different cavitation numbers [15].

In the case of periodic shedding, the cavitation cloud only occupies a portion of the venturi and cyclic cavitation cloud shedding has been observed. The fixed type cavitation structures have been observed to grow until a critical size is reached, then the leading portion of the cavity cloud is detached from the fixed type and travels along the piping after the nozzle as an independent structure, and these steps are repeated again. Various experiments have been done regarding the study of cavitation

in different nozzle shapes and size. Stanley (2012) has done an experiment with orifice size of 8 mm in diameter as shown below. The schematics of the orifice inside the pressure vessel are shown in Figure 8 [7].

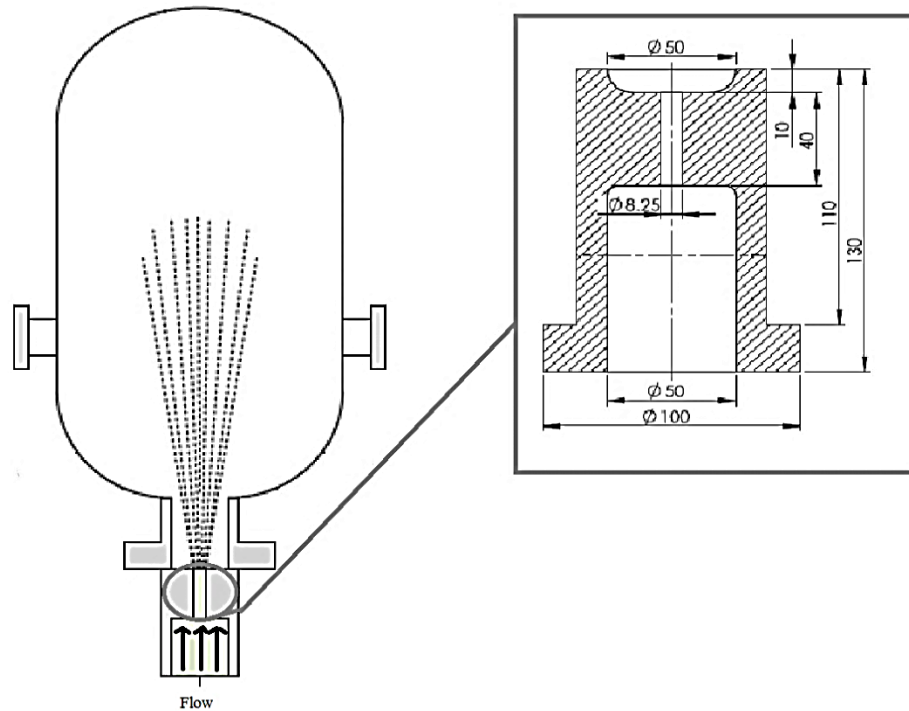


Figure 8. Schematics of the orifice inside the pressure vessel [7].

In this test section, the ratio of orifice length to diameter L/D of 4.5 has been used. Also the ratio of orifice diameter to pipe diameter d/D is 6. Stanley [15] used high-speed digital recording in order to capture the phenomenon inside the tubing. The fixed cavitation cloud portion was measured by analyzing high speed camera recordings. He has divided the cavitation phenomenon into different states: No cavitation-Developing cavitation-Periodic shedding-Supercavitation-Hydraulic flip. The measurements show that for developing cavitation with cavitation number $K > 2$,

cavitation was initiated in the separated shear layer near the nozzle entrance and gets extended up to the mean length to about 15% of the orifice length. As the condition of flow rate and P1 and P2 are modified, and cavitation number is slightly reduced from 2 to $K \approx 1.8$, the collapse length started to grow rapidly of about 30% of orifice length [7].

Further decrease in cavitation number, resulted in sudden discontinuous increase of collapse length to an average length of 80% of orifice length. As the K goes below 1.8, the fixed cavity stretches from nozzle entrance and the cavitation clouds are shed at the nearly exit of the nozzle, a phenomenon known as supercavitation. Figure 9 summarizes the experiments results. As the cavitation number is decreased while the Reynolds number is relatively constant, production of vapor phase accelerates and fixed cavity occupies greater portion of the vena contracta [15].

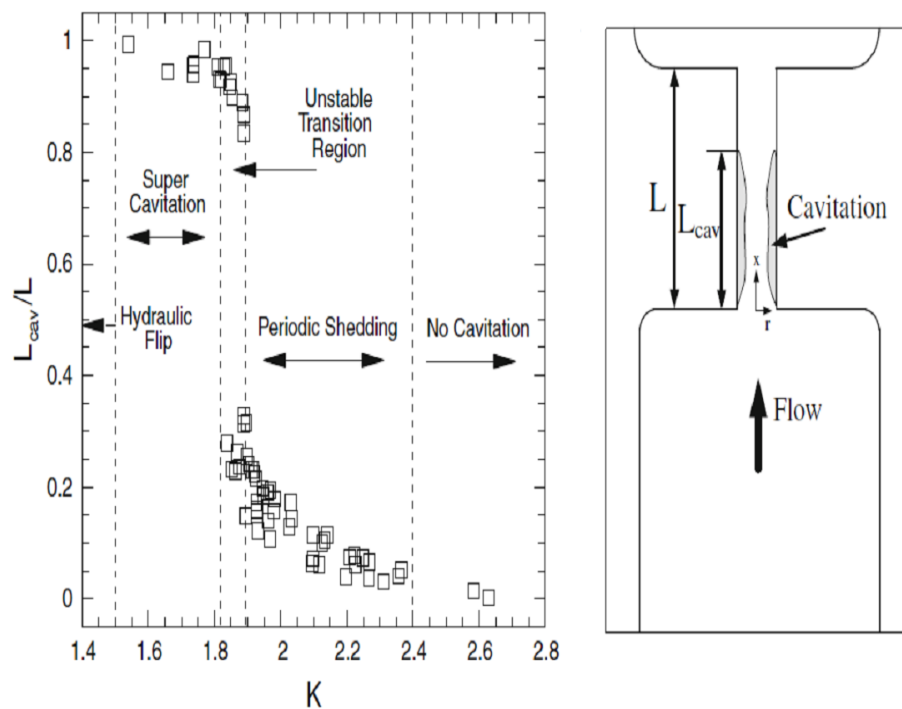


Figure 9. Classification of different flow behavior and the relevant fixed cavity length [15].

When cavitation is initiated and continues, the velocity vectors at the centerline of the orifice increases due to the fact that liquid has lost some portion of cross sectional area available at the orifice. These higher velocity vectors increase the shear force exerted on the fixed cloud cavity and drag it towards the nozzle exit where pressure returns to higher values. This results in increase in the fixed cloud length and cavitation intensity. Figure 10 shows the fixed cavity length for 3 different K values [16].

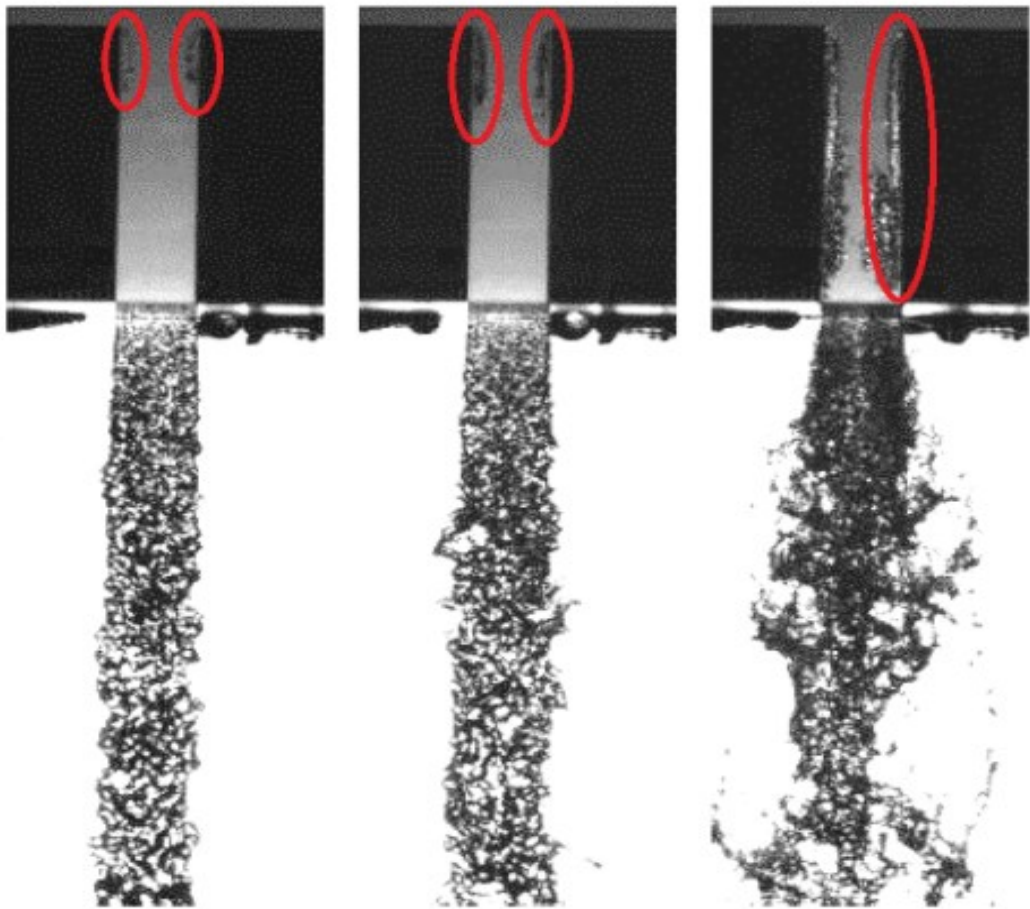


Figure 10. Flow behavior at the outlet of the nozzle with increasing fixed cavity length [16].

2.3.2 Periodic cloud cavity

As it has been observed in Figure 9, the periodic cavity pinching off from the fixed cavity occurs where $1.8 < K < 2.1$. Figure 11 shows the schematics of shedding cavitation for a single cycle where only one bubble cluster is pinched off from the parent fixed cavity cloud [7].

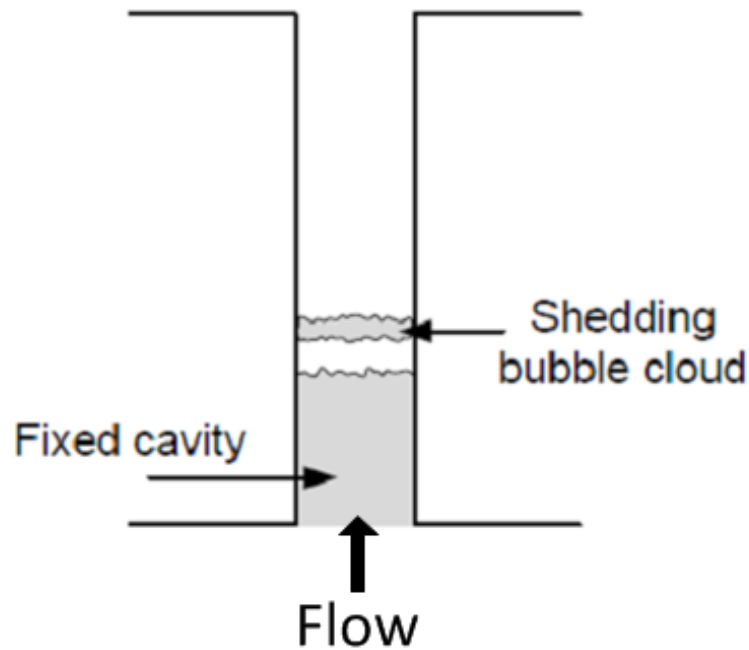


Figure 11. Schematics of the shedding phenomenon inside the nozzle [7].

The sequence of the cavitation shedding phenomenon has been captured using high speed digital recording. Figure 12 shows the sequence of shedding cavity inside the orifice for $K = 1.97$ and Reynolds number $Re = 1.1 \times 10^5$. Image 1 shows that the frontier bubble cloud (B) is starting to detach from the fixed cavity (A). The next image shows that the space between A and B is getting more distinguishable as the smaller clouds in B are connecting to each other and coalescing. The next image

shows that the leading cavity cloud B is completely separated from the fixed cavity A and is an independent structure moving along the conduit. Surface tension forces gather the bubble clouds together and make them a concentrated vortex and increases the gap between two structures A and B. In the next image, we observe that the cavity structure B has collapsed and very small remainder of this collapse is visible [15].

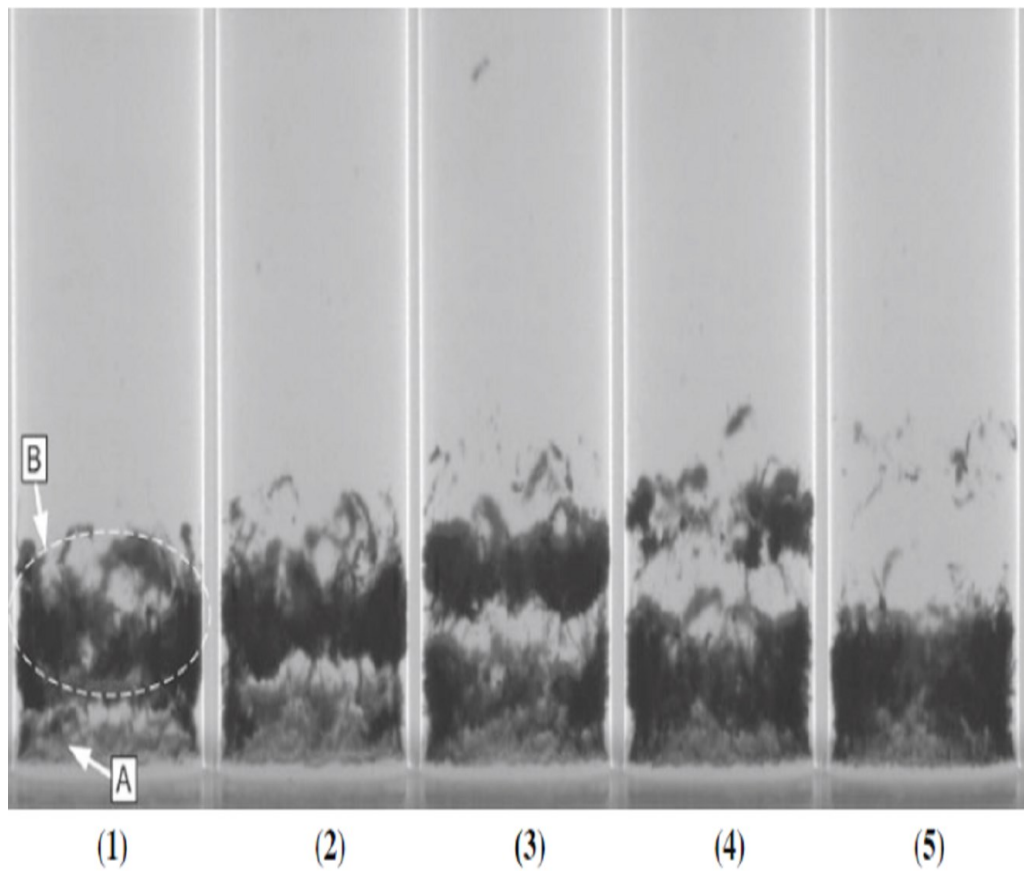


Figure 12. Sequence of bubbles cluster shedding [7].

2.3.3 Measurements of spray angle variation with cavitation

Figure 13 shows the video recordings of the near nozzle spray structures for K values ranging from 1.22 to 2.5. The images represent jet flow in different states from single phase flow to hydraulic flip condition [7].

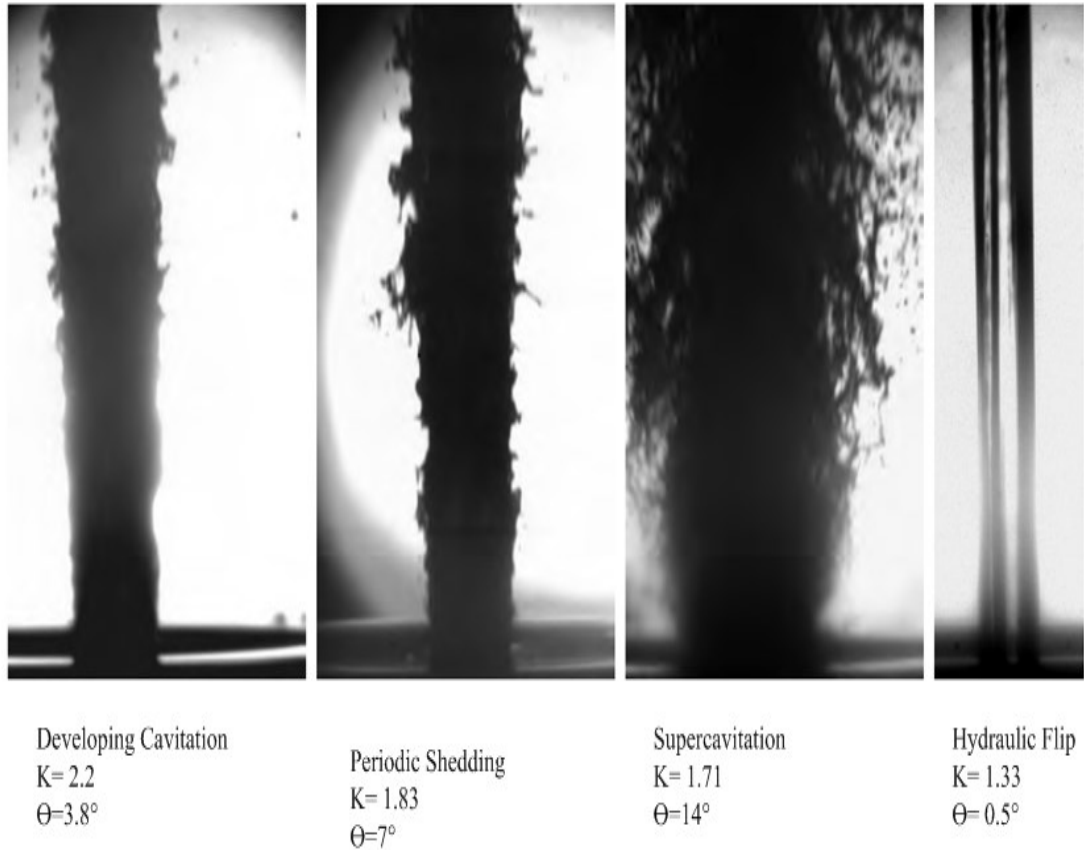


Figure 13. Spray angle variation with cavitation number [15].

As the images show, for $K > 2$, there is very negligible variation in spray angle. The angle is a constant value of about $\theta \approx 2^\circ$. These values of θ for $K > 2$, also agree with the short collapse length of $L_{cav} < 0.15 L_{orifice}$. Any surface perturbations that are visible result from turbulent flow fluctuations inside the nozzle. As K decreases below two, $K < 2$, there is a significant and abrupt increase in spray angle. This phenomenon

corresponds directly to the fact that the fixed length cavity in vena contracta increases suddenly. As the average collapse length or fixed cavity length increases by lowering the K value, the increase in spray angle continues until the fixed cavity reaches the nozzle exit. At this point, the spray angle reaches its peak value of $\theta = 14^\circ$ for the supercavitation condition. Figure 14 shows the half-cone spray angle plotted versus cavitation number [7].

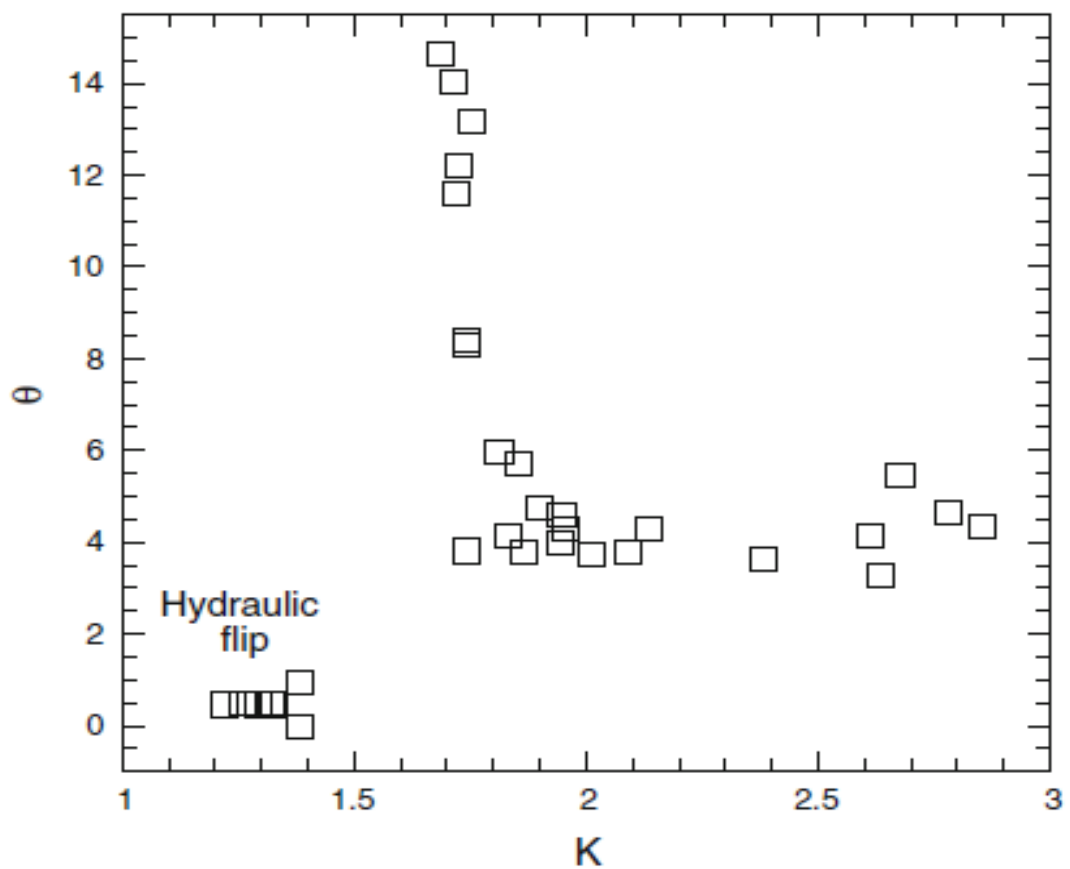


Figure 14. Half-spray angle relationship with cavitation number [7].

2.4 Development and testing of a Polycrystalline Diamond Compact (PDC) bit with passively-pulsating cavitating nozzles

Research in drilling hydraulics shows that the horsepower provided by a conventional drilling rig is significantly higher than the power transferred to the rock by means of bit cutter rotation. This section will discuss the mechanism of using passively pulsating cavitation nozzles within PDC bits to utilize the source hydraulic power much more efficiently in the rock cutting process [17].

A project by U.S. Department of Energy with collaboration of Sandia National Laboratories was conducted with the goal of increasing the rate of penetration and hence reducing the drilling costs. Reducing drilling costs is facilitated by either increasing the penetration rate or by increasing the drill bit life [18].

PDC is an acronym for Polycrystalline Diamond Compact. PDC bits are manufactured of many synthetic cutting elements, or PDCs, and mounted on the bit surface in a specific arrangement. The abrasiveness and high compressive strength of most of the rocks underground have made the PDC bits quite widespread [19].

Over the past decades, many researchers have tried to commercialize the use of high pressure (>10,000 psi) water or mud jet in drilling systems. The attempts to apply such high pressure jets have failed due to the fact that high pressure equipment maintenance is costly and using such high pressure mud jets with abrasive materials is hazardous according to the Health, Safety and Environment (HSE) regulations [17].

In the drilling industry it has been established that as depth increases the pore pressure of the formation also increases. To avoid formation fluid kick and further the well

blowout, the Over Balanced Drilling (OBD) has been used. Thus, as well depth increases, the bottom hole pressure increases, and more energy is required to cut through the rock [2]. However, high pressure jets have significantly reduced the necessity of applying more energy and WOB. Several researchers have conducted experiments regarding this issue and the results show significant reduction of cutter forces, or penetrating stresses, required to drill the rock. In most cases, the cutter forces have been reduced by more than 30%. There are two mechanisms that reduce cutter forces [18]:

- 1- The fine cuttings produced by the surface penetrating action of the bit are blasted away by the high velocities and hence, increase the stress concentration on the rock.
- 2- The fluid enters the cracks created at the surface of the rock created by the cutter action and hydraulically enlarging these fractures and reduces the mechanical forces required.

Figure 15 is the schematics of how the cavitating jet erodes the rock surface.

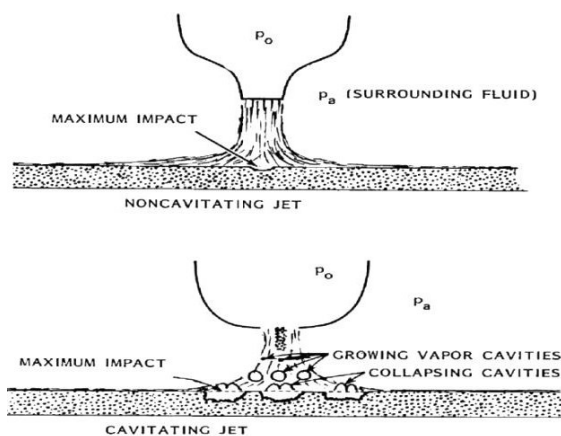


Figure 15. Comparison of non-cavitating and cavitating jet [18].

Instead of using high pressure at the source to create high jet velocities, a new design which induces cavitation could be applied. One of the main features of cavitation is its ability to improve hole cleaning at bit rock interface by weakening and direct erosion of the rock. Figure 16 is the schematics of the cavitating jet nozzle which induces cavitation ring clouds [18].

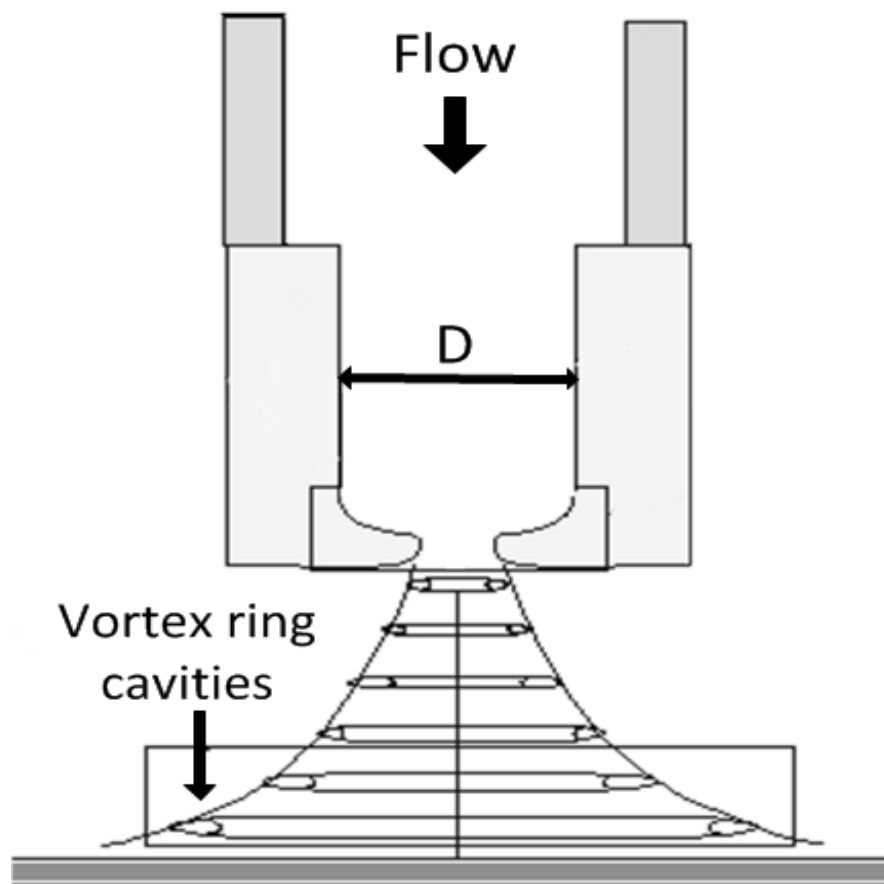


Figure 16. Passively pulsating nozzle schematics [17].

In order to incorporate the cavitating nozzles, the design should satisfy the pressure drop requirements. For a given pressure drop, choosing a rather large nozzle size would require higher flow rates (more than 300 USGPM) or reducing the total number of nozzles. Also the smaller size nozzles are prone to blockage by large particulates

that may be present in the mud. The design should satisfy the requirement that there should be a nozzle for each blade for optimum hole-cleaning and also small enough size to induce cavitation. To mitigate the blockage problem, a robust filtering system should be present to remove any large particulates from the mud. To test these nozzles two different types of rock were chosen to drill [17]: (1) Crab Orchard Sandstone – low permeability and low porosity with UCS of 21,000 psi (138 MPa); and (2) Sierra White Granite – negligible permeability and porosity with UCS of 28,000 psi (193 MPa)

Figures 17 and 18 show the ROP versus WOB for Crab Orchard Sandstone and Sierra White Granite respectively. As depicted in the figures, PDC bits have better penetration rate compared to Roller Cone bits.

Comparison of normal PDC bits with PDC bits with cavitating nozzles, illustrates that PDC bits with enhanced nozzles have higher penetration rates.

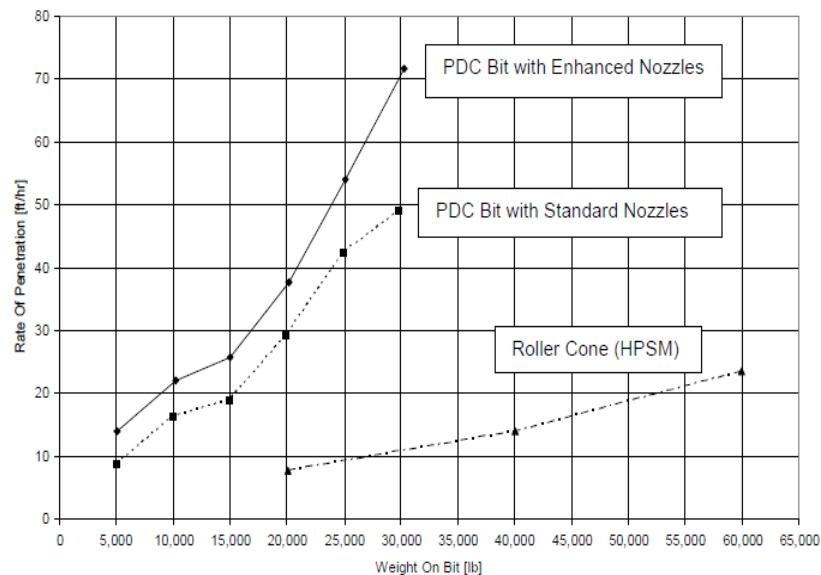


Figure 17. ROP versus WOB for Crab Orchard Sandstone [17].

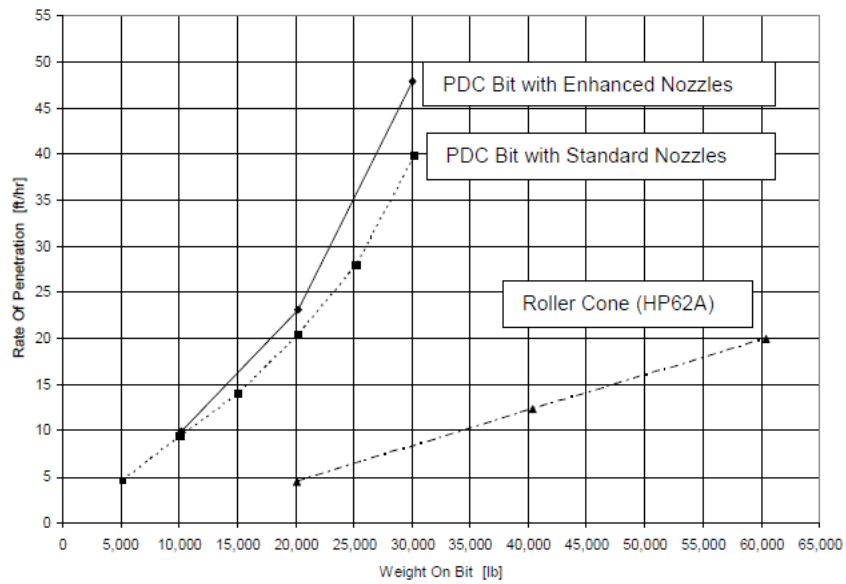


Figure 18. ROP versus WOB for Sierra White Granite [17].

Drilling both of the rocks mentioned above using a PDC bit with cavitating nozzles showed up to 40 % increase in ROP. Also at a given penetration rate, cavitation nozzles reduce the required cutter force and hence the WOB. This effect reduces the bit damage probability which is caused by abrasion and impact loading when hard formations are drilled by applying high WOB [17].

2.5 Cavitation damage to geomaterials in a flowing system

The cavitation damage also has been investigated in mining and geosciences as well as oil well drilling. Experiments conducted by introducing a cavitating water jet in front of rock and concrete samples in time intervals as short as 5 seconds, have shown measurable damage at the rock surface [20]. Erosion of rock and concrete samples by means of cavitating flow is described by the following mechanisms [21]:

- 1- Generation of shock waves due to bubble implosion.

2- Formation of high velocity microjets due to bubble implosion near solid material surface.

3- Direct collapse of bubble clusters at rock surface.

We should note that as the jet leaves the nozzle and impacts the specimen, two distinguished zones are created at the rock surface. These zones look like a crater. The first zone, directly in front of nozzle center, zone 1, has intense erosion and zone 2 has lower intensity at the periphery of zone 1. Figure 19 shows the different zones that occur under the cavitating flow impact [20].

Barnes [20] also explained that when a bubble collapse occurs in the vicinity of a solid material, this collapse produces a hammer-like blow of high strength in a very small area. If these collapses are occurring in a stream, violent shocks are produced. These shocks will rapidly dissipate unless they are in close distance of a solid material. In this case they will pound on the surface over and over by each collapse of a bubbles cluster [20].

The effect of the collapsing bubbles is similar to the hammer-blows on the surface. These hammer-blows shatter the surface of the nearby material. Small pieces of the material surface are dislodged and carried away while fracturing continues. As more pieces are dislodged and carried away the surface roughness increases and erosion continues [22].

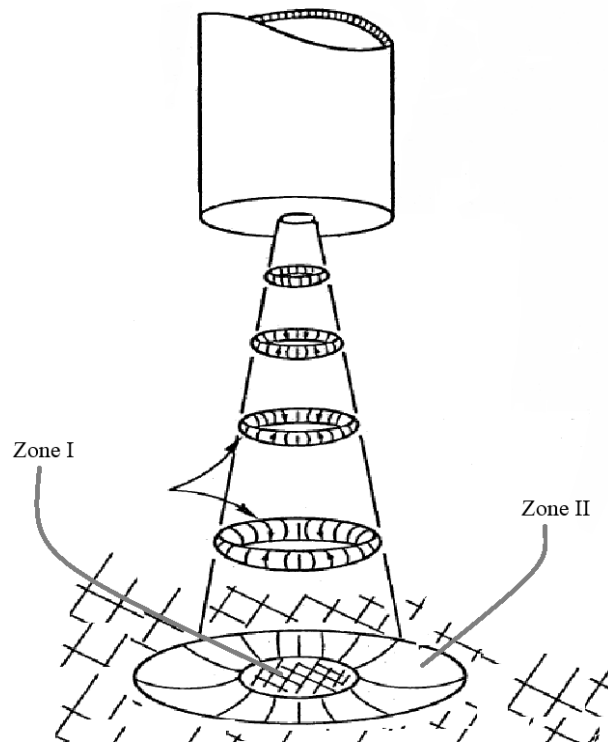


Figure 19. Different zones under cavitating jet impact [22].

The direct cavitating stream on a material first introduces a network of fine cracks. Then these cracks become deeper and bigger and particles become loose and are blasted away [22].

The other effect of these cavitating stream and collapse of the bubbles is vibration. The vibration is induced by the hammer-blows of the successive impacts produced by collapsing of bubbles. This also causes the failure of the material through fatigue [20]. Figure 20 shows the different scenarios in which a bubble is interacting with a solid surface [23]:

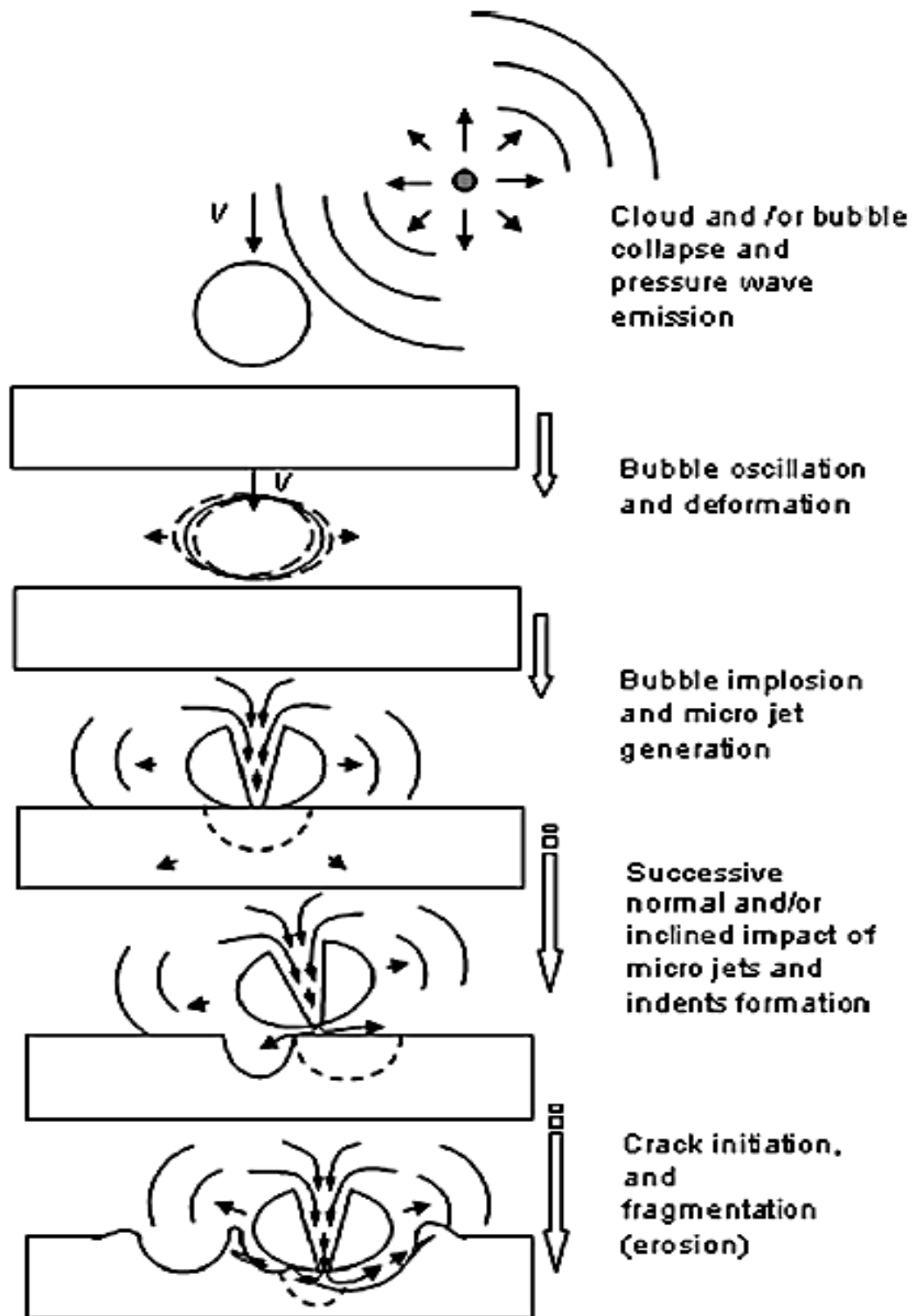


Figure 20. Sequence of cavitation bubbles damage on rock surface [23].

2.6 Summary of literature review

Basics of cavitation phenomenon and properties of a cavitating flow were presented. Also, the Bernoulli's principle was presented in detail which was necessary in better understanding of how different properties of a flow such as pressure, velocity and height are related to each other and how this could be used in order to make a single liquid flow to begin cavitating.

Cavitating flow is defined by cavitation number. For each specific flow condition, there is a specific cavitation number. Understanding the cavitation number and the condition it represents helped us understand the flow behaviour such as single flow, periodic bubble shedding, supercavitation, etc.

Effects of including a cavitating nozzle in a PDC bit were studied. Also, behaviour of solids in direct contact with cavitating flow and its destructive nature was studied.

These topics helped in understanding the nature and properties of a cavitating fluid. Furthermore, tuning the cavitating flow conditions to reach optimum results and applying these results in drilling experiments to increase the penetration rate were based on studying the cavitating flows in details.

3. CFD Simulations

In this chapter, the simulation work done regarding the cavitation phenomenon initiation and different features of a cavitating flow is studied. This chapter shows the numerous simulations done before manufacturing the different prototypes of the cavitating venturis. This assisted understanding of the cavitating flows by studying various properties of this phenomenon such as pressure patterns at different locations of the tool assembly, velocity and density changes, etc. Also the 3D visualization of the flow helped in better understanding of the behavior of the flow such as detecting the initiation locations of the cavitation, and travelling of the detached bubbles through the tool length after the venturi.

3.1 Summary of CFD method

In order to solve a CFD problem, we need to have a simple model of our prototype imported to the CFD software. However, we should take into account that simplifying the model would not change the nature of the problem or give inaccurate results [24]. Also, after the suitable physics and governing equations are defined for the problem, appropriate boundary conditions should be defined. They are a required component of the mathematical models [25].

Figure 21 shows the drawings of the 4 mm venturi designed to use in the experiments. The simulations were done importing the computer assisted drawing or CAD files of the design into the CFD software.

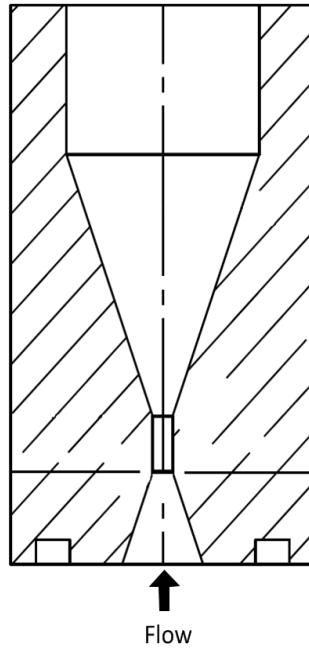


Figure 21. Schematics of 4 mm venturi.

The design considers the fact that the pressure drops caused by the venturi effect will be large enough to decrease the pressure of the stream to its vapor pressure. The venturi is designed to be replaceable in order to test different venturi sizes and choose the one with best performance. This design made it possible to test two different nozzle sizes. Two venturis with diameters of 4 mm and 12 mm were simulated and tested. Figure 22 shows the schematics of the main housing in which the venturis were inserted.

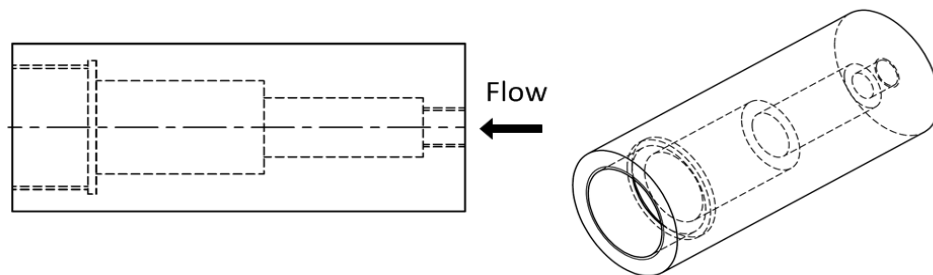


Figure 22. Schematics of the main housing for venturis in the assembly.

The schematics of the assembly with venturimeter inserted are shown in Figure 23.

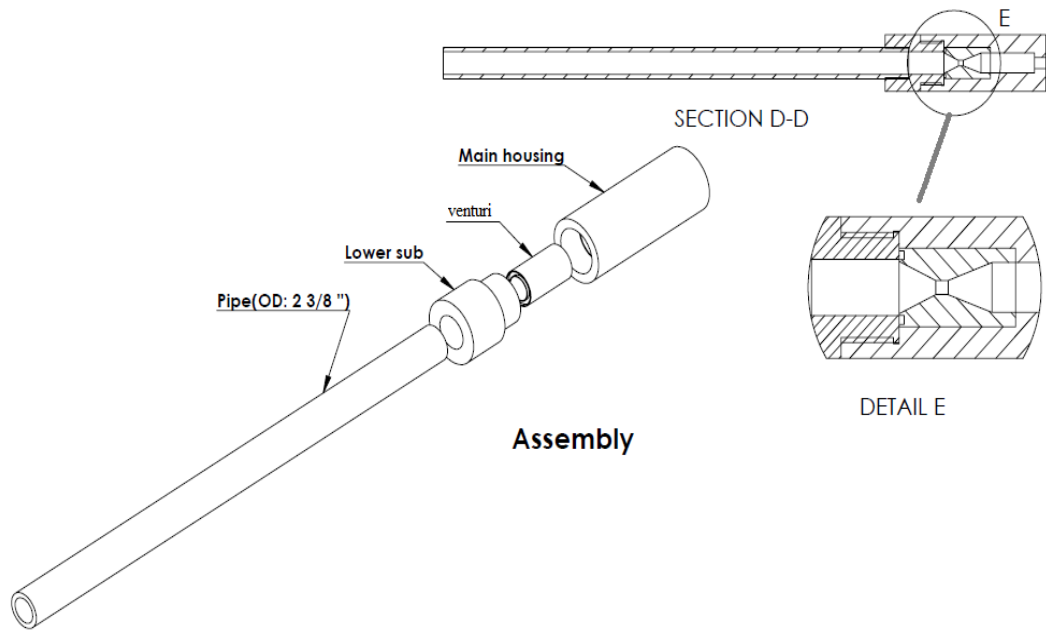


Figure 23. Exploded view of the assembly.

3.2 Simulation results of the 4 mm venturi

Figure 24 shows the assembly imported to the geometry section of the CFD software.

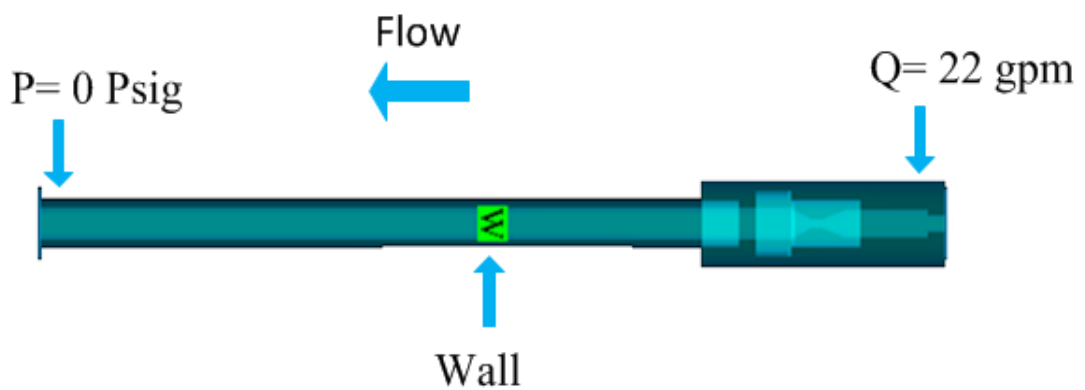


Figure 24. View of imported model into Flow3D simulation.

Figure 24 also shows the direction of the flow. The boundary conditions that are applied are atmospheric pressure at the downstream and different flow rates are applied at the inlet of the geometry. Figure 25 shows the sequence of the cavitation inside the venturi inside the pipe. Image 1 on the left shows the beginning of the simulation. As the simulation starts and the results start to stabilize, flow start to pass from the inlet and move towards the convergent section of the venturi.

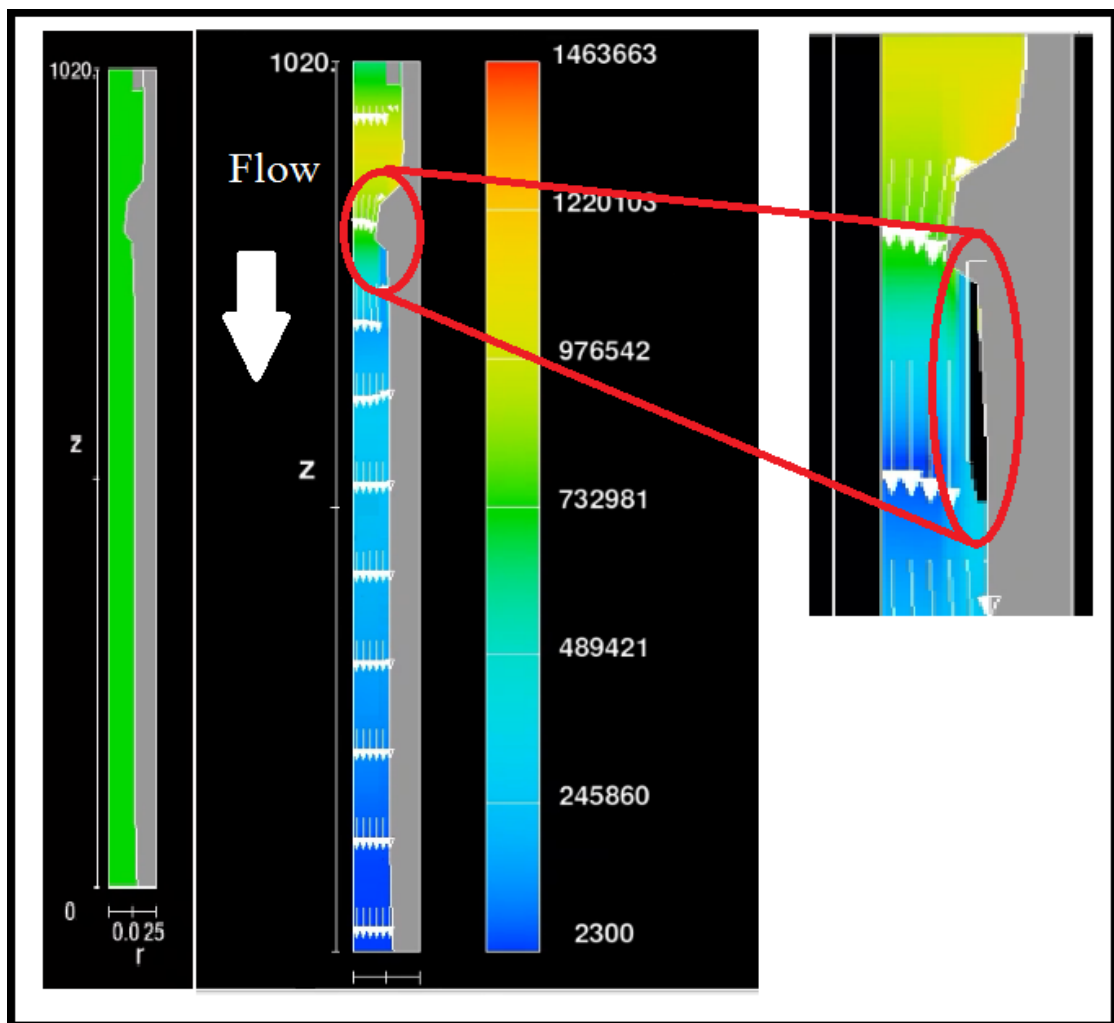


Figure 25. 2D presentation of fluid passing venturi and initiation of bubbles growth.

As the fluid passes this section, the pressure starts to fall. Pressure decline continues and reaches the critical vapor pressure of the fluid, small cavities start to grow. The second image shows the fixed cavity near the outer section of the venturi. This is the fixed cavity length as discussed in the previous chapter.

This cavity cloud is attached to the pipe wall. It starts to grow until it reaches the critical value where excessive growth will make it unstable. Hence, the frontier portion will be detached in order to keep the cavity cloud stable.

At this point, the detached portion will start to move along the fluid streamline. Regarding the location of the cavitation cloud, Figure 26 shows two different types of the cavitation clouds in two different regions of the flow.

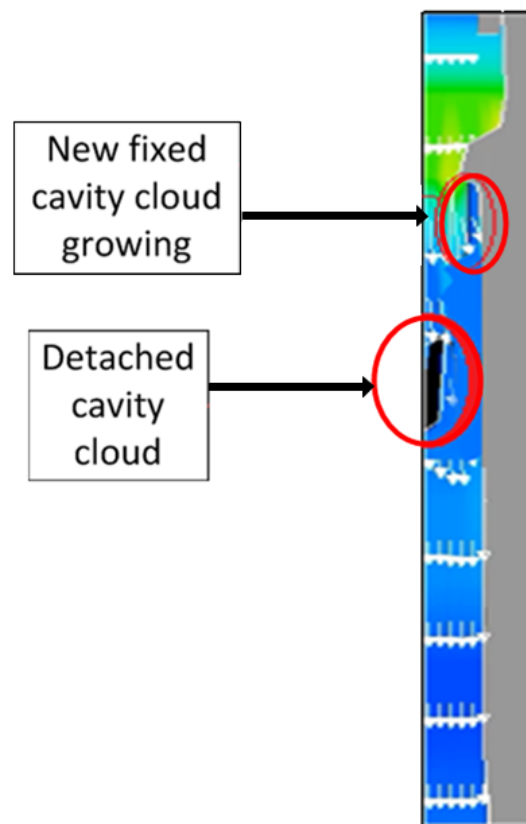


Figure 26. Fixed and detached cavity clouds in Flow3D.

Figure 27 summarizes the simulation process in 3 different stages. This figure shows the travel of the detached cavities inside the pipe. These cavities are detached from the fixed cavity attached near the end zone of the venturi. As they are detached they move along the flow and when they are introduced to the high compressive pressure at the outlet, they burst. Then, this phenomenon continues repeatedly.

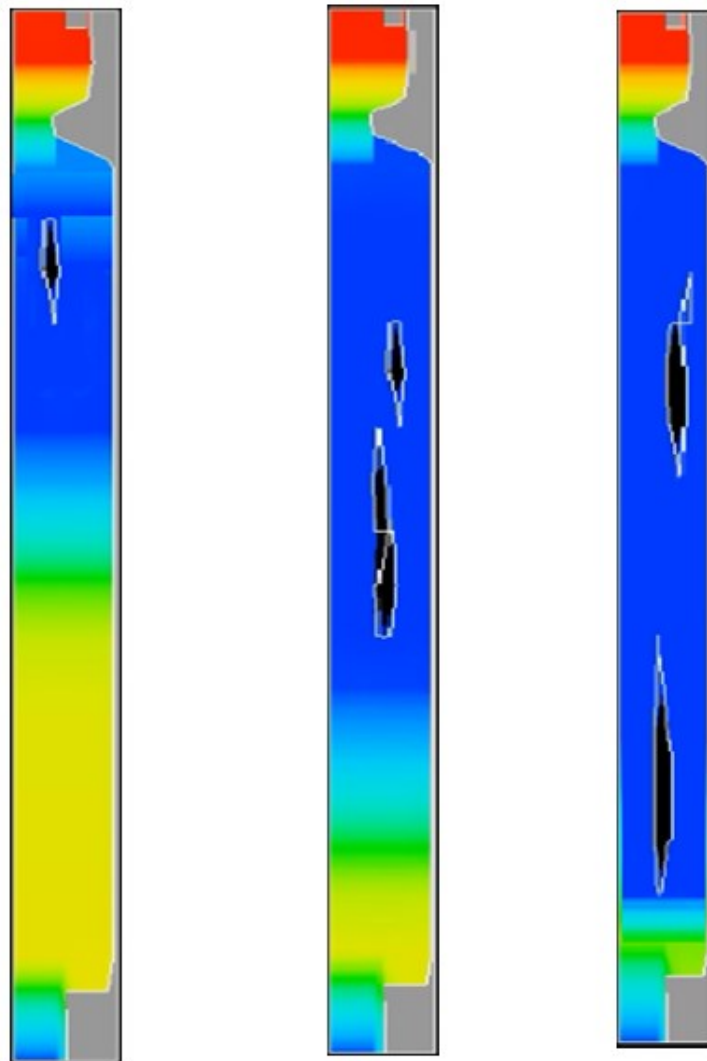


Figure 27. Detached cavity clusters travel along the pipe.

Another useful feature of the CFD is the pressure probe feature. The pressure probe can record data anywhere in the defined mesh system. Figure 24 shows the flow

direction is in z-direction in the 3D Cartesian coordinates. The unit vectors i , j , and k represent the x, y and z directions respectively. The plots in Figure 28 show different locations of the pressure probe along the z direction with fixed x and y direction. Moreover, i and j are kept constant and pressure probe is moved along k , recording the pressure fluctuation during simulation time. The peaks in pressure represent the burst of bubbles inside the flow pattern.

As the plots show, the simulation duration is 41 seconds. The outlet boundary condition is atmospheric pressure. This represents the situation in which the flow is passing through the venturi and the pipe and discharged into the open atmosphere. Many different scenarios were defined and tested. The best results were obtained by setting flow rates for inlet as the boundary condition. Plots in Figure 28 are for flow rate of 15 USGPM for the 4 mm venturi which is the condition in which cavitation begins.

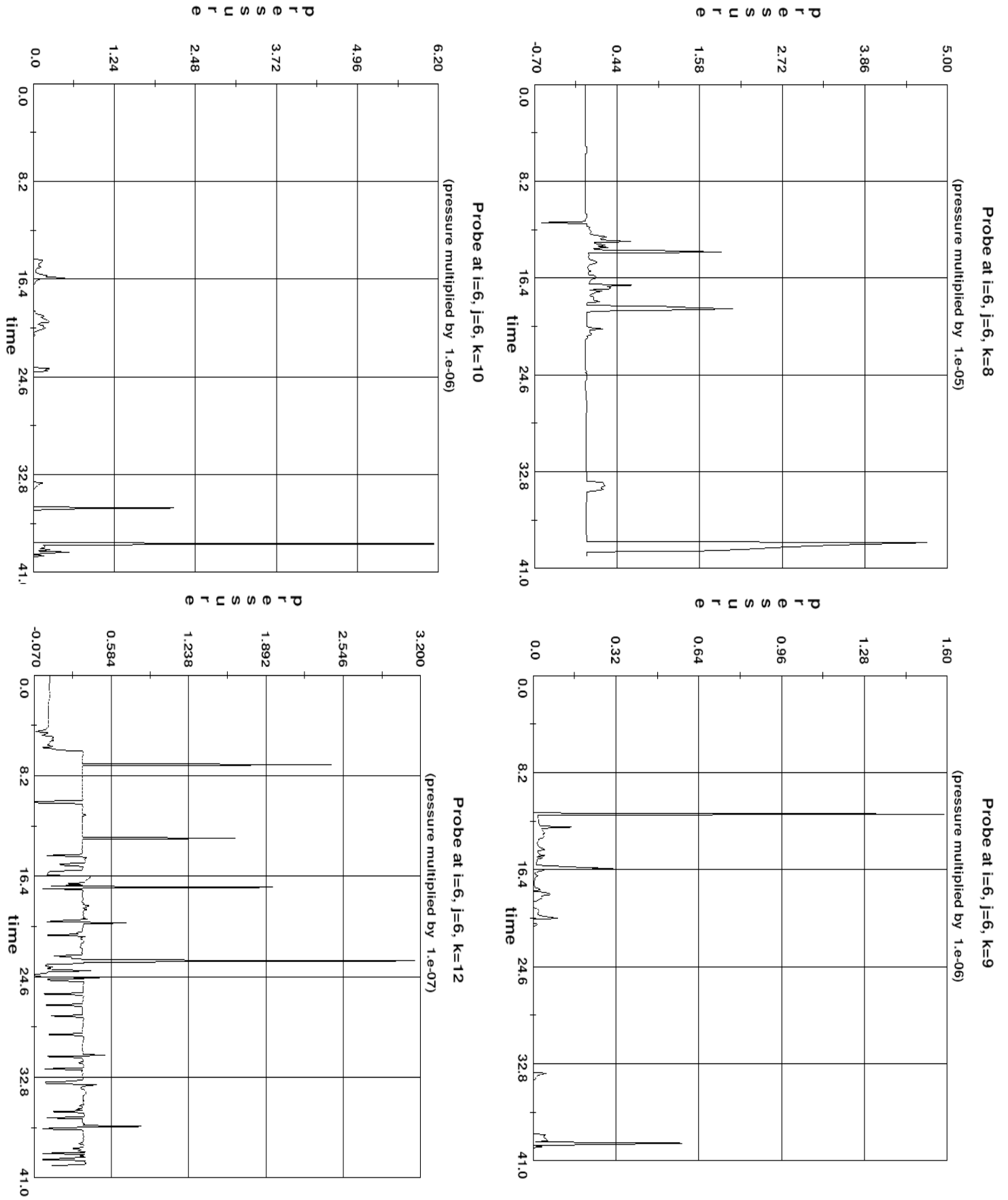


Figure 28. Pressure peaks and flow pressure behavior at different locations after venturi.

3.3 Simulations results of the 12 mm venturi

Simulations for the 12 mm venturi and later on for the 8 mm venturi insert in drilling string continued with Autodesk CFD. This software provides accurate fluid flow tools to help predict and evaluate prototype behavior and assist in optimizing the design before manufacturing. It utilizes the vertex-centered meshing for complex geometries. The solving method used is Finite Volume Method (FVM). FVM is a discretization method which is well suited for a large range of problems especially for complicated geometries. In vertex-centered FVM, the control volumes are centered on the vertex and the cells are divided into sub control volumes [26]. Additional features in post-processing in order to better understand the results, and flexible and numerous boundary conditions are also achievable with Autodesk CFD.

Figure 29 shows the drawing of the 12 mm venturi. This venturi as mentioned before is made replaceable. Hence, it could be placed into the testing frame conveniently and be replaced to test the other venturi.

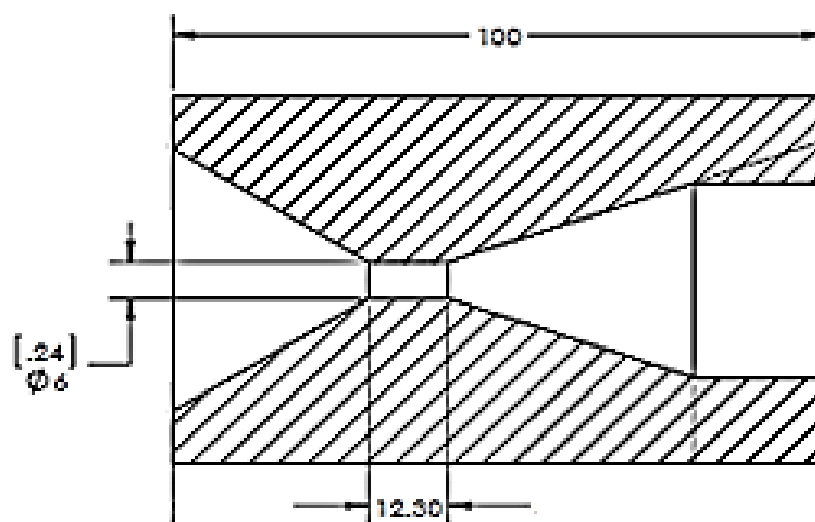


Figure 29. Schematics of 12 mm venturi.

The sections before and after the venturi are two 2-inch stainless steel schedule 80 pipes. The material defining is an important step with Autodesk. Since different materials have different roughness values and this can alter the turbulence of the fluid flowing past the conduits made with these materials.

Post-processing and visualization of the results is the last important step in CFD simulation. Particle tracer is one of the useful features of Autodesk CFD. The concept of particle tracing is similar to an injected dye stream in flow. This helps in better understanding of the flow by visualizing streamlines of the flow and flow movement. By default, these particle tracers have no mass; therefore, they are only influenced by flow and no other forces such as gravity [27].

Figure 30 clearly shows the converging and diverging section in which these streamlines are defined.

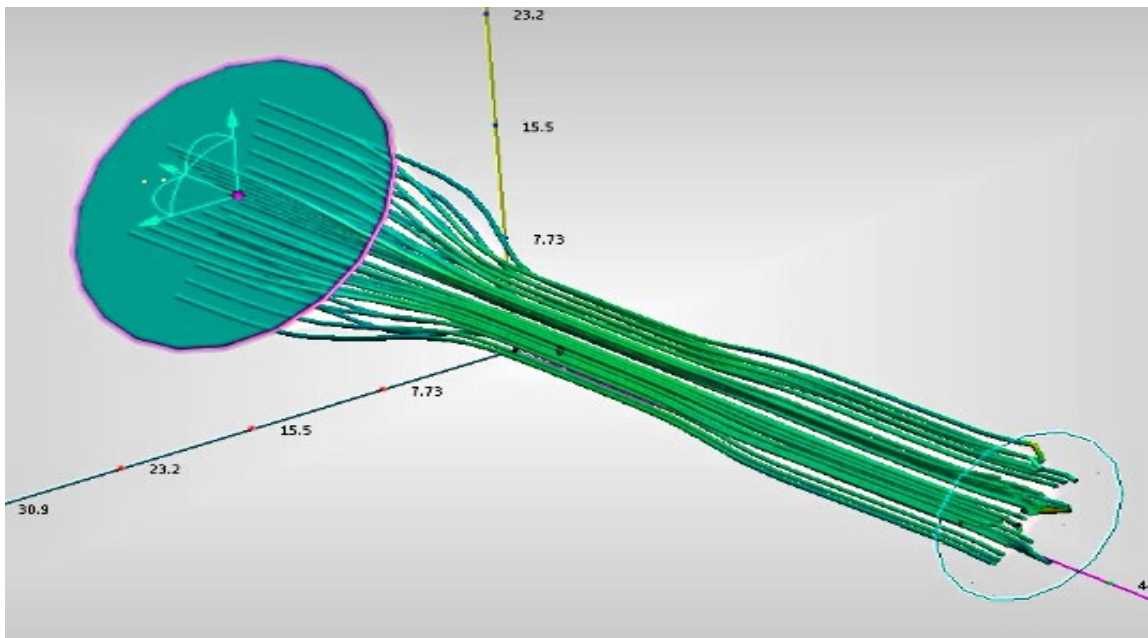


Figure 30. Particle tracing (representing flow streamlines) in simulated control volume.

The simulation result for the 12 mm venturi with fine meshing, 33 USGPM for inlet boundary condition and atmospheric pressure for the outlet are presented below. Figure 31 shows the assembly after the meshing has been applied. The meshing system of the Autodesk CFD, as mentioned before, is vertex based. Figure 31 shows the fine tetrahedral meshing of the system. The figure presents the discretization of the computational domain. Although the software adapts the results to converge the solutions, prior to the simulations robust meshing was applied before any simulation. The minimum number of nodes for discretizing was between 50,000 to 80,000 elements.

In order to reduce the uncertainty level and be able to reach to converging solution, the computational domain was chosen to be long enough, especially after the venturi. Two different scenarios of steady and unsteady were studied and the results were compared to understand which results are more realistic. In Autodesk CFD, it is possible to apply more than one boundary condition to better control the solving process. The boundary condition atmospheric at the outlet is not a fixed B.C and refers to the situation in which the flow is running to an open tank in atmospheric condition.

These boundary conditions are the simplified conditions in which the tests were conducted. The presented pressure patterns are also representative of a transducer just before outlet of the assembly to capture the pressure fluctuations.

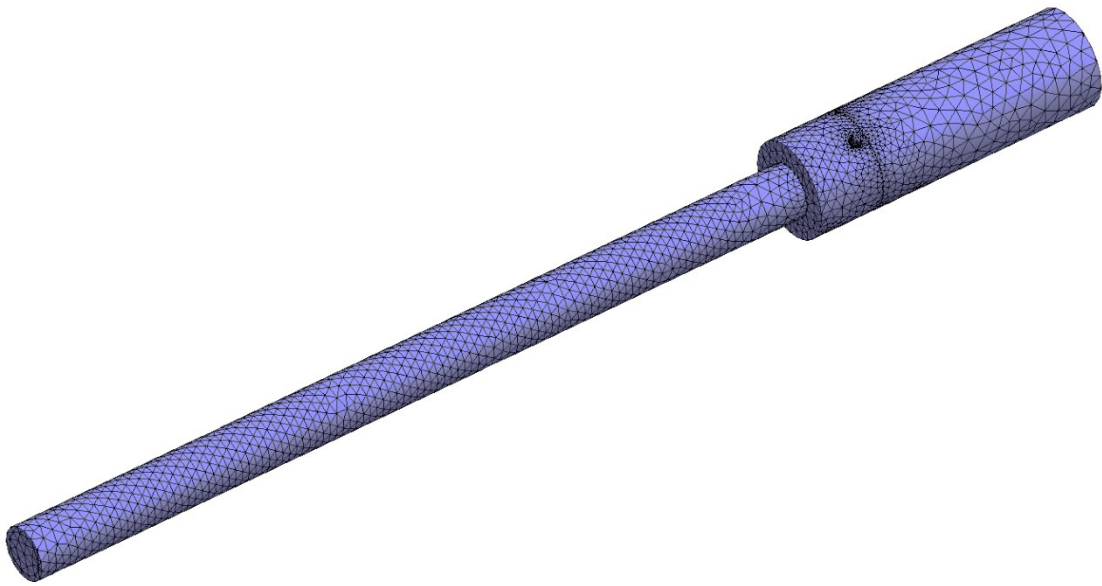


Figure 31. Tetrahedral meshing of the assembly.

After the meshing task has finished, the software starts to solve the Partial Differential Equations (PDE) defined for the model. The B.C. values are the initial condition values for these differential equations. At each step, properties of each node are approximated from the initial nodes and this progress continues until it reaches to the last nodes located at the outlet. Then adaptation begins and when the results converge, simulation stops [28]. The next step is the post-processing and visualization of the results.

Figure 32 is the 3D profile of the liquid. This figure represents the Volume of Fluid (VOF) for current simulation. The VOF range is from 0 to 1, $0 < \text{VOF} < 1$.

When VOF is 1, the fluid is 100% liquid and if VOF is 0, the fluid is 100% vapor. In Figure 32, Image 1 represents the initial condition in which fluid starts to move towards the venturi and it has not been fully developed. The fluid has entered the venturi and the pressure reduction process has started. The fluid color change from red

to yellow represents the initiation of vapor creation. Image 2 represents the flow condition after a few steps.

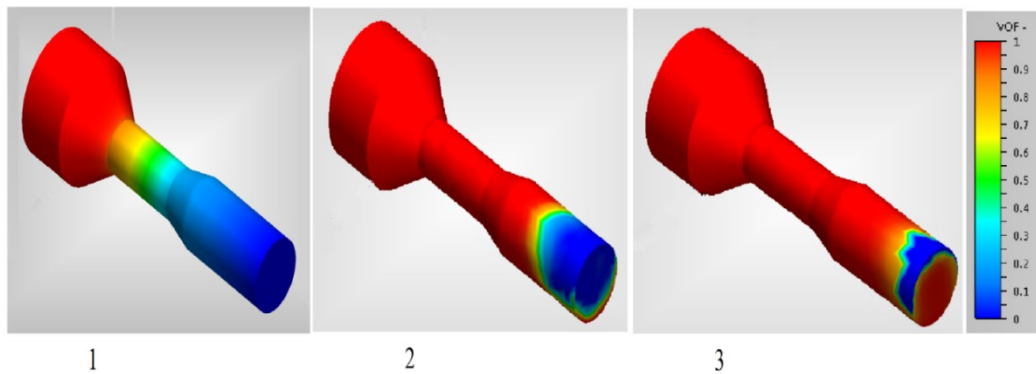


Figure 32. VOF results of the simulation presenting liquid vapor after venturi.

In this Image a portion of the fluid filled with bubble clusters is at the end the assembly. When this portion is introduced to high compressive pressure at the end of the pipe, bubble clusters begin to implode and emit pressure waves and pressure peaks. This is observed with the pressure probe at the end of the model.

Figure 33 shows the pressure contours at the outlet of the model. In this figure, the location at which the bubbles burst is shown. The high pressure is represented by red color and low with blue. As the bubbles flow inside different portion of the liquid, they flow in an irregular path. Figure 33 shows that the main reason of the bubbles collapse is due to collision with the pipe wall at the outlet. The high pressure contours in the midsection are present due to the fact that the pressure outside the bubble wall was higher than the pressure inside the bubble. This results in the implosion of these bubbles.

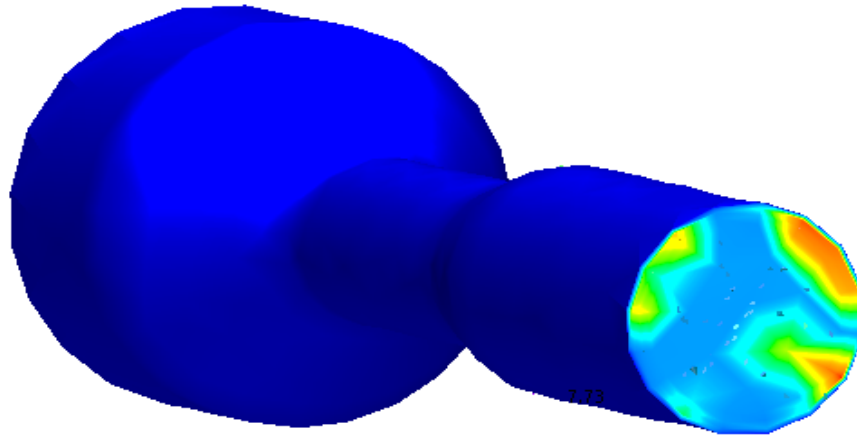


Figure 33. Front view of the tool outlet with pressure contours.

Other than 3D representation of the flow, it is also possible to study the flow behavior in a specific cross section plane. The most efficient way is to study the result on the plane passing from the middle of the model. This plane divides the model in half and basically represents the model in 2D. Figure 34 is the 2D representation of the model which shows cavitation vapor volume of the fluid (CVF) and it illustrates the presence of liquid vapor due to cavitation process.

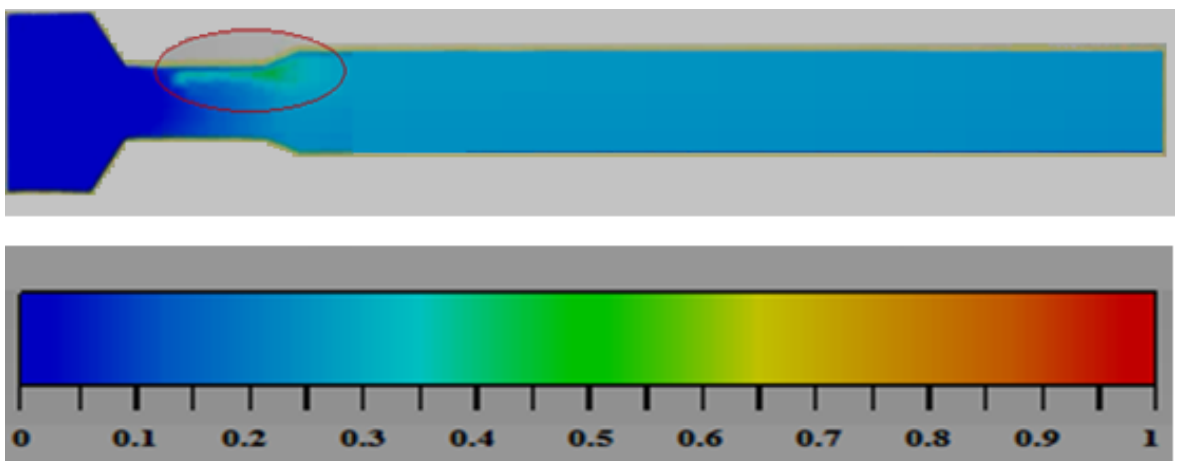


Figure 34. 2D representation of Cavitation vapor volume fraction inside 12 mm venturi.

CVF ranges from zero to one. Zero represents the condition in which there is no cavity and fluid is liquid. When the fluid passing is 100% cavity or vapor, CVF is one [27]. Figure 34 shows that the fluid before the venturi is liquid with no cavity and CVF is zero.

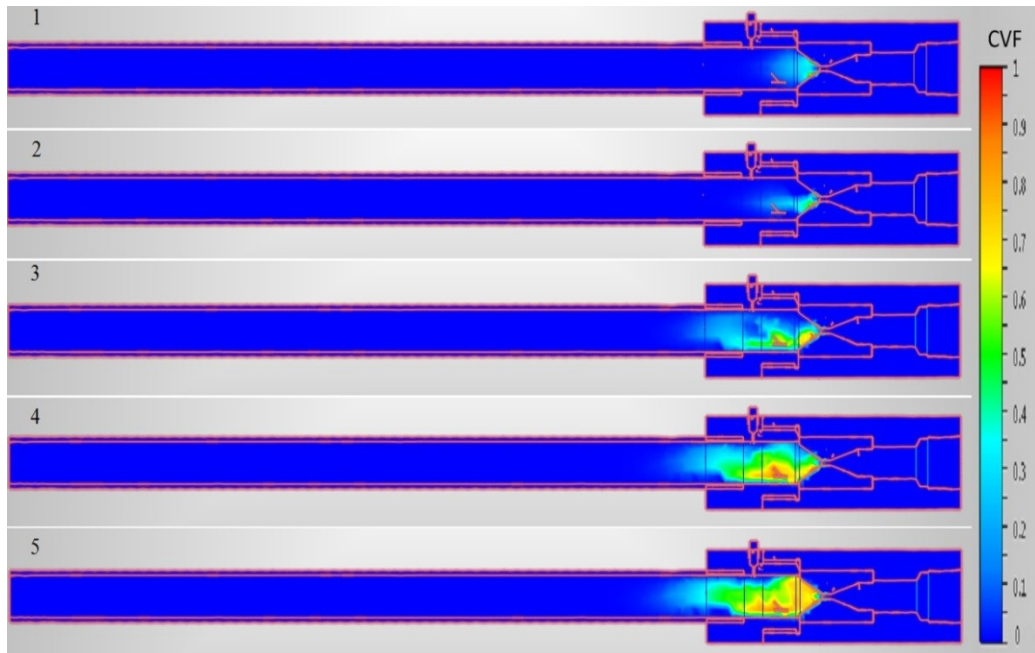


Figure 35. Fixed cavity growth inside 12 mm venturi represented with CVF.

After the fluid passes the constriction, pressure is reduced and cavities start to grow and the CVF changes from 0 to 0.5 at the outer part of the venturi. Figure 35 shows the sequence in which the bubbles are created and start to grow. This figure shows that the CVF is at the outlet of the venturi is increasing. In this figure, Image 5 shows the last step in which the fixed vapor volume is in its largest possible volume and bubble clusters start to detach after this step.

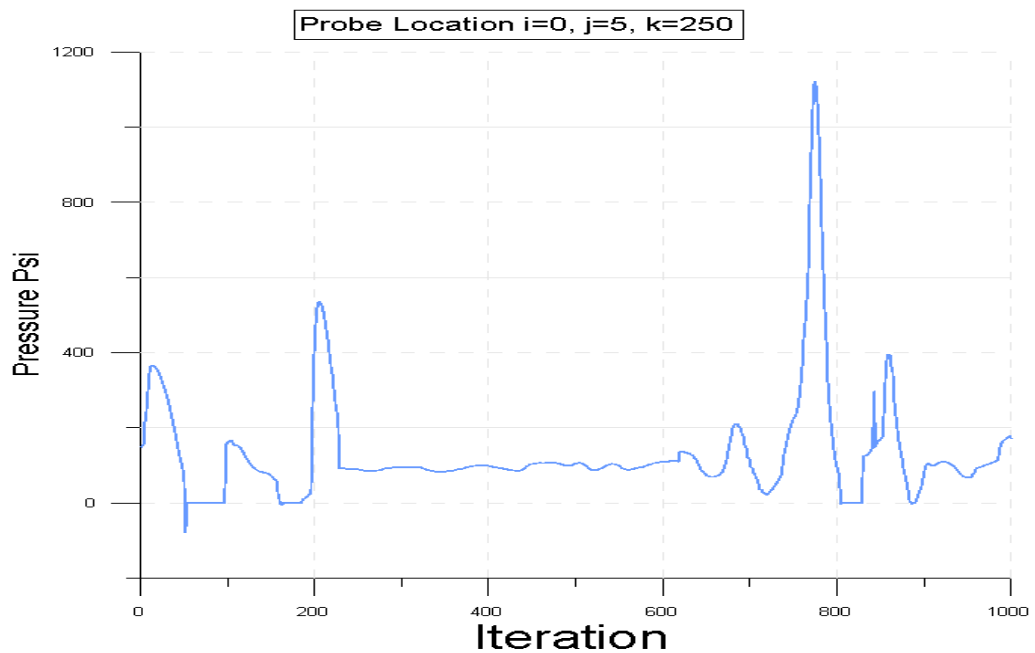


Figure 36. Pressure recorded with probe at k=250 after venturi.

Graphical visualization is a good way to present the results for CFD simulations. However, we can also extract the numerical values of the simulation from different probes that record various features such as pressure, velocity magnitude, density, VOF, CVF and many other properties. Figure 36 shows the pressure fluctuation of the model recorded with the pressure probe located at $i = 0$, $j = 5$ and $k = 250$. This probe is located downstream of venturi and recorded the pressure fluctuations due to bubbles collapse.

As the flow passes by the constriction, more bubbles are created. This makes the flow to change from single phase liquid to a 2-phase fluid filled with cavities. As we discussed before, the cavitation phenomenon is discrete and cavity pockets created are scattered inside the liquid phase. Figure 37 shows the CVF probe located at $i \approx 0$, $j = 5$, and $k = 302$. The fluctuation in CVF represents the irregular pattern of bubbles

detachment from the fixed cavity. The CVF probe after the venturi is measuring the detached cavities fraction inside the liquid.

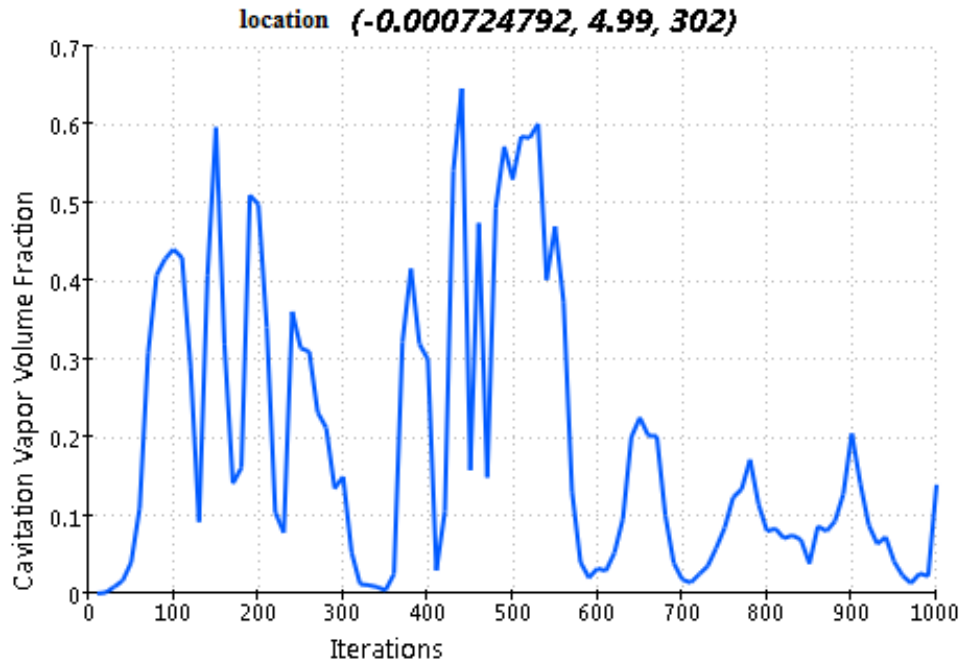


Figure 37. CVF presentation of flow at k=302.

There is an interesting relationship between density and the CVF. As the CVF increases this means that the percentage of the vapor is increasing in a specific volume of a fluid. Since the density of vapor or gas is much less than the density of the liquid, the total density of the fluid goes down. Moreover, increase in CVF, results in reduction in density. The simulation results show that when the CVF is high, the density is low and when the amount of vapor is very low, the density of the fluid is close to the density of the liquid. Figure 38, represents the density probe after the venturi located at $i = 0$, $j = 5$, and $k = 302$.

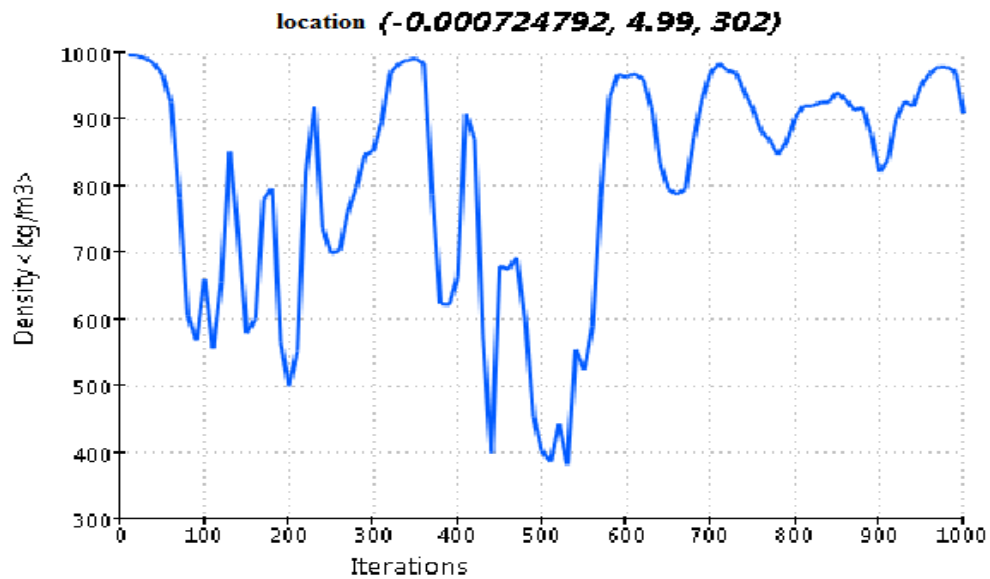


Figure 38. Density of the flow at k=302.

The plot shows that at the beginning of the simulation and before the flow is fully established, the density is 1000 kg/m^3 . After the bubbles are introduced to the flow, ρ decreases and then starts to fluctuate. Another fact is that there are times that ρ gets close to 1000 Kg/m^3 but never equals to 1000 Kg/m^3 which means that there are cavities inside the liquid all the time. Comparing the CVF plot and density plot, it can be concluded that these plots are the mirror image of one another. Due to rarefaction of the liquid by invasion of the bubbles, the fluid gets less dense. The driving force of the fluid, which provides 33 USGPM of flow, has remained constant. According to the Newton's 2nd law, $F = ma$, if F is constant and m is reduced then the acceleration and hence the velocity of the fluid will increase. The increase in velocity of the fluid also is the result of the rarefaction of the liquid by invasion of the bubbles which makes the fluid lighter. Figure 39, shows the behavior of the fluid velocity recorded at the same location where other properties were measured, $i = 0$, $j = 5$ and $k = 302$.

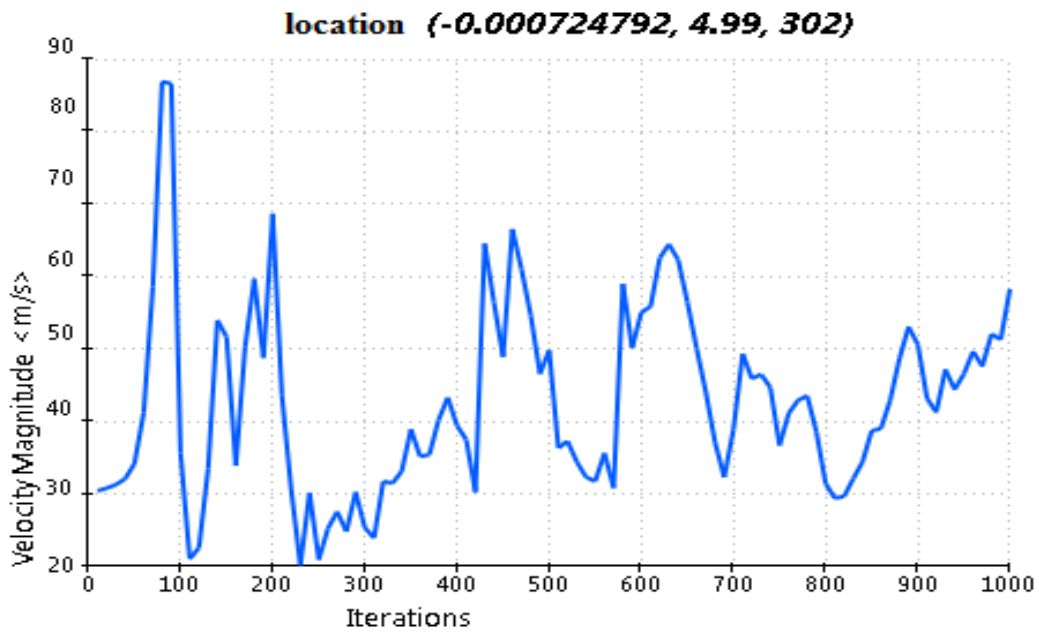


Figure 39. Velocity magnitude of the flow at K=302.

The minor fluctuations are due to the fact that the flow is turbulent. If the flow was a single phase, the pattern would be a straight line with minor fluctuations due to turbulence and the average velocity would be much lower.

3.4 8 mm venturi insert in drill pipe simulation

An 8 mm venturi insert for drilling purposes was also designed. Figure 40 is the drawing of the tool assembly in which the venturi is located.

Figure 41 shows the specific dimensions of the venturi. The venturi is located after the swivel where the venturi outlet is connected to the drill pipe which is connected to the drill bit. The flow passes through the venturi and the drill pipe and is discharged from the bit.

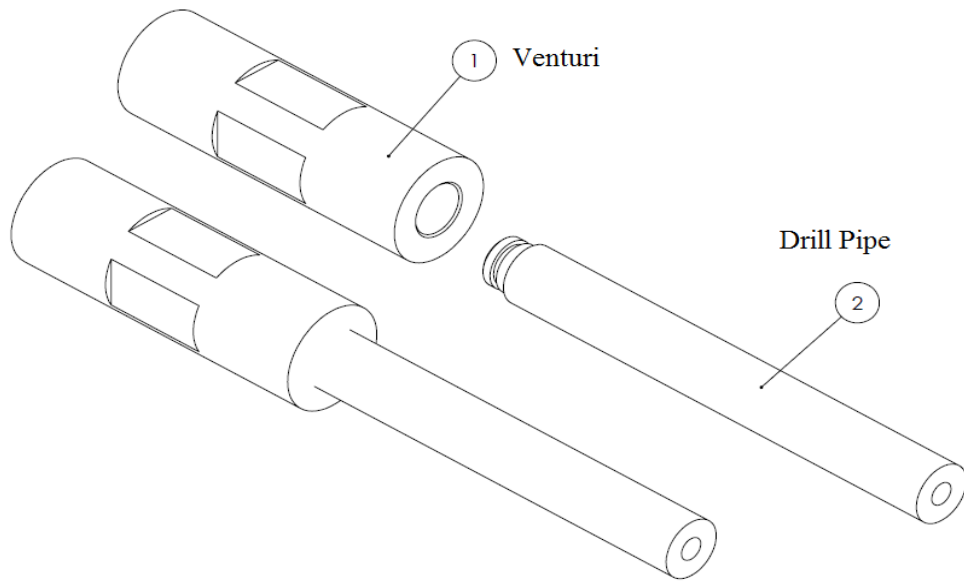


Figure 40. Exploded View of the venturi insert for drilling setup.

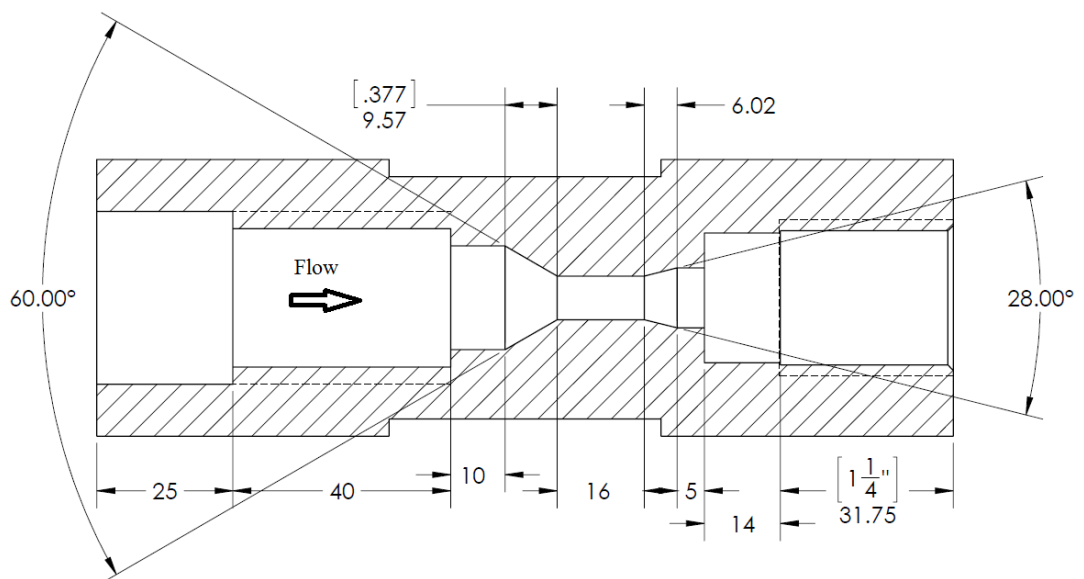


Figure 41. Dimension of 8 mm venturi.

Autodesk CFD was used to simulate the flow behavior inside the tool. Figures 42 and 43 show the results for 20 USGPM inlet flow and atmospheric pressure for the outlet with a robust fine meshing system. Figures 42 and 43 show the cavitation vapor volume fraction in the 3D format.

Figure 42 shows that the initiation of cavitation phenomenon is in the throat section of the venturi. A lot of bubble clusters are created in this step. In the next step which is shown by Figure 43, these bubbles are detached from the fixed cavity in the throat section and are carried away by the flow and burst after they are introduced to the high pressure environment.

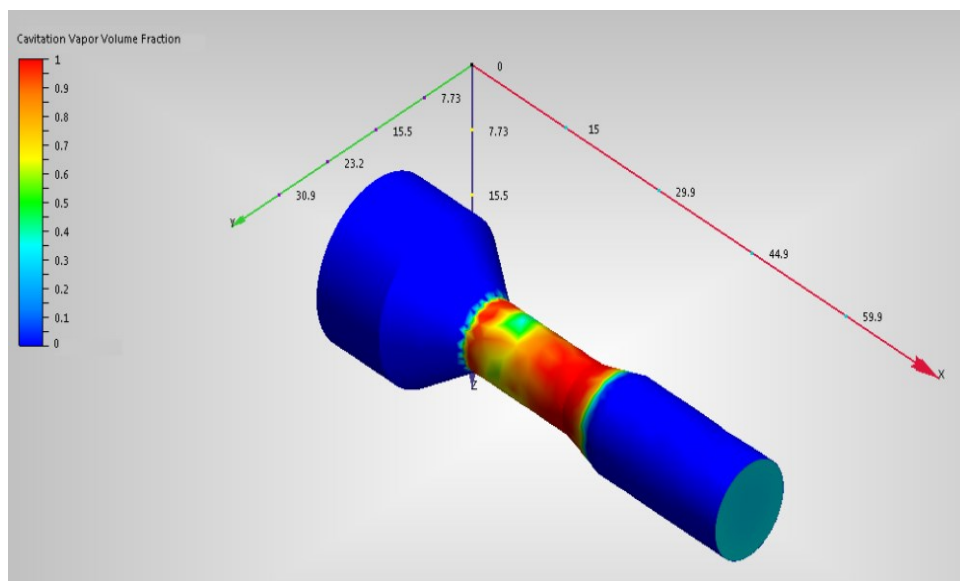


Figure 42. Cavitation initiation in 8 mm venturi throat section.

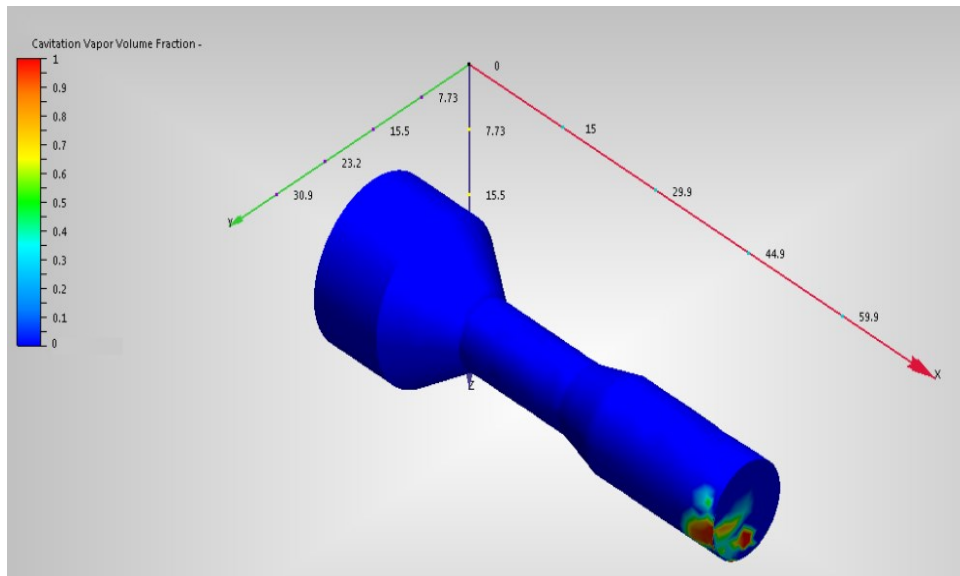


Figure 43. Bubble cluster detached from venturi throat, exiting venturi.

As discussed before, the VOF feature dynamically simulates the interface between liquids and gases. Figure 44 shows the liquid-cavities interface for the same steps in the same simulation model.

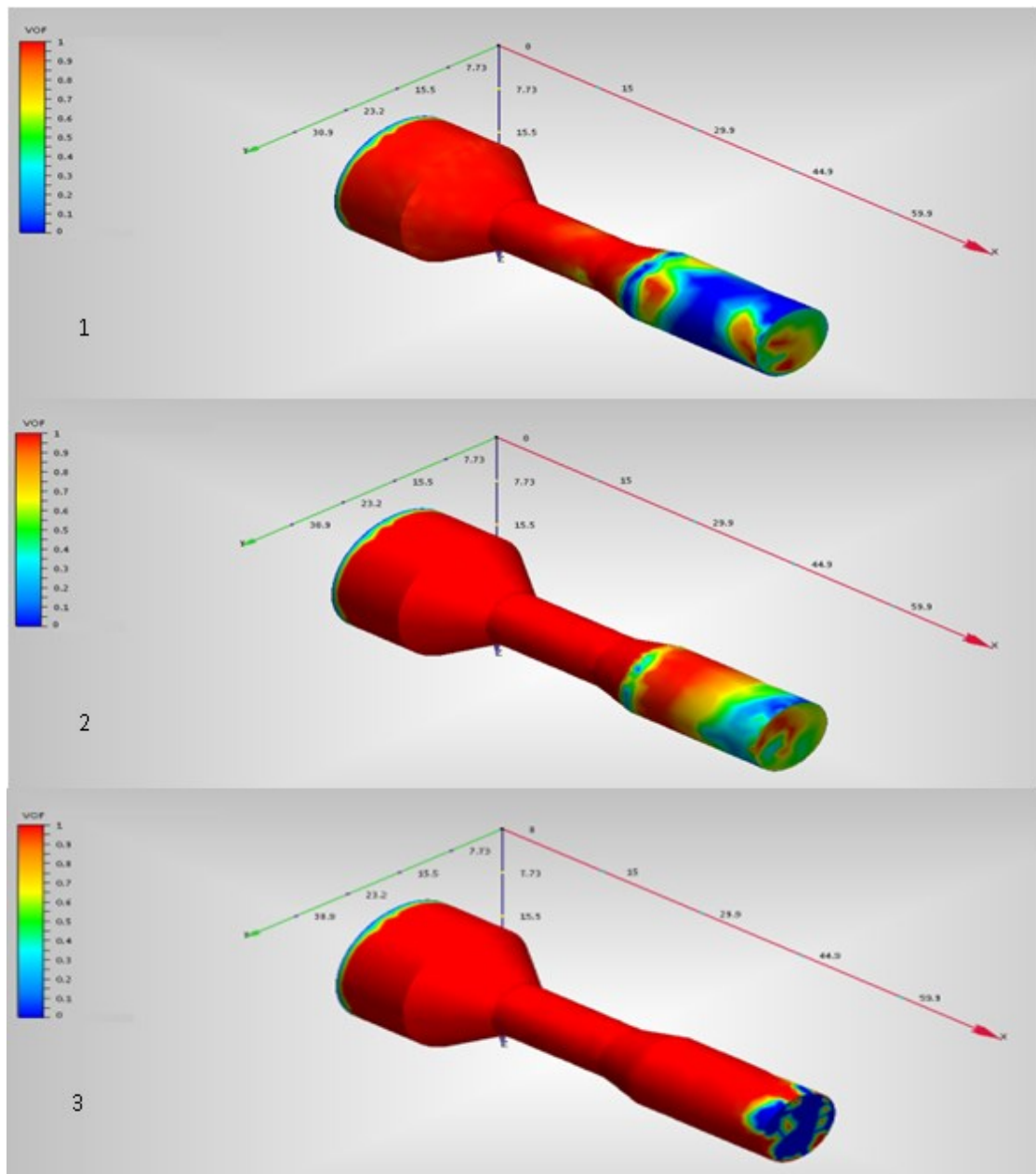


Figure 44. Cavity clusters exiting the venturi after shedding presented by VOF.

Figure 44 shows the bubbly flow after the venturi. In this figure, the bubble clusters created at the venturi are carried in the drill pipe. This figure basically is the VOF representation of the flow. $VOF = 1$ represents single liquid and $VOF = 0$ represents vapor flow.

As it is observed in Figure 45, the flow after the venturi is a mixture of liquid and vapor along the drill pipe. The flow is basically two phase consisting of water and its vapor.



Figure 45. Vapory texture of the flow after venturi.

Rarefaction of the liquid and pressure surges due to bubbles collapse increases the fluid velocity. For the 8 mm venturi with 40 USGPM flow rate, the velocity in case of single flow with venturi is 50.2 m/s in the throat section. However, with the cavitation phenomenon occurring in this model the fluid velocity reaches magnitudes up to 154 m/s.

This velocity is 3 times greater than the condition in which there was no cavitation. Figure 46 shows the velocity profile of the flow while Figure 47 shows the pressure history of a point after the venturi. The pressure probe recorded the fluctuations of the outlet pressure for 55 seconds.

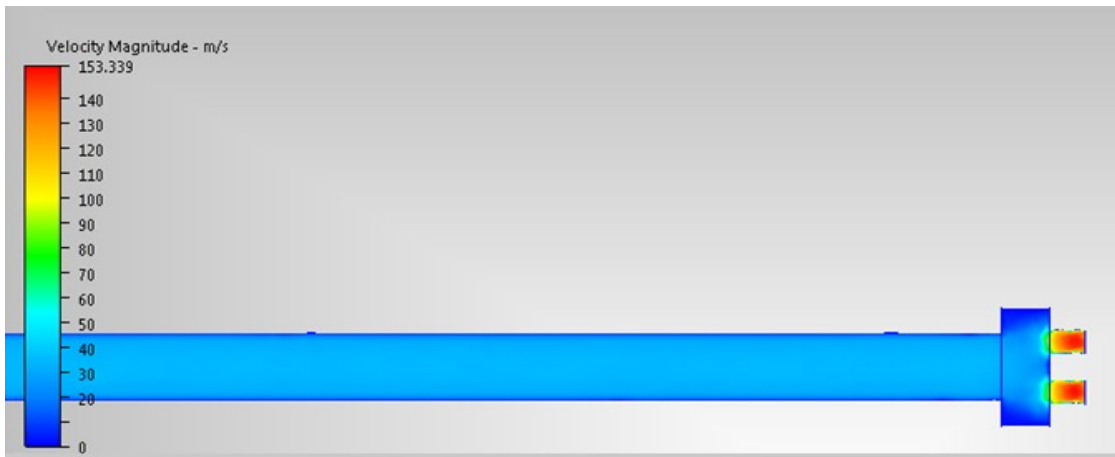


Figure 46. Fluid velocity profile

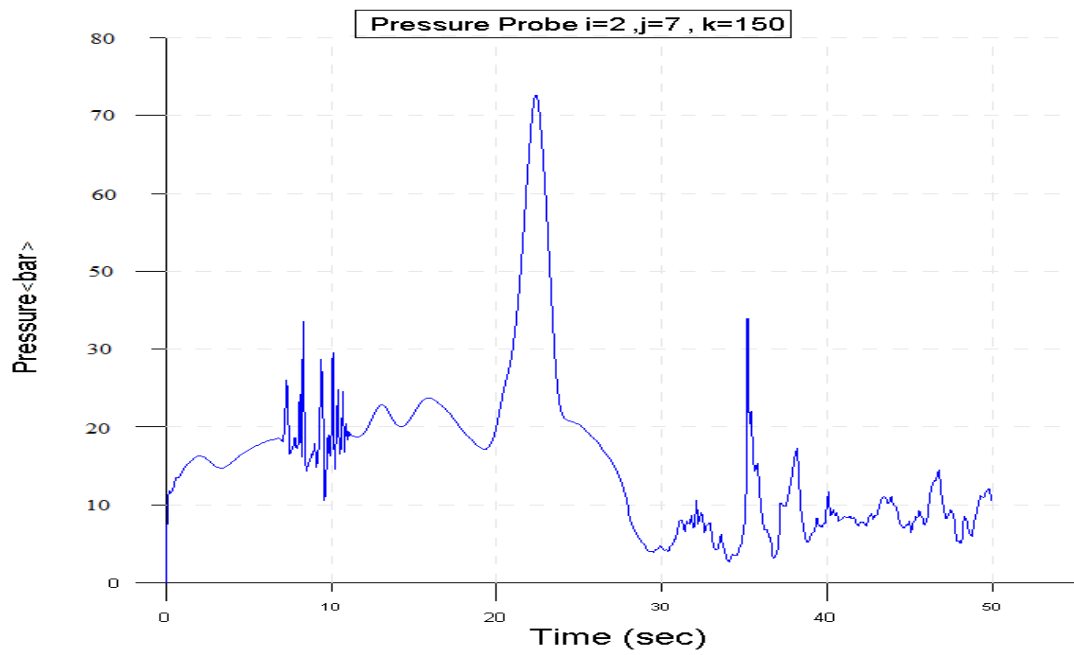


Figure 47. Pressure fluctuations of the fluid at k=150.

Overall the pressure behavior inside the assembly along the z-direction is shown in Figure 48 which shows that the pressure decreases when it reaches the venturi, then it is recovered after it has passed the constriction section.

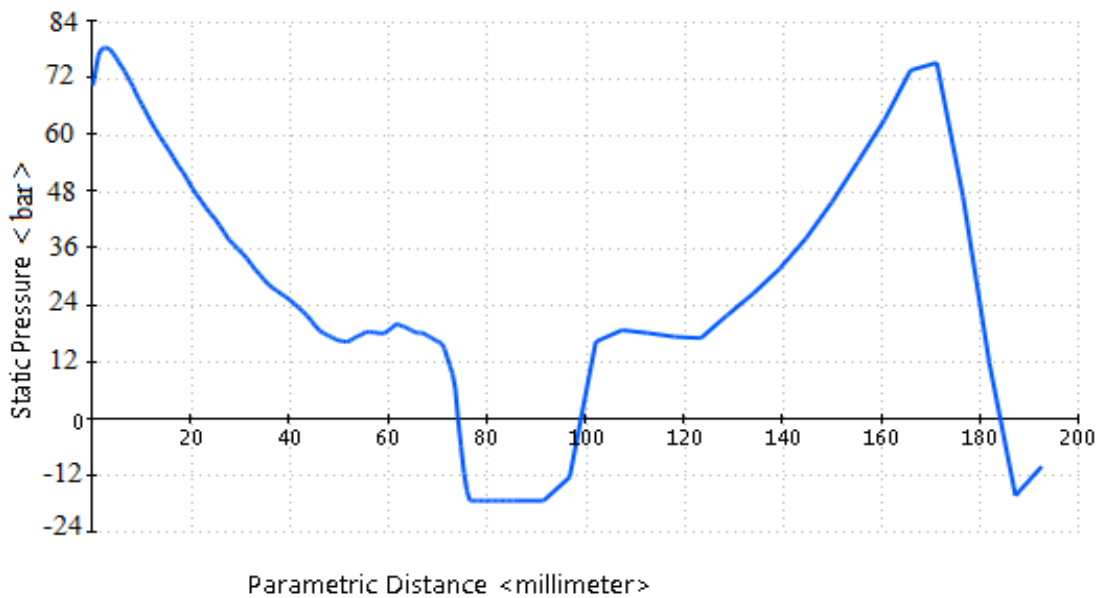


Figure 48. Venturi pressure profile along tool length.

Figures 49 and 50 show the density and cavitation vapor volume fraction features of the flow. As discussed before, these two probes are related to each other inversely. When density is at its highest value, the CVF fraction is at its lowest and vice versa. Analyzing the data shows that overall trend for density is decreasing and hence more bubbles are produced as the simulation continues. Density values also show that cavitation bubbles rarefy the water up to 10 times which means 90% of the flow at the recorded instant is vapor.

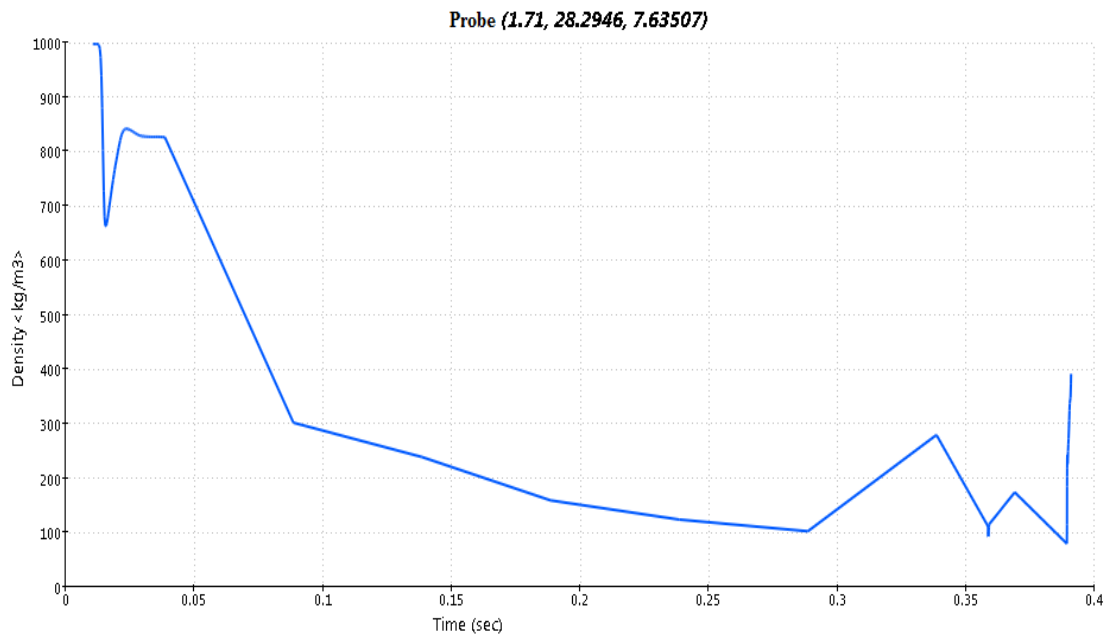


Figure 49. Fluid density after venturi during simulation time.

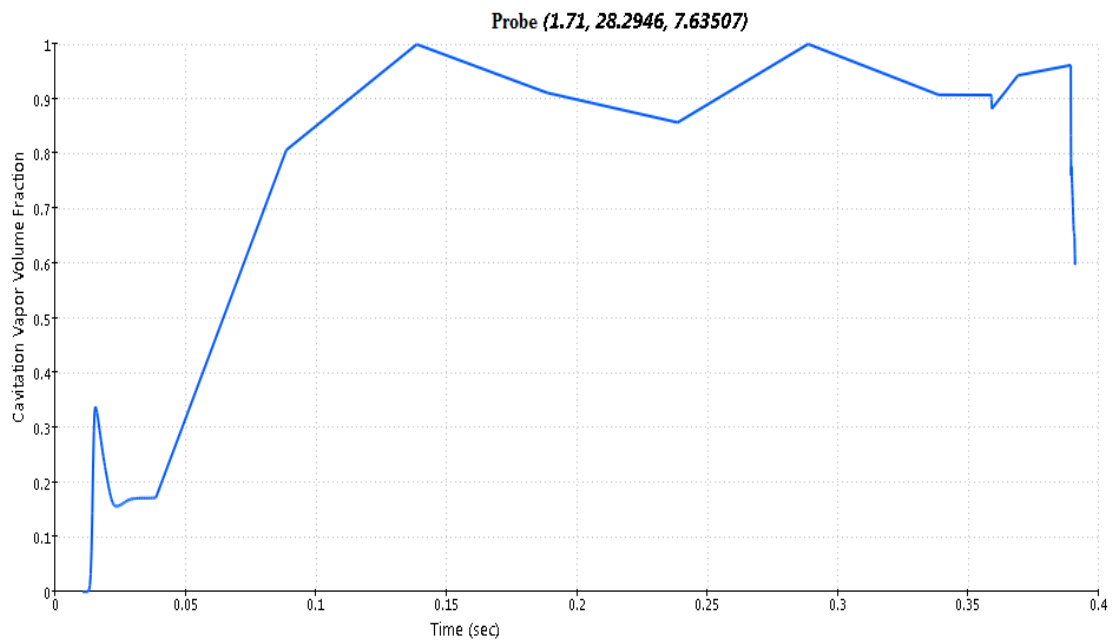


Figure 50. Cavitation vapor volume fraction of the fluid after venturi.

Continuing the simulations to confirm the result obtained with another software, the same model of the 8 mm venturi was imported to Flow3D software. Same conditions for B.C were applied. The meshing system was tuned to be in its optimum condition which is fine meshing with good tolerance to accurately reflect the flow geometry.

Applying the same B.C and using the mesh, the model was studied with cell-centered simulation scenarios. After the simulations were done the results were in agreement with those obtained from Autodesk CFD software.

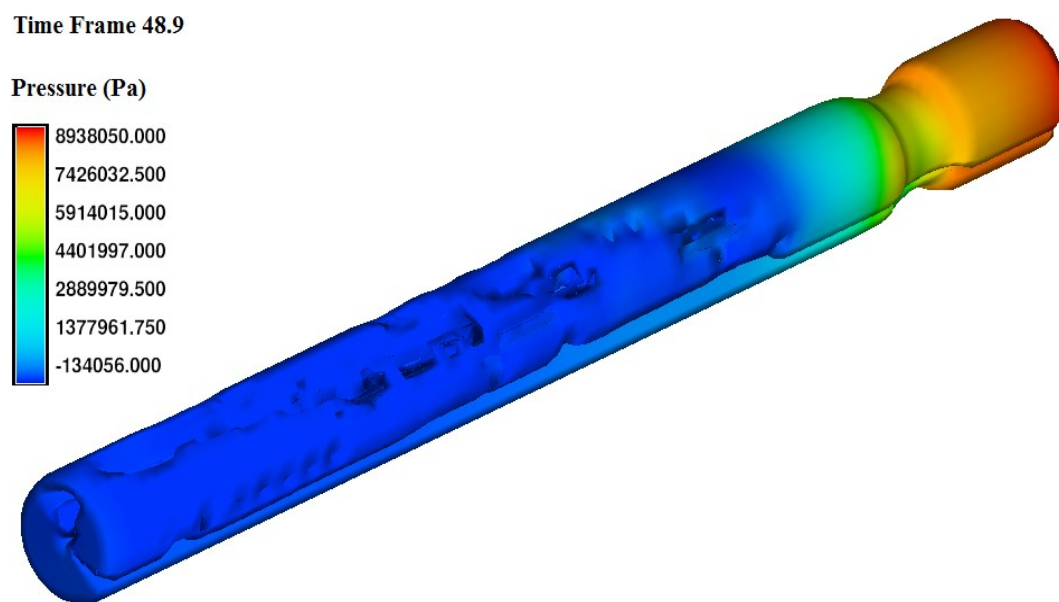


Figure 51. 3D representation of the cavitation clusters with pressure contours in 8 mm venturi.

Figure 51, shows the pressure contours in the 3D representation of the computed domain. The ripples in the surface are the bubble clusters moving along the drill pipe at the interface of fluid and the pipe surface.

The pressure probe located at $i = 7, j = 17, k = 27$ has recorded the pressure history of the flow. This is summarized in Figure 52.

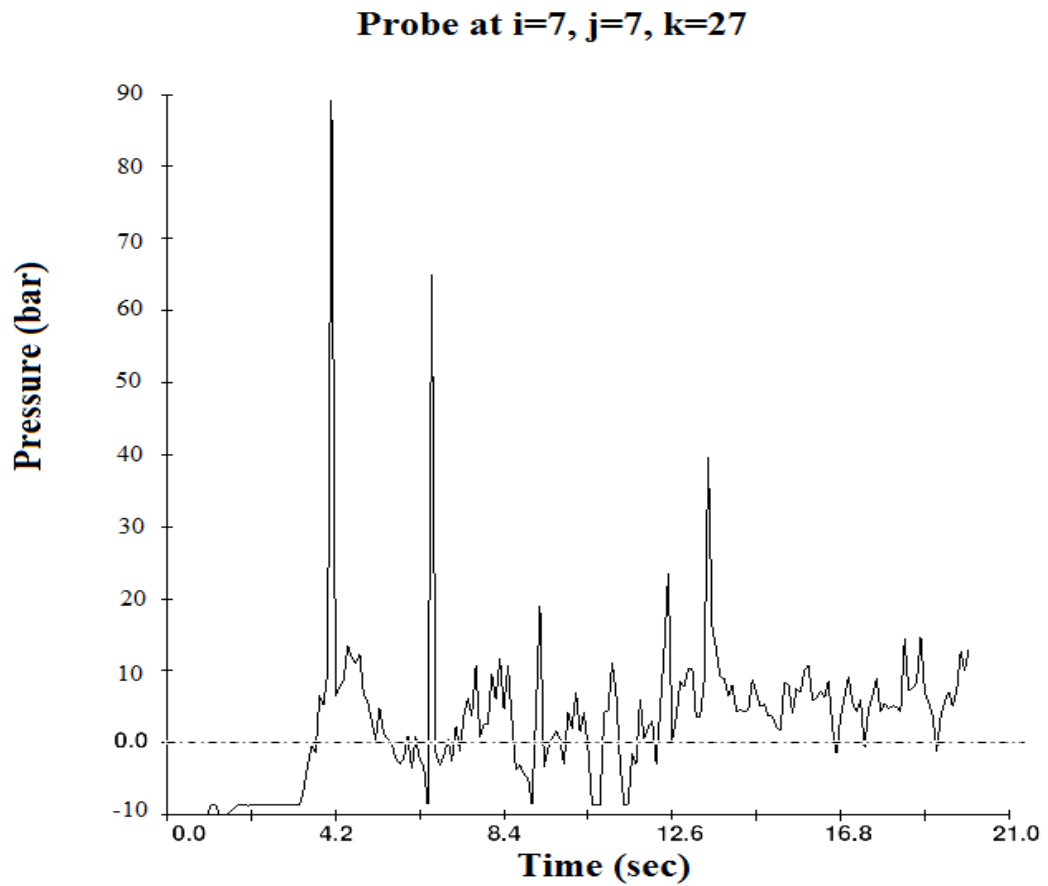


Figure 52. Pressure probe fluctuation at $k=27$ after venturi during 21 s simulation.

Simulations confirm that the cavitation occurs in all of the venturis fabricated. Using two different simulation software packages confirmed this idea. Simulating with Flow3D and Autodesk CFD confirmed that the results are valid since the results obtained were in close agreement to each other. Different features of the softwares gave us better understanding of the phenomenon. Comparison of fluid density values before and after the venturi, confirmed the existence of cavity clusters after the venturi because of cavitation. This was also true for CVF values. The pressure probe data confirmed the pressure peaks due to the collapse of bubbles clusters.

CFD simulations helped us predict what is happening in reality and how the fluid properties change during the cavitation phenomenon.

4. Pulse Cavitation Tool Experiments

In this chapter, the experimental setup for early investigation of the pulse cavitation tool is described. The different factors and their effect on cavitation phenomenon are studied. The test frame used for this set of experiments is designed to investigate the different features of the cavitating flow such as pressure pulses and corresponding induced forces.

4.1 Testing setup description

The test frame as shown in the Figure 53 consists of a network of pipes to control the inlet flow to the cavitation segment of the assembly. This part of the assembly is shown in Figure 54.

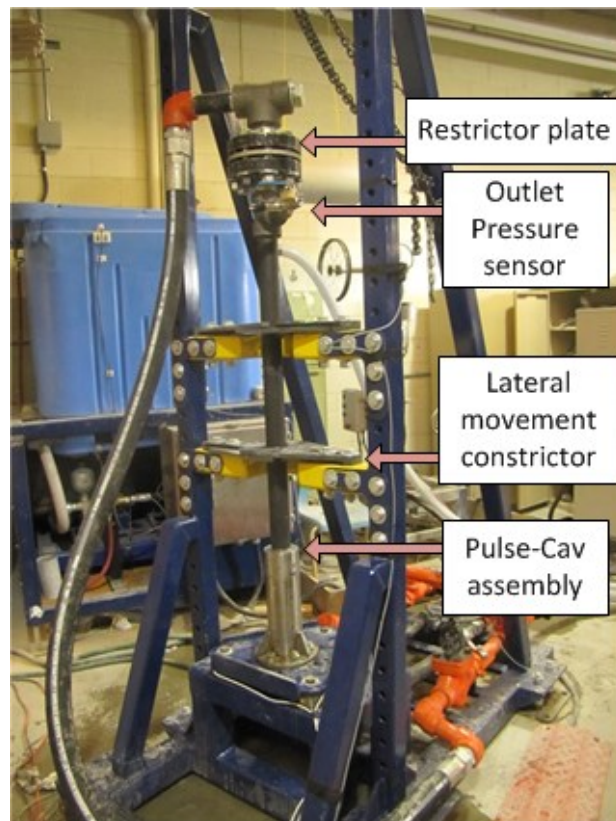


Figure 53. Test frame components.

It consists of safety valves to circulate the flow back to the pump in case of any problem occurring during testing. This section is designed to let the flow into the system and recirculate it back to the tank feeding the pump. There is a needle valve to apply back pressure to the flow assembly. A flow meter and a pressure transducer are installed on this section to measure the flow rate and inlet pressure of the system.

The flow in this system is upward opposite to the direction of gravity. This assists in removing the effect of gravity in pressure calculations.

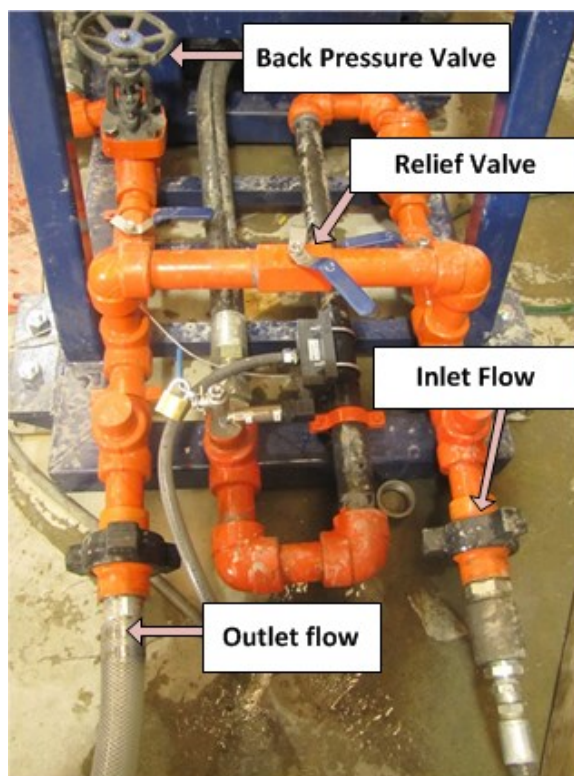


Figure 54. Test frame piping section.

Lateral movement constriction is applied via triangular plates as shown in Figure 53 to avoid any lateral movement of the assembly. The main housing of the assembly is attached to the triangular plate which supports 3 different load cells recording forces induced by the flow inside pulse cavitation assembly.

A restriction plate is installed at the end of the pipe connected to the assembly as a representation of a drilling bit. The restriction plate is shown in Figure 55. The restriction plate represents a drilling bit with 3 nozzles. The plate is used to convert the pressure pulses produced by the pulse cavitation tool to forces acting on the bit. These force fluctuations act as the secondary source added to the WOB.

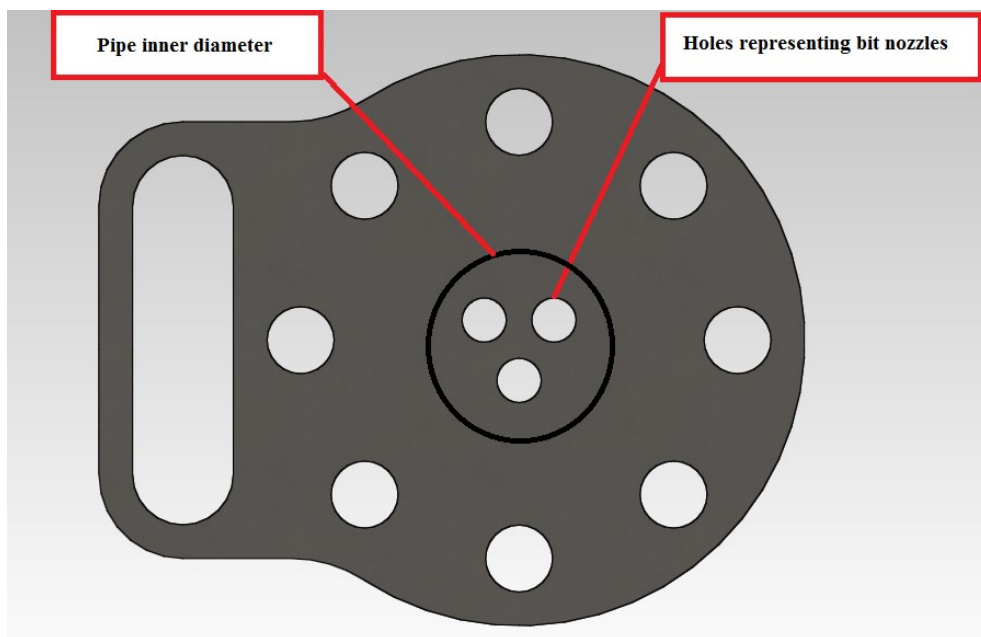


Figure 55. Restriction plate schematics.

4.2 Data Acquisition (DAQ) System

The testing frame was connected to a portable DAQ system which facilitated conducting the experiments outside the lab. The power supply for the DAQ is water proof. Figure 56 shows the power supply and DAQ system connected to a computer recording the data.

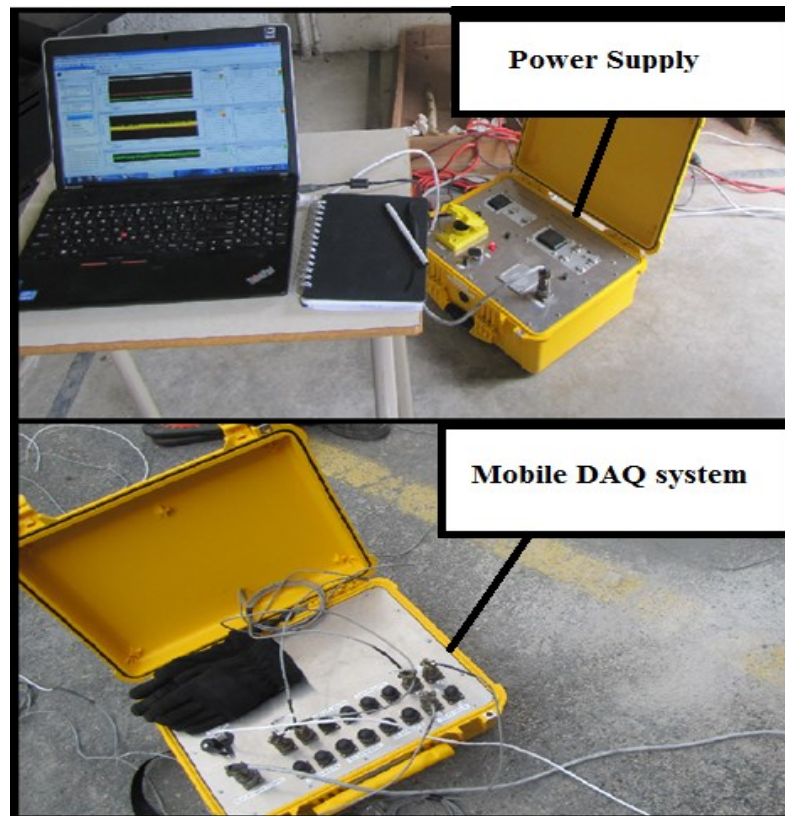


Figure 56. Mobile DAQ system and its power supply.

4.3 Sensors

For conducting the experiments, 6 sensors were used. Two pressure sensors were used to measure the inlet or upstream pressure and outlet or downstream pressure fluctuations. Three load cells in a triangular configuration were used to record the forces generated by the tool. A flow meter was also used to measure and set the flow rate according to the plan.

To measure the outlet pressure, a transducer with operating range of 0 to 4000 psi was used. For the inlet pressure fluctuations, the operating range of the pressure transducer was from 0 to 1500 psi. Each load cell has capacity of 5000 lbs., therefore, when they are added together, the load capacity of the system is 15000 lbs. As shown in Figure

57, the pulse cavitation tool is placed in the center of the plate and the generated force is divided among three load cells. Adding measured loads from each load cell, the total force generated by the tool is calculated.

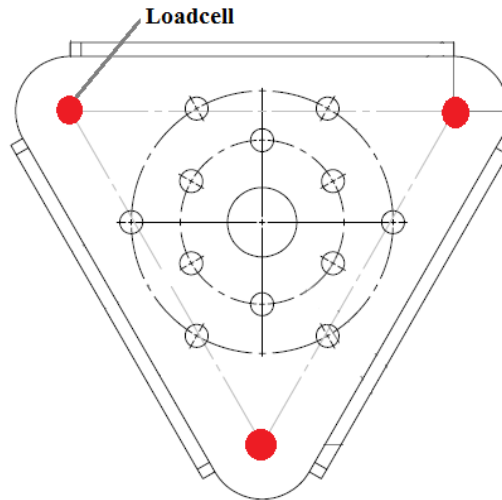


Figure 57. Triangular configuration for load cells.

4.4 Experiments plan and results

Two sets of experiments were conducted using this test frame. The first block of experiments were conducted using the triplex pump in the ADG laboratory with flow rates up to 40 USGPM and pressure capacity of 1000 psi. The pressure transducers recorded the inlet and outlet pressures of the assembly. The load cells recorded the force output of the assembly. The triangular plates used to omit any type of lateral movement assist in focusing only on axial vibration and forces produced by the pulse cavitation assembly. Both 4 mm and 12 mm venturis were used for the experiments. Table 1 shows the test matrix for these experiments. Back pressure represents the bottom hole pressure downstream of the bit.

Table 1. 4 mm venturi experiments plan.

4 mm_venturi			4 mm_venturi		
Test	Flow (USGPM)	Back Pressure (Psi)	Test	Flow (USGPM)	Back Pressure (Psi)
1	6.5	0	14	10	0
2	6.5	100	15	10	100
3	6.5	200	16	10	200
4	6.5	300	17	10	300
5	6.5	400	18	10	400
6	6.5	500	19	12	0
7	6.5	600	20	12	100
8	8	700	21	12	200
9	8	0	22	12	300
10	8	100	23	13.5	0
11	8	200	24	13.5	100
12	8	300	25	15	0
13	8	400			

Table 2 shows the experimental plan matrix for the 12 mm venturi. These plans were based on water as the fluid passing through the assembly. Also the same block of experiments was conducted using a viscous drilling fluid prepared at the ADG lab. The viscous drilling fluid was developed by mixing water with Xanthan Gum powder as the viscosifier agent. The mud was a shear thinning fluid with apparent viscosity of 5 cp. Due to the high pressure drops required to break the liquid mud bonds and hence cavitate the fluid and restriction of pump capacity, the mud did not cavitate although pumped out at high flow rates up to 40 USGPM.

Table 2. 12 mm venturi experiments plan.

12 mm Venturi			12 mm Venturi		
Test	Flow (USGPM)	Back Pressure (Psi)	Test	Flow (USGPM)	Back Pressure (Psi)
1	8	0	21	26	0
2	8	200	22	26	200
3	8	400	23	26	400
4	8	600	24	26	600
5	12	0	25	30	0
6	12	200	26	30	200
7	12	400	27	30	400
8	12	600	28	30	600
9	15	0	29	33	0
10	15	200	30	33	200
11	15	400	31	33	400
12	15	600	32	33	600
13	20	0	33	37	0
14	20	200	34	37	200
15	20	400	35	37	400
16	20	600	36	37	600
17	23	0	37	40	0
18	23	200	38	40	200
19	23	400	39	40	400
20	23	600	40	40	600

Testing the tool started with water as the flowing fluid. Experiments were conducted according to the plan mentioned in Tables 1 and 2.

The inlet and outlet pressures were recorded as well as the forces recorded by the three load cells and back pressure was applied via the needle valve at the outlet section of the frame.

Analyzing the data showed that the 12 mm venturi performed better than the 4 mm venturi. Higher flow rates were achieved with the 12 mm venturi while the 4 mm venturi was giving high pressure drop at low flow rates and 15 USGPM was the

maximum flow rate that could pass through the venturi within the pressure capacity of the pump. Increasing flow rates beyond this flow rate would have resulted in pump shut down since the maximum operating pressure of the pump is 1000 psi.

Data analysis showed that for the 12 mm venturi, the cavitation phenomenon was initiated at 26 USGPM. Later on, it was found that the venturi works within a flow range and increasing the flow rate will not necessarily increase cavitation intensity. Therefore, the pressure pulses due to the cavitation bubbles collapse, decrease after the maximum pressure peaks are achieved. Figure 58 to 67 show the pattern of outlet pressure from 8 USGPM to 40 USGPM with no back pressure applied.

Figures 58 to 62 show the outlet pressure pattern from the minimum flow rate of 8 USGPM up to 23 USGPM. Within this range, cavitation did not occur. The fluctuations in the pressure signals are due to the triplex pump action.

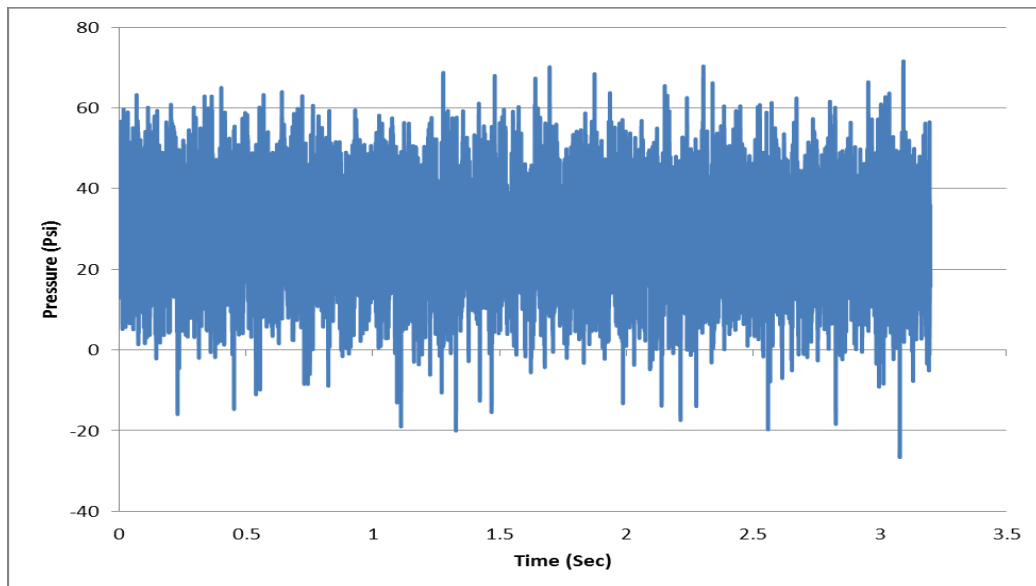


Figure 58. Outlet pressure of 12 mm venturi at 8 USGPM.

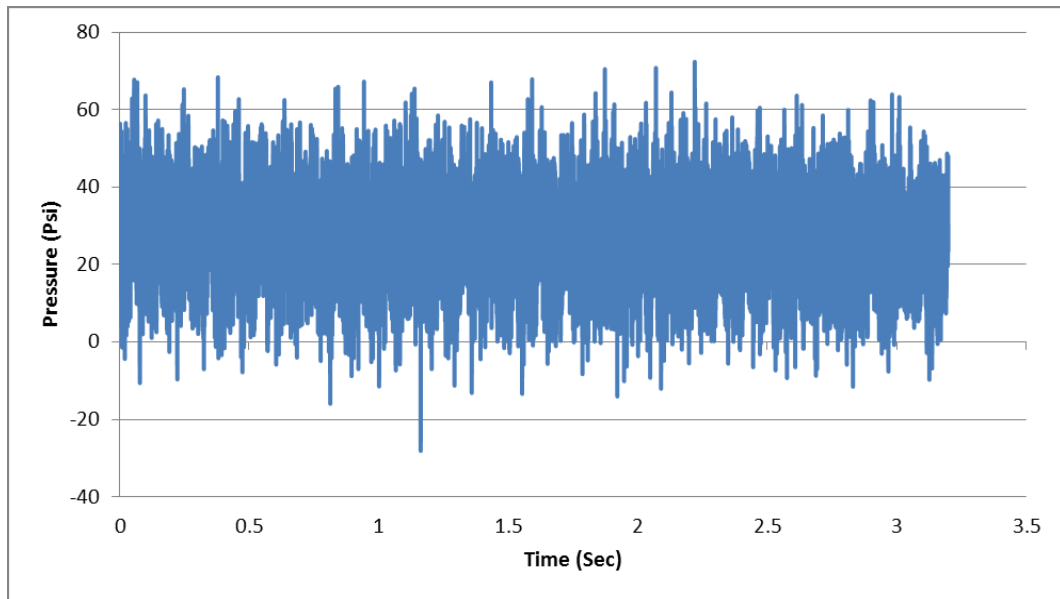


Figure 59. Outlet pressure of 12 mm venturi at 12 USGPM.

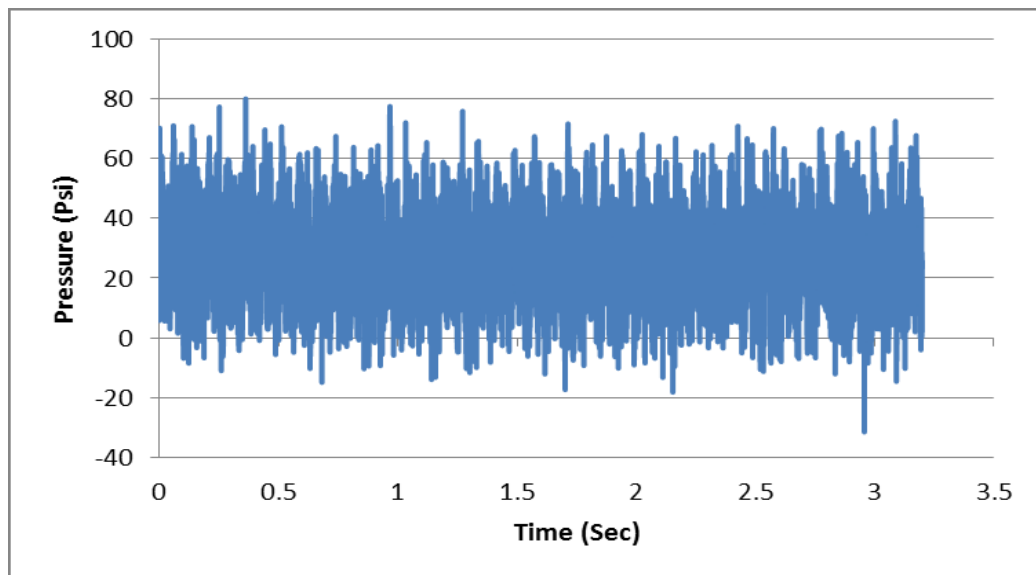


Figure 60. Outlet pressure of 12 mm venturi at 15 USGPM.

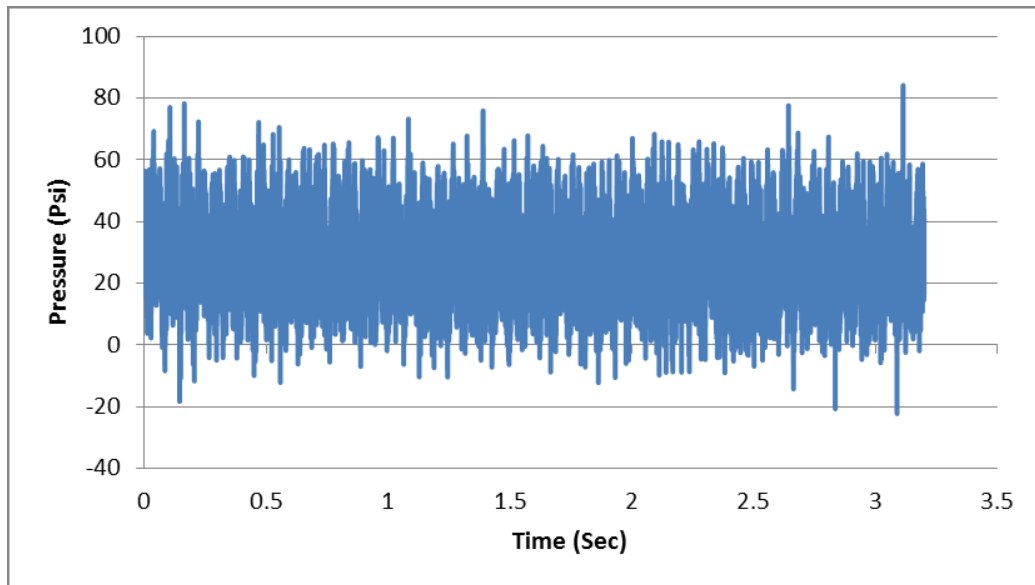


Figure 61. Outlet pressure of 12 mm venturi at 20 USGPM.

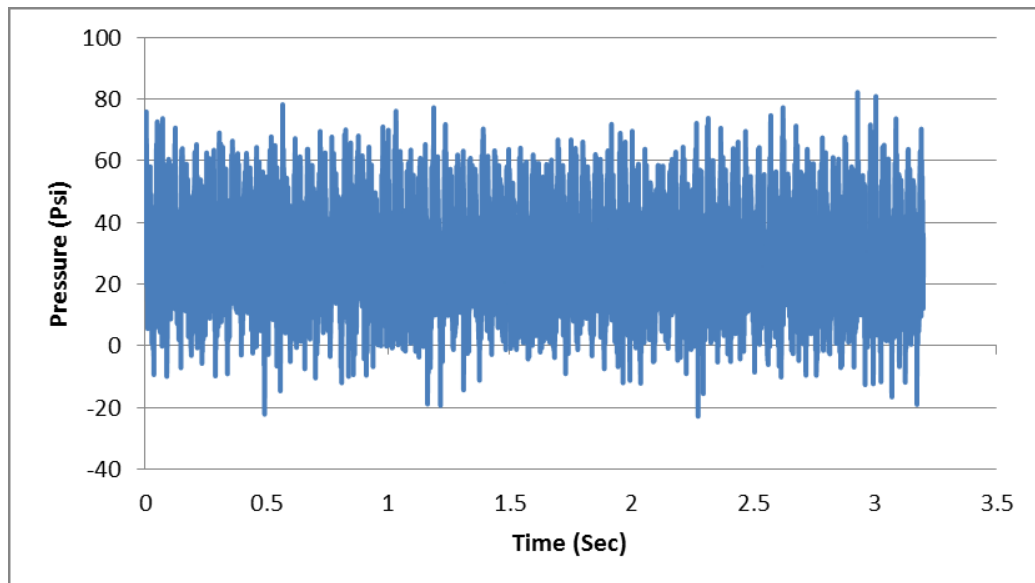


Figure 62. Outlet pressure of 12 mm venturi at 23 USGPM.

According to the Bernoulli's theorem, as the fluid velocity increases the pressure goes down. For flow rates as high as 26 USGPM, the pressure drop which is caused by fluid velocity increase, is not enough to cavitate the fluid. At 26 USGPM, the fluid velocity increase equals to the pressure drop which is needed to initiate the cavitation phenomenon and small bubbles are created at the venturi. These bubbles which move in small groups as bubble clusters are moved along the assembly. When they are introduced to the high compressive pressure at the outlet, they start to implode and pressure peaks are produced. These pressure peaks are recorded by the pressure transducer at the outlet of the assembly. The restriction plate used as the bit analogy captures the impact force of the remaining bubble clusters which were not collapsed. Collision of these bubbles causes cavitation pitting at the restriction plate surface. Figures 63 to 67 show the pressure behavior downstream of the tool. These figures show the cavitating flow pressure pattern. The pressure peaks coming from the tool are easily distinguishable from pump noise presented at Figures 58 to 62.

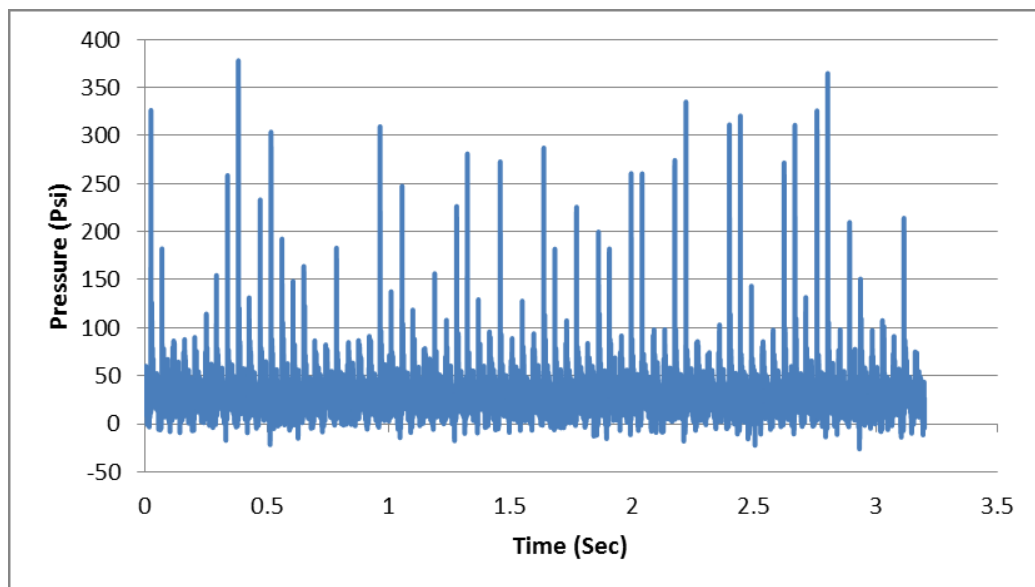


Figure 63. Outlet pressure of 12 mm venturi at 26 USGPM.

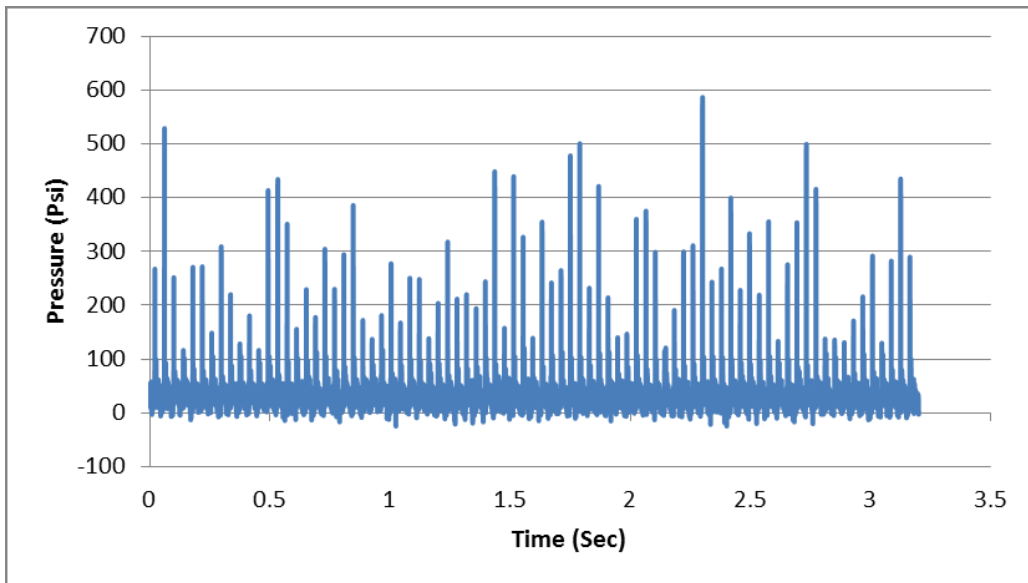


Figure 64. Outlet pressure of 12 mm venturi at 30 USGPM.

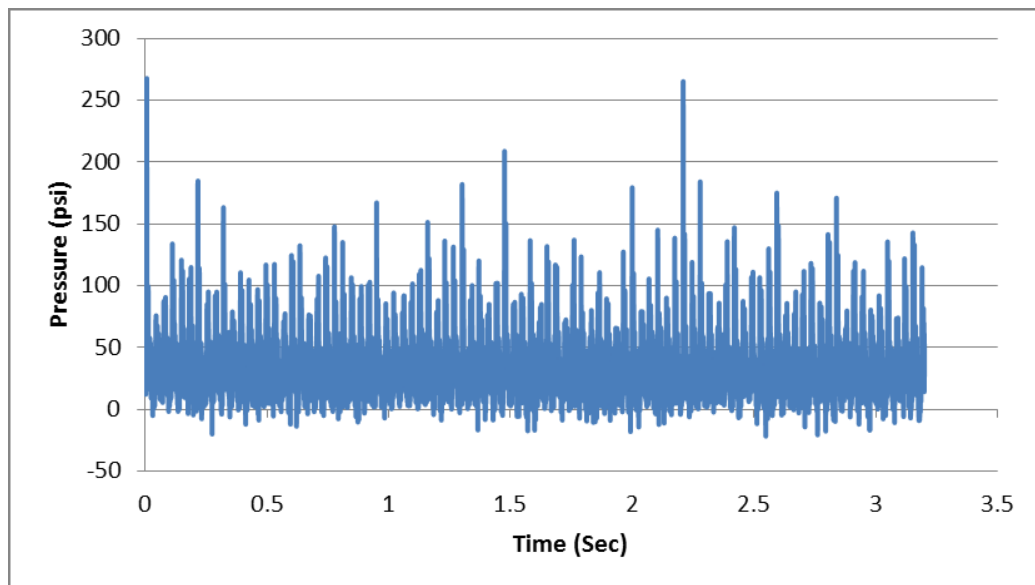


Figure 65. Outlet pressure of 12 mm venturi at 33 USGPM.

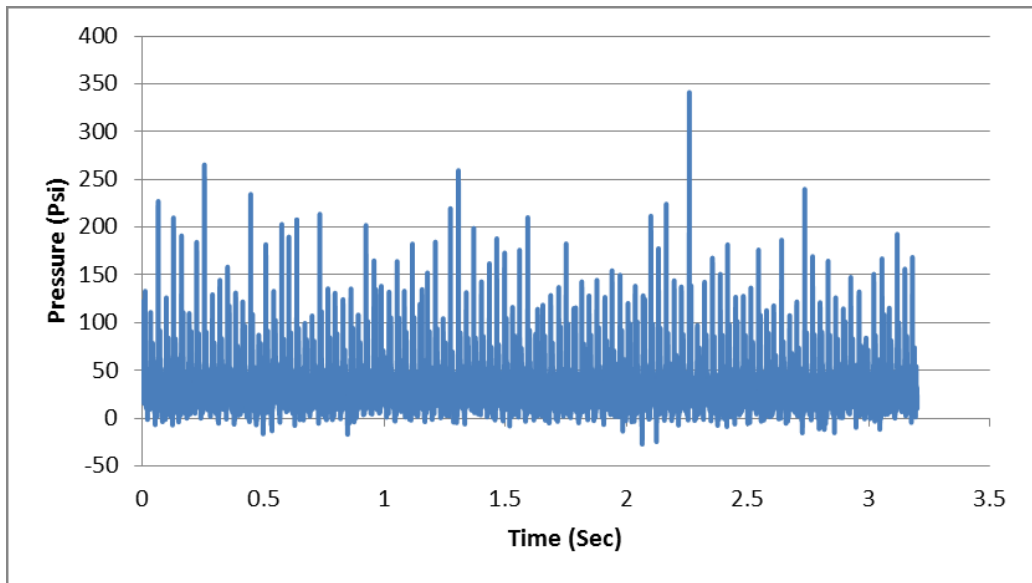


Figure 66. Outlet pressure of 12 mm venturi at 37 USGPM.

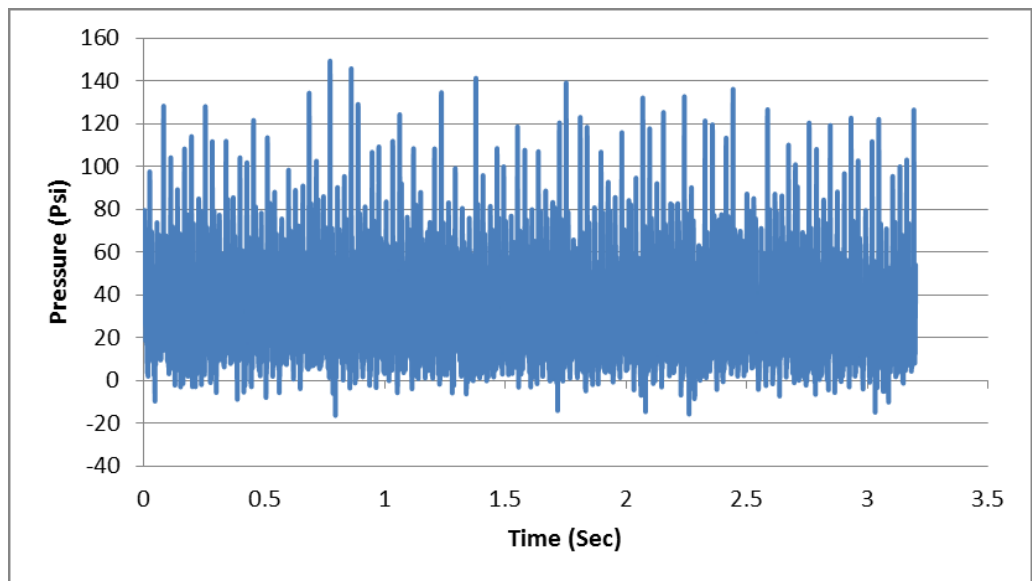


Figure 67. Outlet pressure of 12 mm venturi at 40 USGPM.

For these experiments the cavitation phenomenon started at 26 USGPM. Since by increasing the flow rate, the inlet pressure of the system also increases, therefore, there is a range for the tool to be at its optimum performance.

Experimental results show that at a flow rate of 30 USGPM, maximum pressure peaks of about 500 psi were recorded. Figure 68 is the 3D comparative plot of the working range for the 12 mm venturi. At a flow rate of about 37 USGPM pressure peaks are starting to decrease and at 40 USGPM the pressure peaks are at their lowest value of about 150 psi. Comparing the outlet pressure patterns observed when the tool is in cavitation production range with the lower flow rates show that the pressure peaks generated by the tool are much higher than the fluctuation observed due to the pump effect.

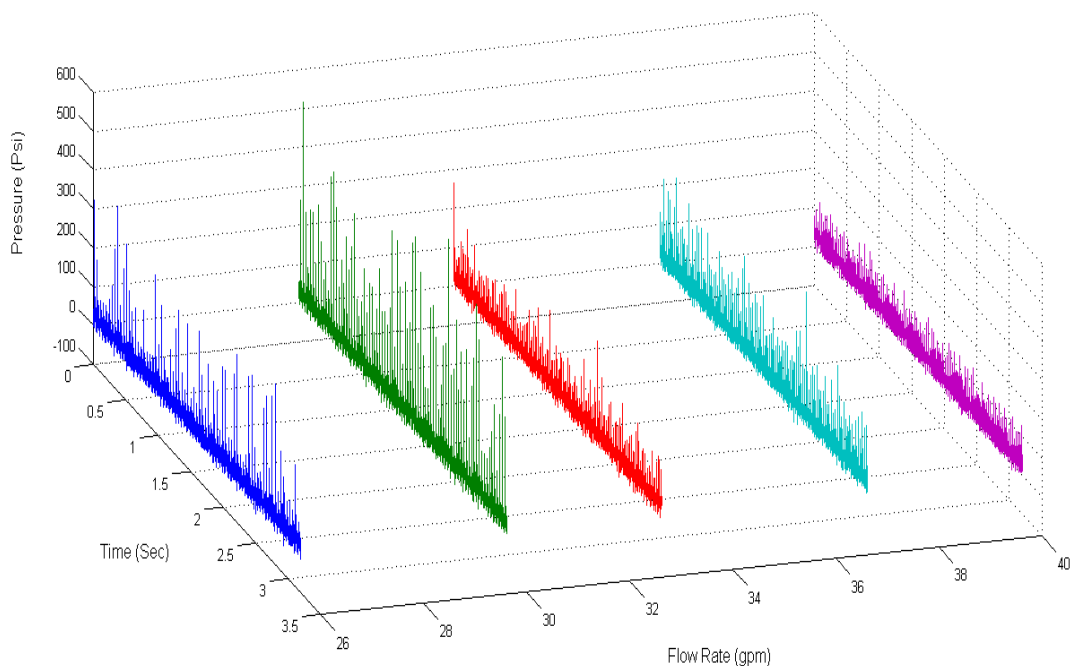


Figure 68. Comparison of pressure pulses amplitude at different flow rates during cavitation.

Figure 69 compares the pressure pattern of the outlet section of the assembly at 20 USGPM and 30 USGPM.

Back pressure was also applied through a needle valve as means of applying back pressure to simulate the situation in which the tool is operating down hole at greater depth. The tool performance and the pressure pulses produced were significantly decreased. The outlet pressure fluctuations were drastically reduced due to the fact that the needle valve was blocking the flow passage much more than the restriction applied to the flow by venturi.

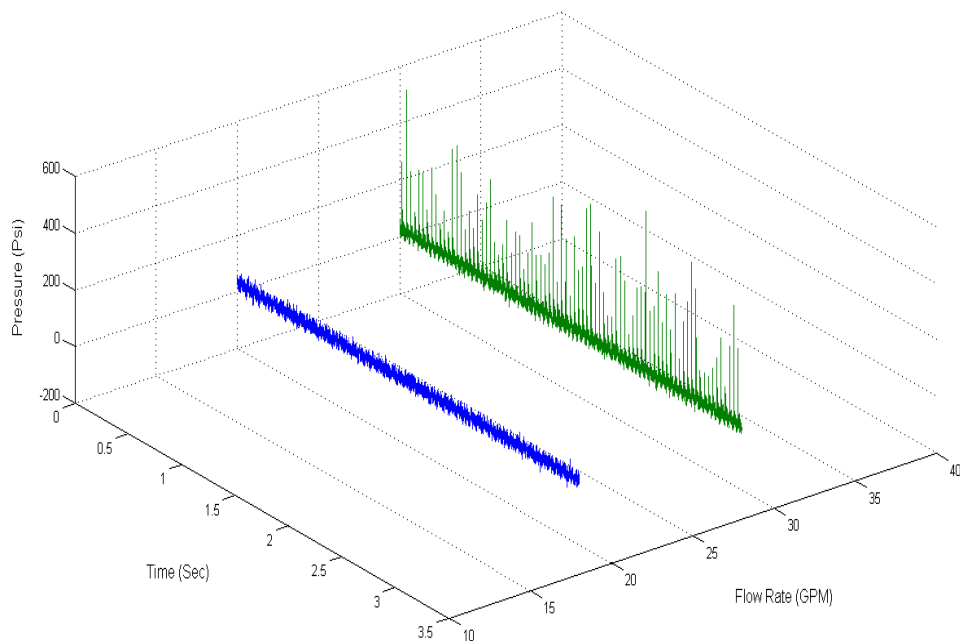


Figure 69. Comparison of outlet pressure with and without cavitation.

Figure 70 shows the outlet pressure recordings for 30 USGPM flow rate with 200 psi back pressure applied. Figure 71 compares the results for 30 USGPM flow rate with and without back Pressure.

Analyzing the data for the 4 mm venturi with water showed that although cavitation was occurring during the experiments, the amplitude of pressure peaks in comparison to the output of the 12 mm venturi was negligible. Regarding the restriction of pump operating pressure and the back pressure produced by flow of the fluid through a small diameter venturi, the inlet pressure of the venturi was significantly higher than the pressure drop of the fluid due to the venturi and intensity of the cavitation was very low.

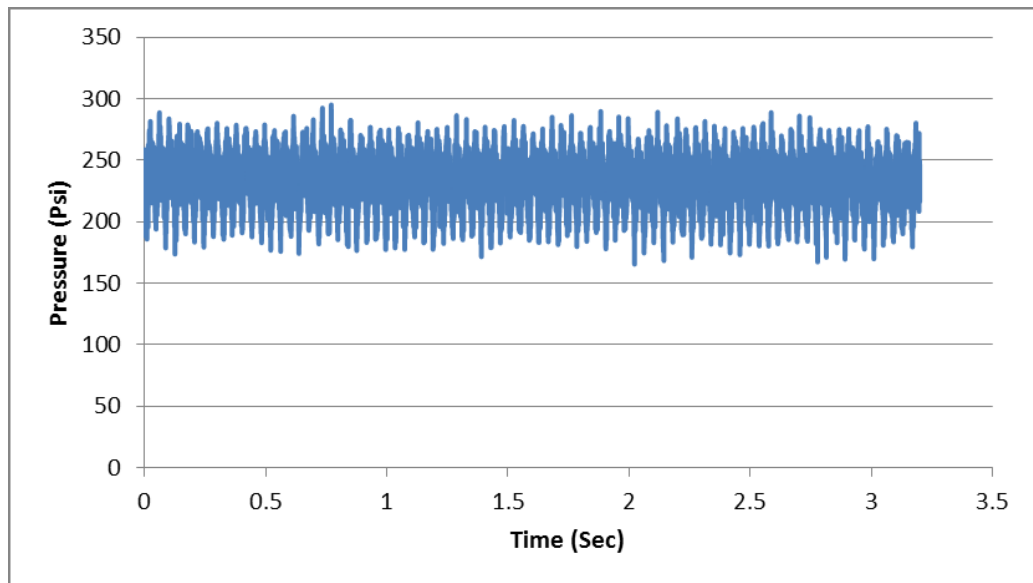


Figure 70. Outlet pressure of 12 mm venturi at 30 USGPM with 200 psi back pressure.

At a lower flow rate of 6.5 USGPM the outlet pressure peaks of 4 mm venturi was at its highest but still was not significant. This could be explained by the fact that cavitation intensity significantly depends on fluid velocity and the other factor is that

the size of bubbles produced from the 4 mm venturi were smaller than from the 12 mm venturi and pressure peaks were not as high in amplitude. Figure 72 shows the outlet pressure of the 4 mm venturi at 6.5 USGPM.

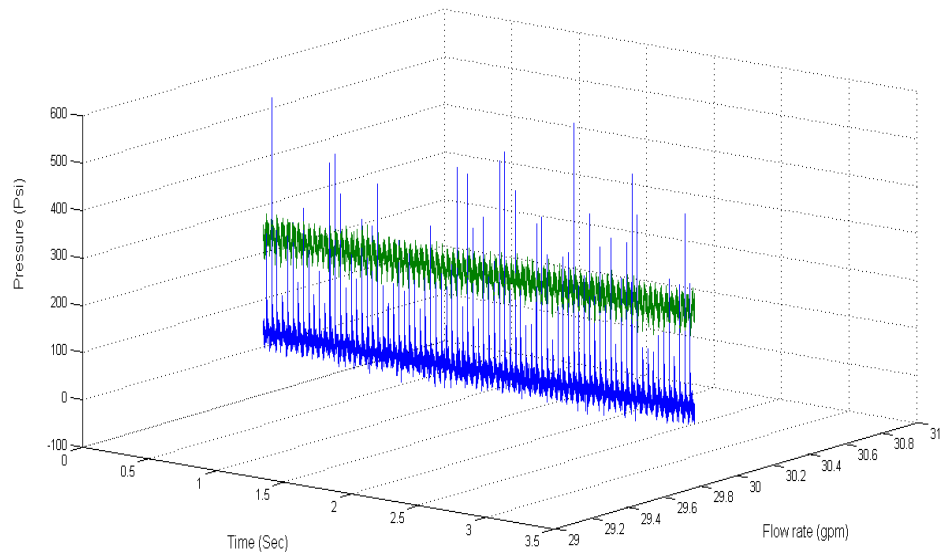


Figure 71. Comparison of outlet pressure at 30 USGPM without back pressure and with back pressure.

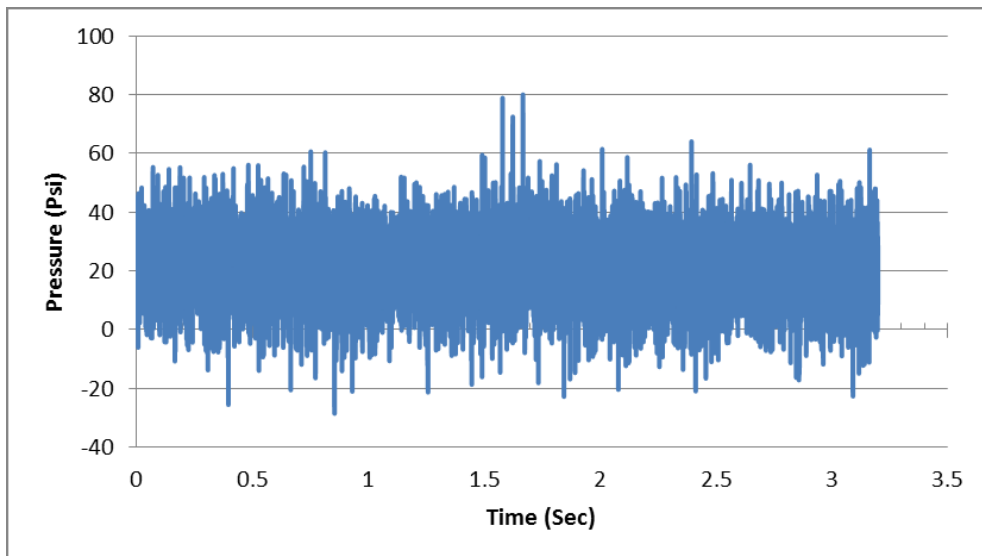


Figure 72. Outlet pressure of 4 mm venturi at 6.5 USGPM.

Another set of experiments was done to study the 12 mm pulse cavitation tool with higher flow rates. A pump truck with a duplex pump was used. The pump capacity was up to 70 USGPM. A set of experiments were done with high flow rates from 40 USGPM to 70 USGPM.

Analysis of the data also showed that the venturi produces high amplitude pressure pulses of about 250 psi. Figures 73 and 74 show the outlet pressure recordings for 50 USGPM and 60 USGPM respectively.

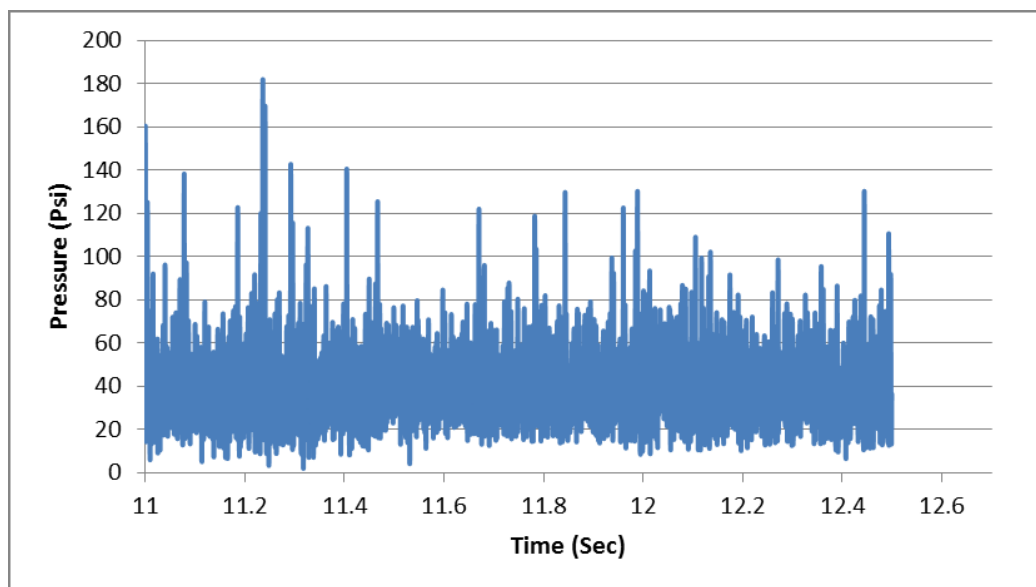


Figure 73. Outlet pressure of 12 mm venturi at 50 USGPM.

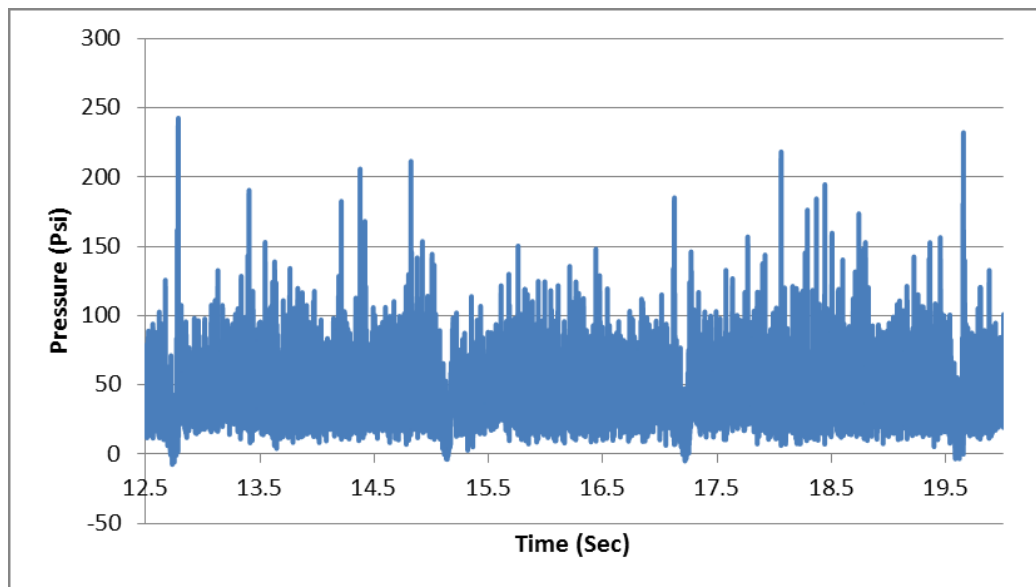


Figure 74. Outlet pressure of 12 mm venturi at 60 USGPM.

An additional set of experiments are done using the tool assembly without the venturi to study if there were any source for the pressure pulses such as the restrictor plate or pump itself. Figures 75 and 76 show the pressure outlet of the tool without the venturi at the same flow rates of 50 USGPM and 60 USGPM.

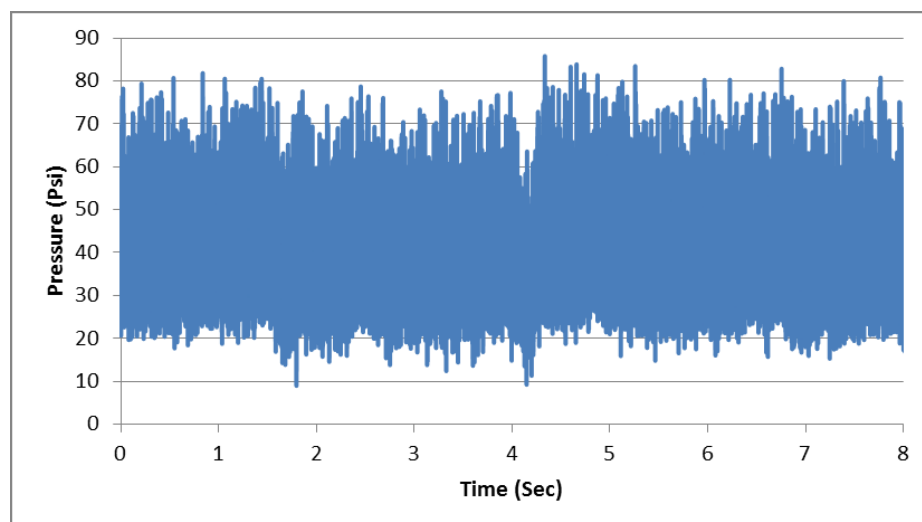


Figure 75. Outlet pressure of tool with no venturi at 50 USGPM.

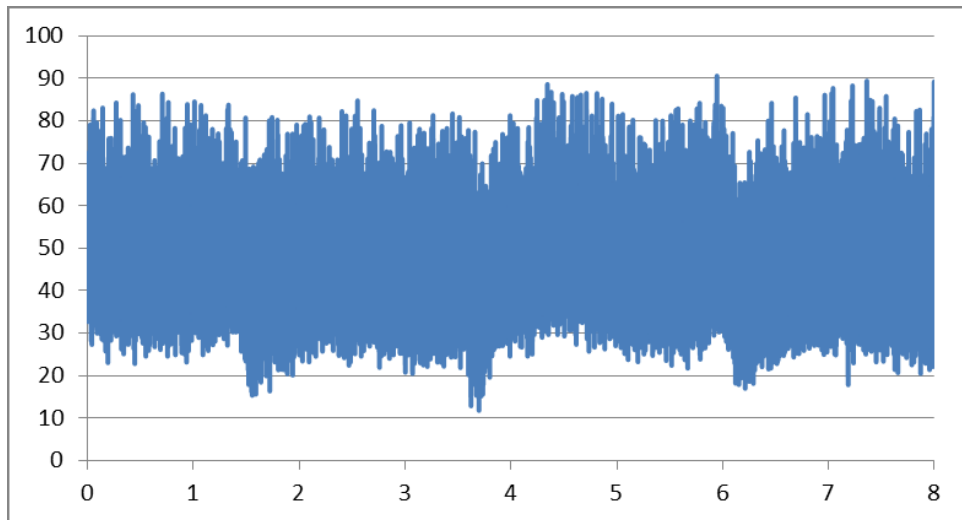


Figure 76. Outlet pressure of tool with no venturi at 60 USGPM.

Force analysis of the data agrees with the calculations based on fluid dynamics. To calculate the force generated by the action of a jet on a flat plate, the fluid density, jet area and jet velocity are required [29]. Figure 77 shows a jet impact on a plate.

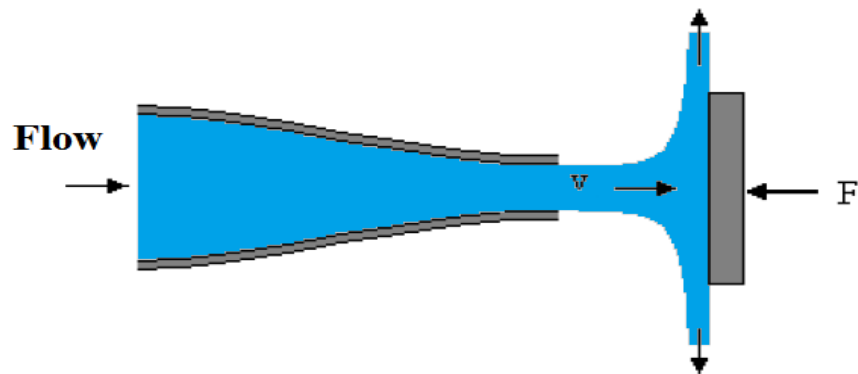


Figure 77. Schematics of a nozzle flow acting on a plate [29].

$$F = \rho (A_{\text{nozzle}}) v^2 \quad (18)$$

$$V = (60 \text{ USGPM}) (6.30902\text{e-}005 ((\text{m}^3/\text{s})/ \text{USGPM})) (3.14 \cdot 0.012^2 \text{ m}^2) = 33.47 \text{ m/s}$$

$$F = (1000 \text{ kg/m}^3) (3.14 (0.012)^2) (33.47)^2 = 506.53 \text{ N} = 113.87 \text{ lb.}$$

Studying the results of the three load cells separately and then adding their fluctuation amplitude, shows that these values are in agreement. Figures 78, 79 and 80 show the load cell data for 60 USGPM flow rate.

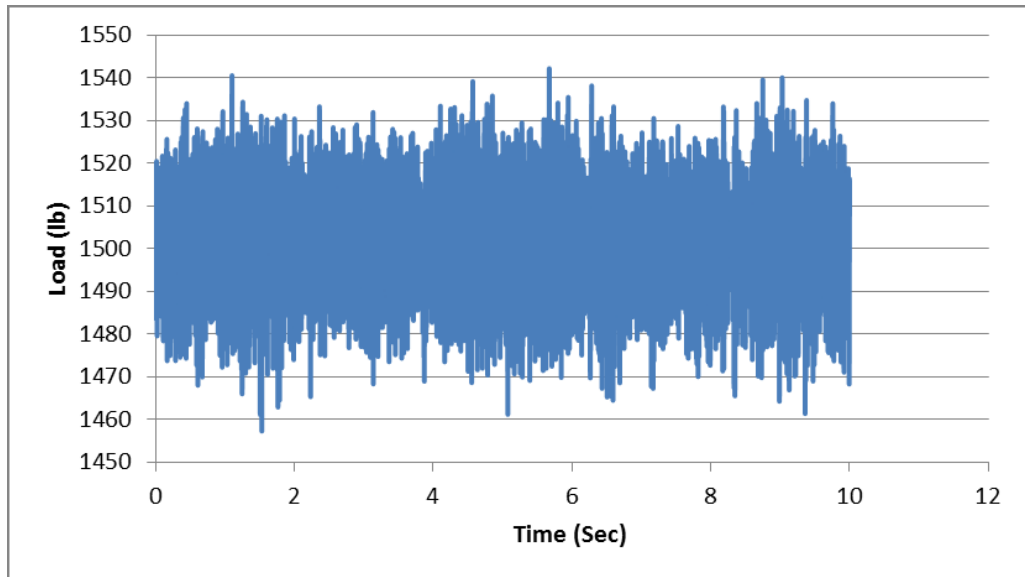


Figure 78. Load cell 1 data of 12 mm venturi at 60 USGPM.

We should keep in mind that the load cells were preloaded and the initial load was 1513 lb. According to the load data from the Figure 78 for load cell 1, the max load peak was 42.75 lb. For load cell 2 and load cell 3 from the Figures 79 and 80, the max peaks were 27.85 and 31.75 respectively. Adding these values gives:

$$\text{Load}_{\text{total}} = \text{load cell 1} + \text{load cell 2} + \text{load cell 3} \quad (19)$$

$$= 42.75 + 31.75 + 27.85 = 102.35 \text{ lb.}$$

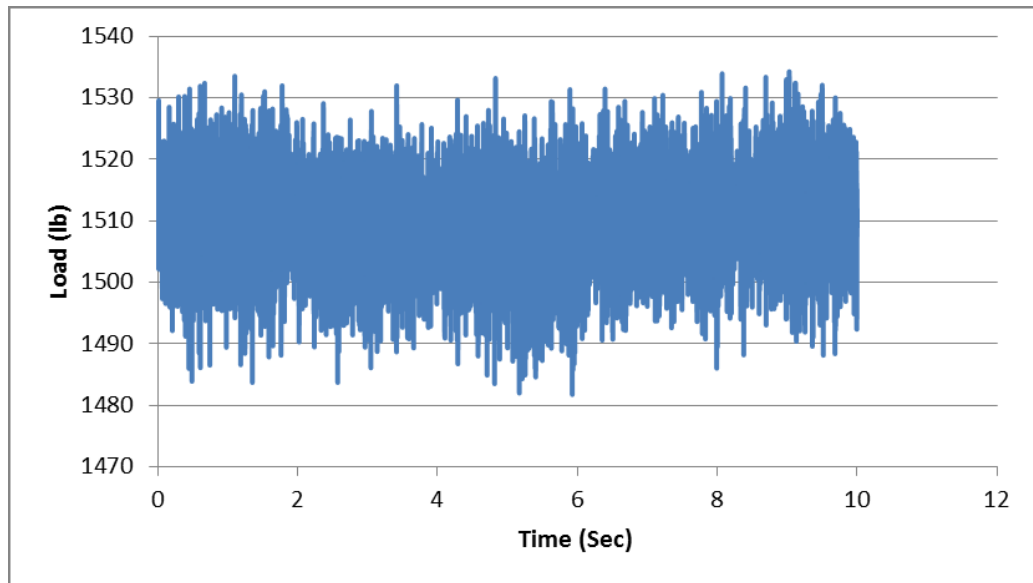


Figure 79. Load cell 2 data of 12 mm venturi at 60 USGPM.

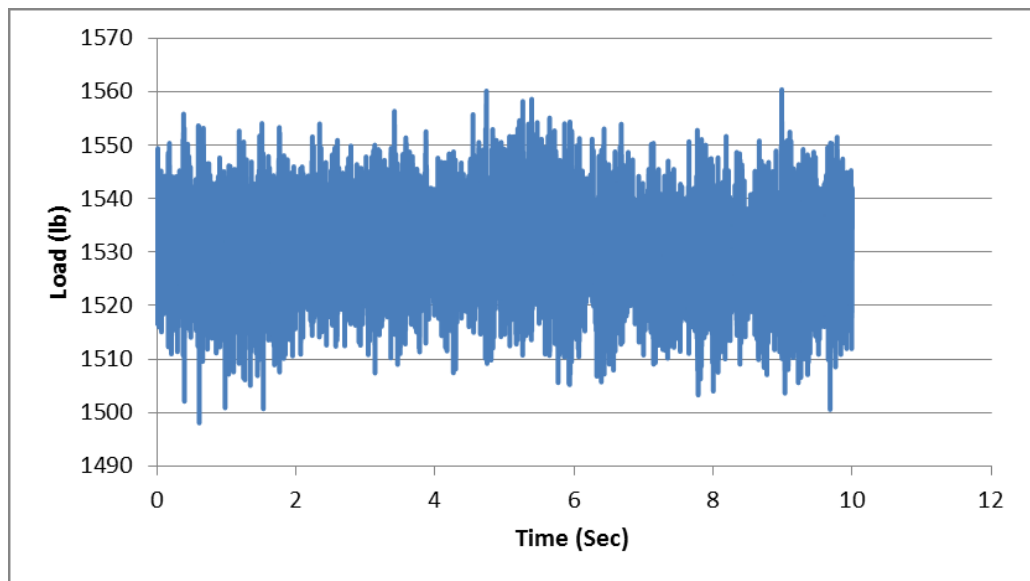


Figure 80. Load cell 3 data of 12 mm venturi at 60 USGPM.

4.5 Cavitation pitting

During the short duration of testing the 4 mm and 12 mm venturis with the restriction plate acting as a surface for the bubbles collapse, the surface of the restriction plate was eroded. This erosion due to cavitation is referred to as cavitation pitting which results from repeated collapses of the bubbles on the plate surface [30]. Figure 81 shows the different spots of the cavitation bubbles attack on the restrictor plate. Examining the surface of the plate with the naked eye does not show significant erosion due to the short duration of the exposure of the plate to the cavitating flow. However, the microscopic view of one of the spots reveals the depth of eroded zone with respect to the non-eroded area.

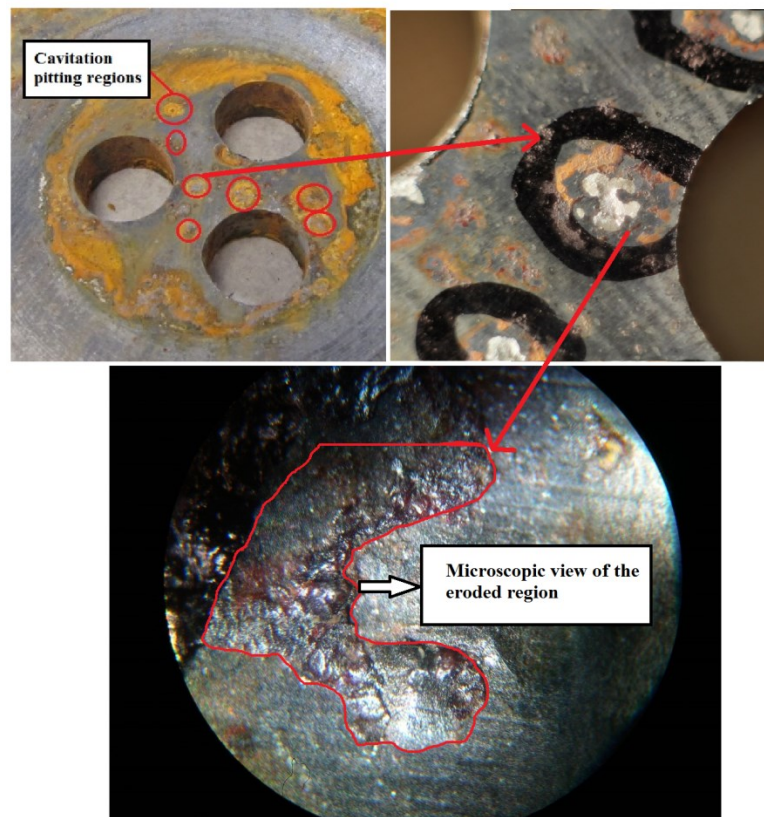


Figure 81. Different views of the eroded regions of the restrictor plate.

5. Drilling Experiments

In this chapter, drilling experiments and different factors affecting the ROP and MSE will be discussed. An 8 mm venturi insert in the drill pipe and a normal drill pipe with no venturi were used as the drill string connecting the swivel to the bit. Also, a compliant element was mounted on the drill rig to study the effects of the axial compliance in drilling performance of the normal drill pipe and the drill pipe with venturi insert.

5.1 Experimental setup description

The setup used for drilling synthetic rock specimen was the modified small scale drilling simulator or SSDS-I developed in the ADG. Figure 82 shows the different sections of this setup.

The drilling motor is mounted on top of the drill rig. This motor can operate at 300 and 600 RPM. As the motor starts, the shaft starts to rotate and the shaft rotation consequently rotates the drill pipe and the bit.

The drill motor is connected to the swivel. Rotation of the drill pipe is provided by the drill motor rotation. Drilling fluid is pumped from the triplex pump through various hoses to the swivel and then to the pipe. An inlet pressure transducer is placed just before the fluid enters the swivel.

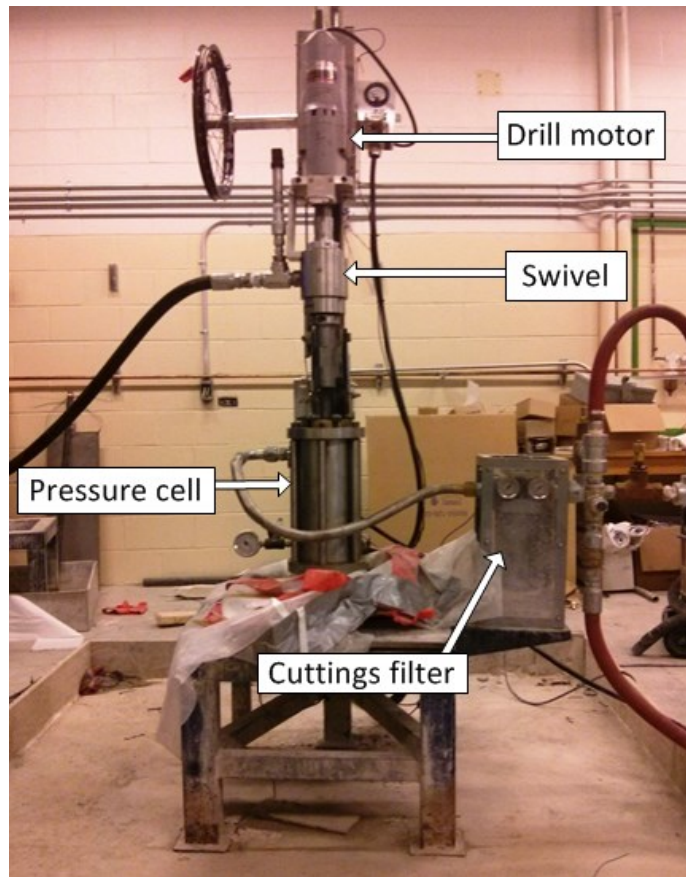


Figure 82. SSDS-I Drill rig components.

Synthetic rock samples were placed inside the pressure cell. Inside the pressure cell there are 3 metal bars to keep the rock centered and a disk holds the rock in place. Figure 83 shows the rock sample placed inside the pressure cell [31].



Figure 83. Inside view of the pressure cell with synthetic rock sample secured with rock holding disk [31].

In these experiments a 2-cutter PDC bit with outer diameter of 1.375 inch was used. Figure 84 shows a close-up view of the bit with the nozzles configuration.

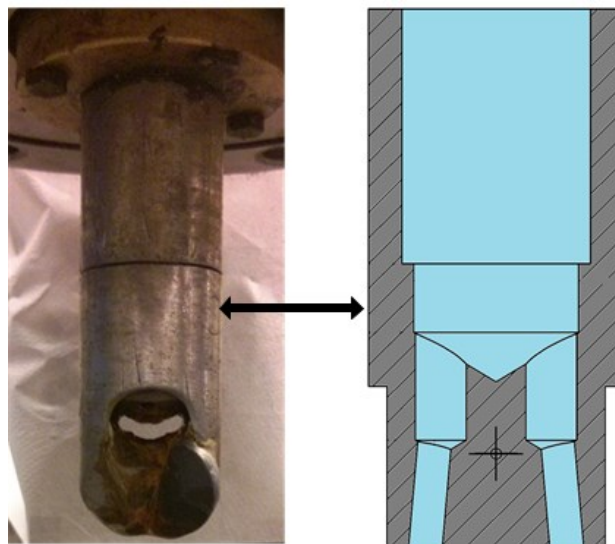


Figure 84. 2-cutter PDC bit & nozzle schematics [31].

In order to measure the movement of the bit and hence to measure the rate of penetration of the drill bit, an LVDT was mounted on the frame that moves simultaneously as the bit moves. As shown in Figure 85, when the suspended weight which applies the WOB is released, the drill pipe and the bit move downward. Since the base of the drill motor is in contact with the top part of the LVDT, the sensor starts moving and the data is collected by the DAQ system.



Figure 85. Location of LVDT measuring bit travel and suspended weight.

The last part of the drill rig is the cuttings filtration system. As the bit cuts through the rock, fine cuttings are produced. The high velocity jets of the drill bit flush away these cuttings. Drill cuttings are moved out of the pressure cell along with the drilling fluid and are filtered. Figure 86 shows the filter and filter housing for the fine debris.



Figure 86. Drill cuttings filter [31].

5.2 Compliance

The most important modification of the SSDS-I was mounting the compliant plate assembly. This modification was done regarding the further analysis of the effect of vibrations in enhancing drilling performance. The recent research done by one of the ADG members shows the positive effects of using a compliant element [32]. The compliant element converts the force vibrations into displacement and also improves the transfer of vibrations from the vibration source to the drill bit and hence increases the penetration rate. After confirming this idea with simulations done with PFC2D software, a compliant element was designed to be mounted on the SSDS-I drill rig. The design consists of two metal plates, with one acting as the base plate and the other one attached to the bottom of the pressure cell. The plates have a series of holes in a circular configuration so that any combination for the rubber mounts such as triangular or rectangular pattern is possible. Figure 87 shows the compliant section for the drill rig.

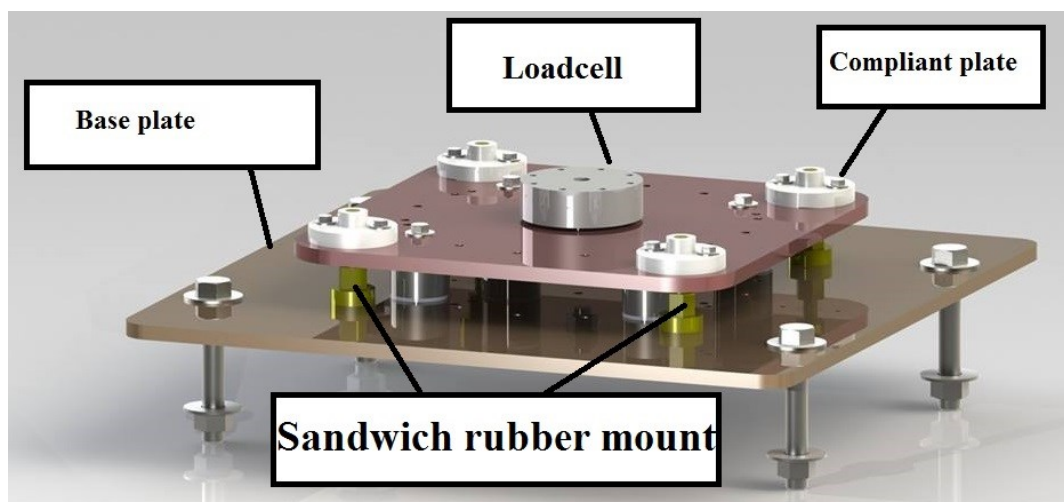


Figure 87. Different sections of the compliant element for SSDS-I setup.

5.3 Experiments Procedure

The experiments were planned in order to study the sensitivity of the drilling operation to the effects of the pulse cavitation tool and the compliant element. In order to see the performance of the pulse cavitation, two different sets of experiments were done. The first set was done with the normal drill pipe, and the second set was done with a drill pipe with venturi insert. Also, to study the effects of compliance two sets of experiments were performed. In the first set, an equilateral triangle configuration with each rubber mount located at the vertices of the triangle was used. In the second set, three metal mounts which would not allow any axial movement of the upper plate and hence no compliance was used.

The experiments started with placing the rock samples inside the pressure cell and fixing them with the rock holding disk. After securing the pressure cell, the flow rate was set. At this point, the specified WOB was applied to the bit by hanging the suspended weight from the wheel connected to the drill motor assembly. Drilling started with turning on the drill motor and let the bit cut through the rock as the suspended weight was moved downward. Meanwhile the data was recorded by the sensors and sent to the DAQ system. After the drilling procedure was finished, the system was turned off and the drilled sample was replaced with another sample and experiments continued.

Table 3 shows the experiments plan, 2 different WOBs, 7 different flow rates, 2 modes of compliance, 2 different borehole pressures and 2 different drill pipes were used.

Table 4. 8 mm venturi drilling plan

8mm venturi_No compliance				8mm venturi_compliance			
Test	Flow (GPM)	WOB (lb)	Borehole Pressure (Psi)	Test	Flow (GPM)	WOB (lb)	Borehole Pressure (Psi)
1	8	600	0	20	8	600	0
2	12	600	0	21	12	600	0
3	15	600	0	22	15	600	0
4	18.5	600	0	23	18.5	600	0
5	22.6	600	0	24	22.6	600	0
6	26	600	0	25	26	600	0
7	30	600	0	26	30	600	0
8	8	300	0	27	8	300	0
9	12	300	0	28	12	300	0
10	15	300	0	29	15	300	0
11	18.5	300	0	30	18.5	300	0
12	22.6	300	0	31	22.6	300	0
13	26	300	0	32	26	300	0
14	30	300	0	33	30	300	0
15	8	600	300	34	8	600	300
16	12	600	300	35	12	600	300
17	15	600	300	36	15	600	300
18	18.5	600	300	37	18.5	600	300
19	22.6	600	300	38	22.6	600	300

Table 3. Drill pipe drilling plan

Drill pipe_No compliance				Drill pipe_compliance			
Test	Flow (GPM)	WOB (lb)	Borehole Pressure (Psi)	Test	Flow (GPM)	WOB (lb)	Borehole Pressure (Psi)
39	8	600	0	51	8		0
40	12	600	0	52	12		0
41	15	600	0	53	15		0
42	18.5	600	0	54	18.5		0
43	22.6	600	0	55	22.6		0
44	26	600	0	56	26		0
45	30	600	0	57	30		0
46	8	600	300	58	8		300
47	12	600	300	59	12		300
48	15	600	300	60	15		300
49	18.5	600	300	61	18.5		300
50	22.6	600	300	62	22.6		300

5.4 Drilling experiments results

Penetration rate and the MSE are the key factors of a drilling process. MSE according to the literature is [33]:

$$\text{MSE} = \frac{\text{WOB}}{(\text{A_bit})} + \frac{120 \pi \text{N T}}{(\text{A_bit}) \text{ROP}} \quad (20)$$

Where:

WOB: Weight on bit, (lbs.)

A_bit: Drill bit area, (in²)

N: Bit revolutions per minute, (RPM)

T: Torque, (lb-ft)

ROP: Penetration rate, (ft/hr)

Increasing the penetration rate as discussed in the previous chapters, reduces the drilling time and hence reduces the costs. Therefore, drilling researchers are always looking for new methods and tools to improve drilling efficiency by drilling faster. ROP data comparison for both the tools used in the drilling experiments shows that including the compliant element into the system, increases ROP. Also, ROP data analysis showed that the venturi insert was not efficient and the effect of compliance was more significant. ROP data analysis shows that the drilling with the normal drill pipe with no venturi was more efficient and resulted in higher penetration rates.

On the other hand, both drill pipe and the drill pipe with venturi insert had better performance when there was compliant element present. However, when the back

pressures applied through the needle valve located after the drill cell, due to the significant resistance to the flow, drilling efficiency and penetration rate dropped drastically.

Figures 88 and 89 compares the ROP and MSE values for venturi insert with and without the compliant element.

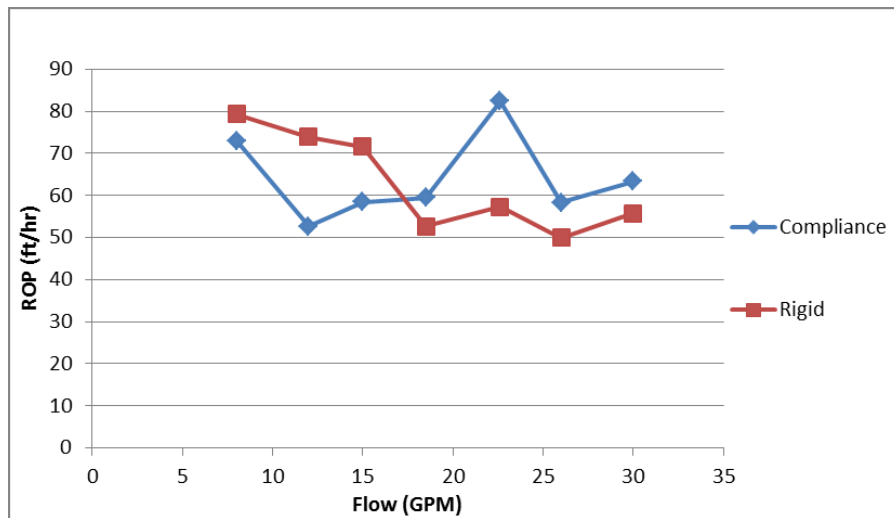


Figure 88. ROP for venturi with and without compliant element at different flow rates.

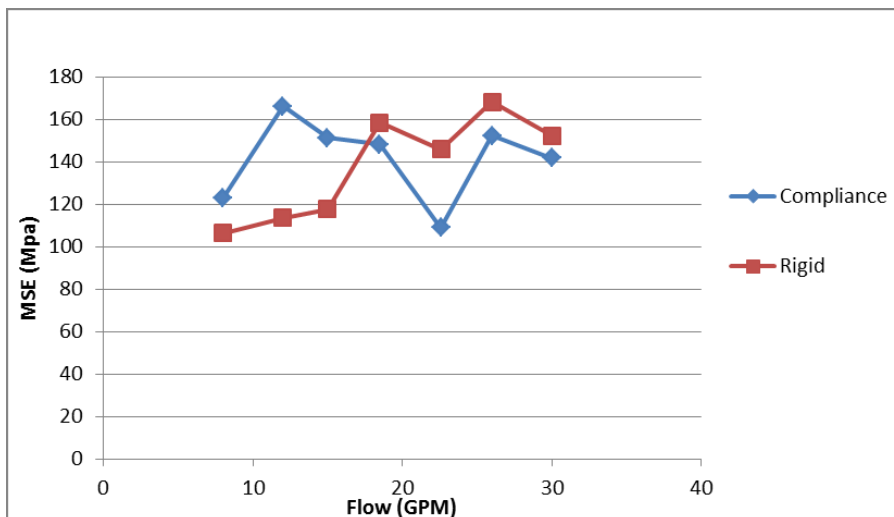


Figure 89. MSE for venturi with and without compliant element at different flow rates.

Figures 90 and 91 present the ROP and MSE values for the drill pipe with and without the compliant element at different flow rates.

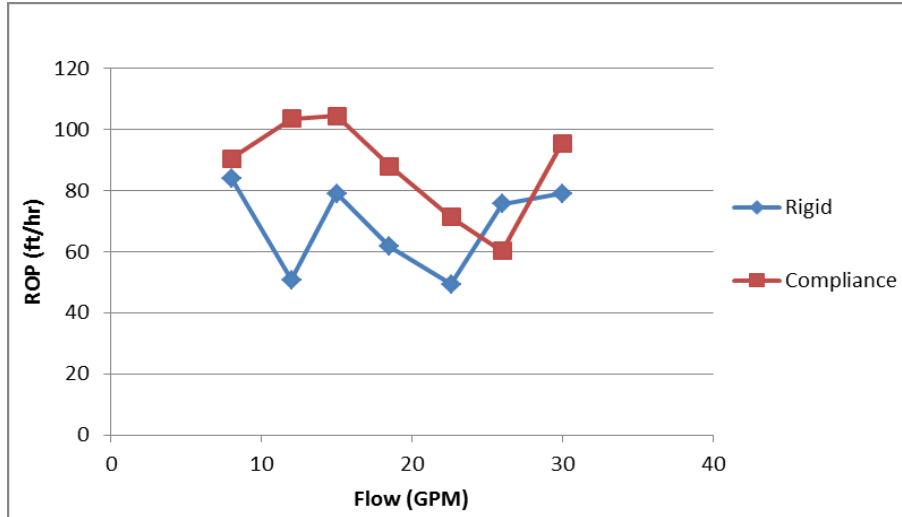


Figure 90. ROP for drill pipe with and without compliant element at different flow rates.

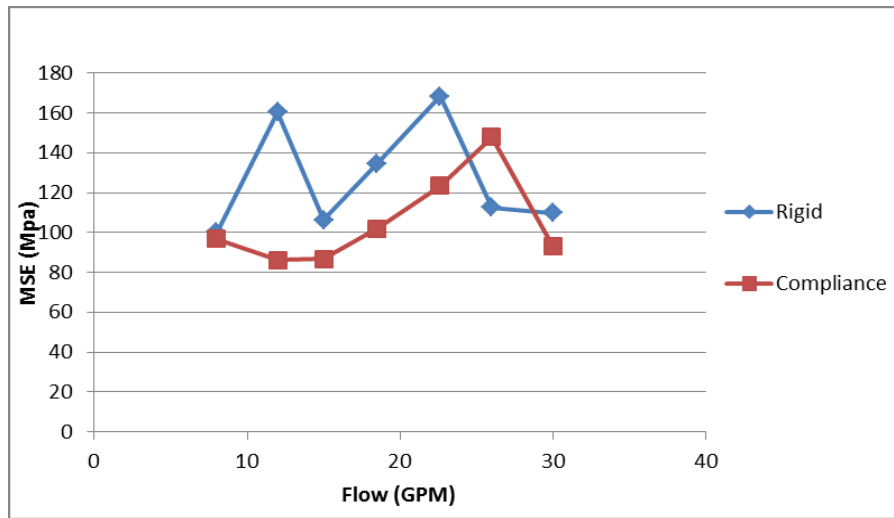


Figure 91. MSE for drill pipe with and without compliant element at different flow rates.

Comparing the results for venturi and drill pipe shows that if all the factors are the same, with applying enough WOB, drill setup performs better with compliant element.

However, when the WOB was not high enough, experiments showed that this configuration is not optimum for the compliant element to be effective. Also, applying back pressure had similar results close to the low WOB case.

The fact that low WOB results in slower drilling has been established before. The WOB does not provide enough force for the cutter to move and penetrate the rock. In this case more energy is wasted and the drilling efficiency decreases significantly.

Figures 92 and 93 present the ROP and MSE values for venturi at low WOB.

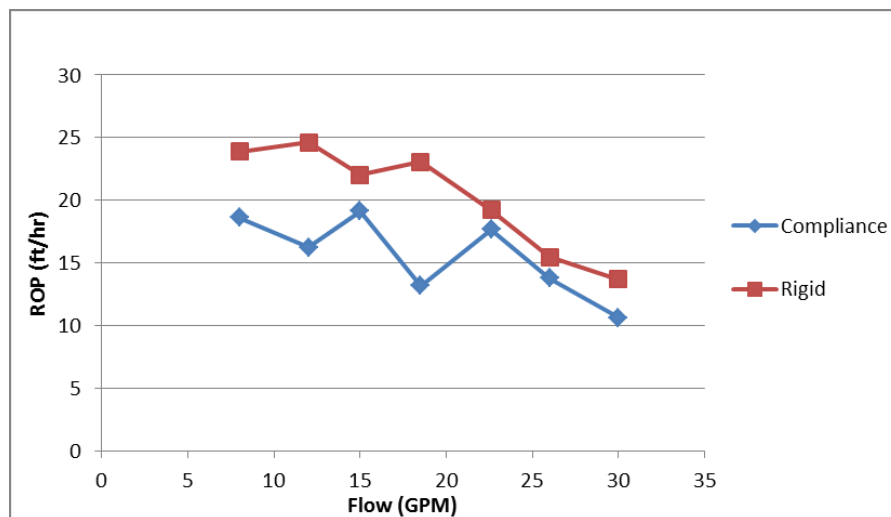


Figure 92. ROP for venturi with and without compliant element at different flow rates at low WOB.

Comparing the low WOB drilling tests with and without the compliant element shows that compliant element is efficient when WOB is high enough and this results in better conversion of force profile into displacement. Analysis of the LVDT below the

compliant plate shows that the displacement fluctuation amplitude is very low with low WOB and it is high when high WOB is applied.

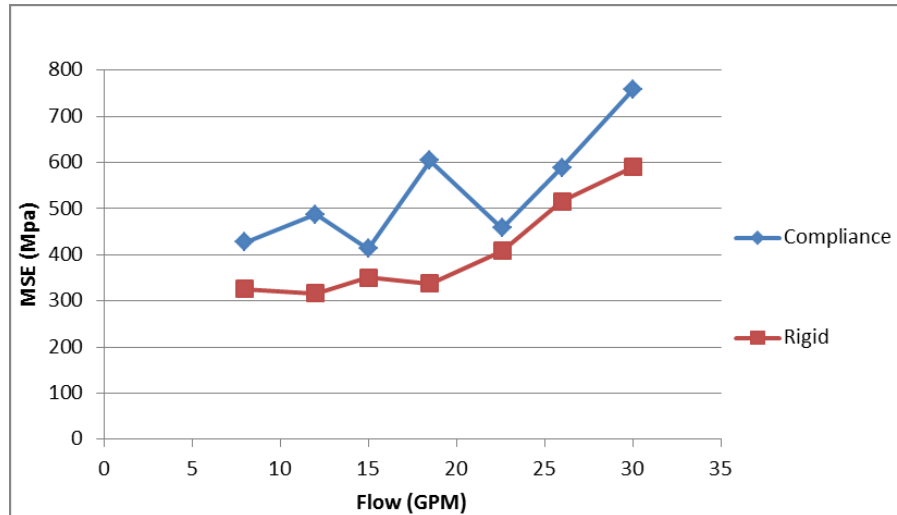


Figure 93. MSE for venturi with and without compliant element at different flow rates at low WOB.

Analysis of ROP and MSE when 300 psi back pressure was applied also shows the same negative effect when the applied WOB was low. This has resulted in lower fluctuations in displacement of the compliant element. Thus, the drilling rate was slow and efficiency of the drilling operation was very low. Comparing the results show that in both cases when the WOB was low and when high back pressure was applied, the fluctuations of the compliant plate was very low, which indicates the poor conversion of axial force into axial displacement and hence rate of penetration was slow and MSE was high.

Figures 94 and 95 present the venturi ROP and MSE at 300 psi back pressure. In both cases with and without compliance, the drilling efficiency is very low. Although

without compliance shows slightly better improvement, this is not a fair comparison since the ROP is very low and drilling efficiency is around 10%.

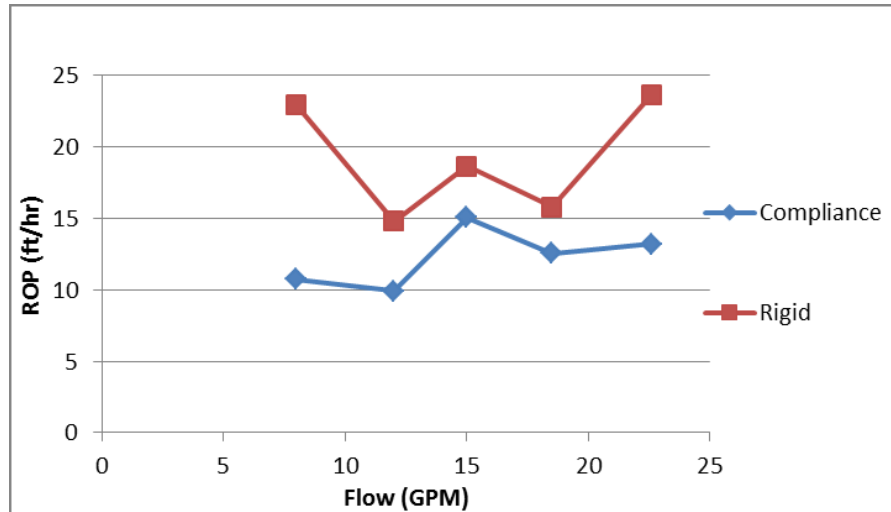


Figure 94. ROP for venturi with and without the compliant element at 300 psi back pressure.

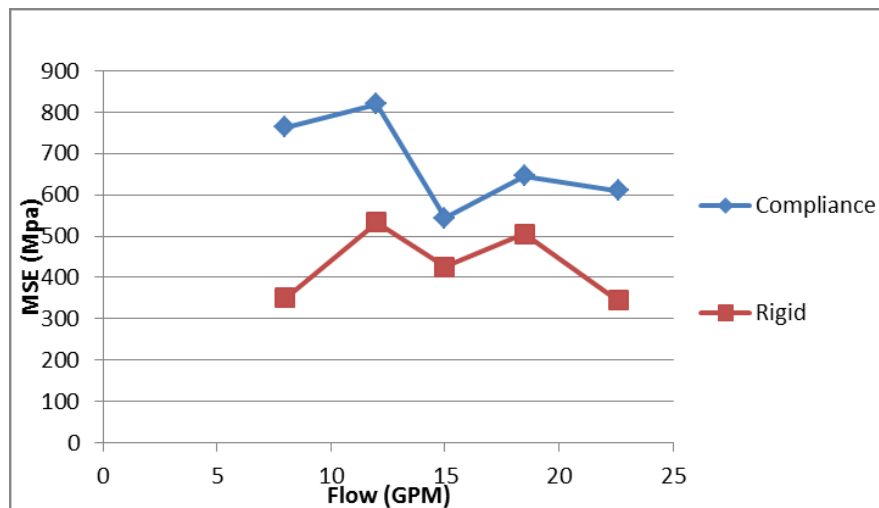


Figure 95. MSE for venturi with and without the compliant element at 300 psi back pressure.

Figures 96 and 97 show the performance of drill pipe at 300 psi at different flow rates and Figure 98 compares the ROP of drill pipe and venturi at 3 high flow rates. This

figure shows that performance of drill pipe is much better than venturi. Figure 98 shows that even with the aid of compliant element, venturi performance is very low but the drill pipe even without any compliance is working better. This comparison will be further discussed and venturi and drill pipe will be compared when both are working at their best performance with high WOB, high ROP and lower MSE values and drilling efficiencies are much higher. That comparison will be more valid since the efficiency of the drilling is much higher than 10 %.

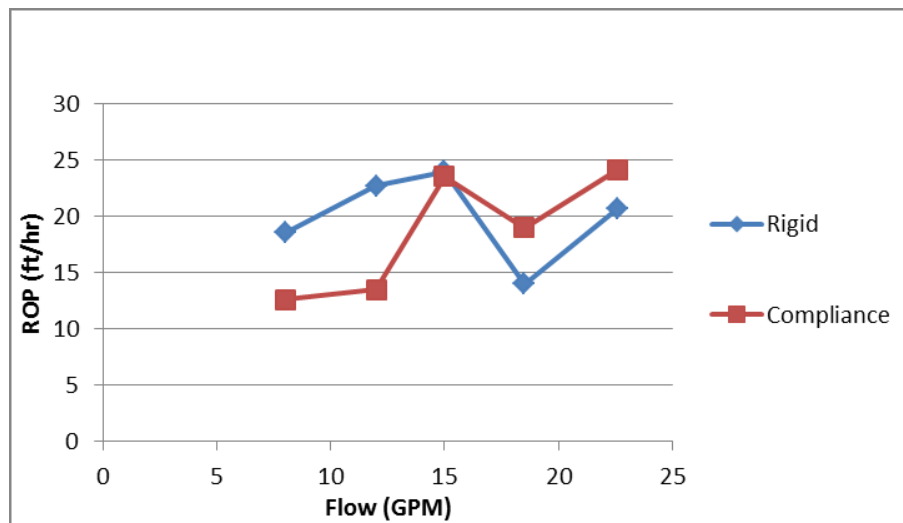


Figure 96. ROP for drill pipe with and without the compliant element at 300 psi back pressure.

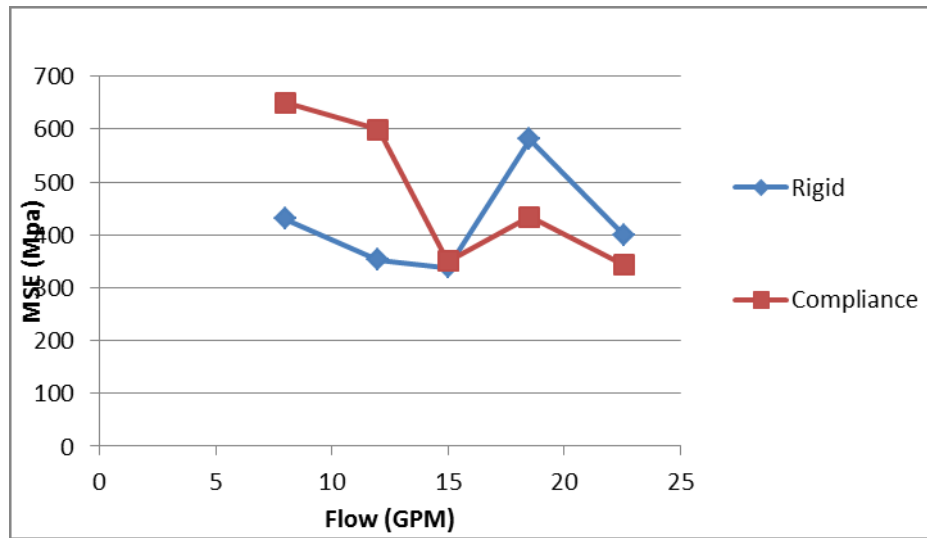


Figure 97. MSE for drill pipe with and without the compliant element at 300 psi back pressure.

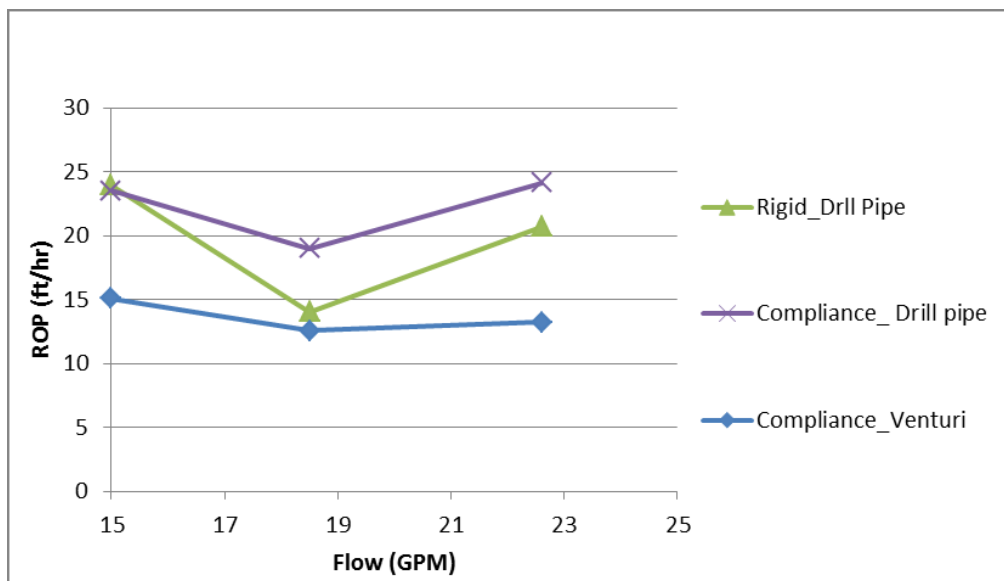


Figure 98. ROP comparison of venturi and drill pipe at 300 psi back pressure at high flow rates.

The final comparison of the drill pipe and venturi with the compliant element is presented in Figures 99 and 100.

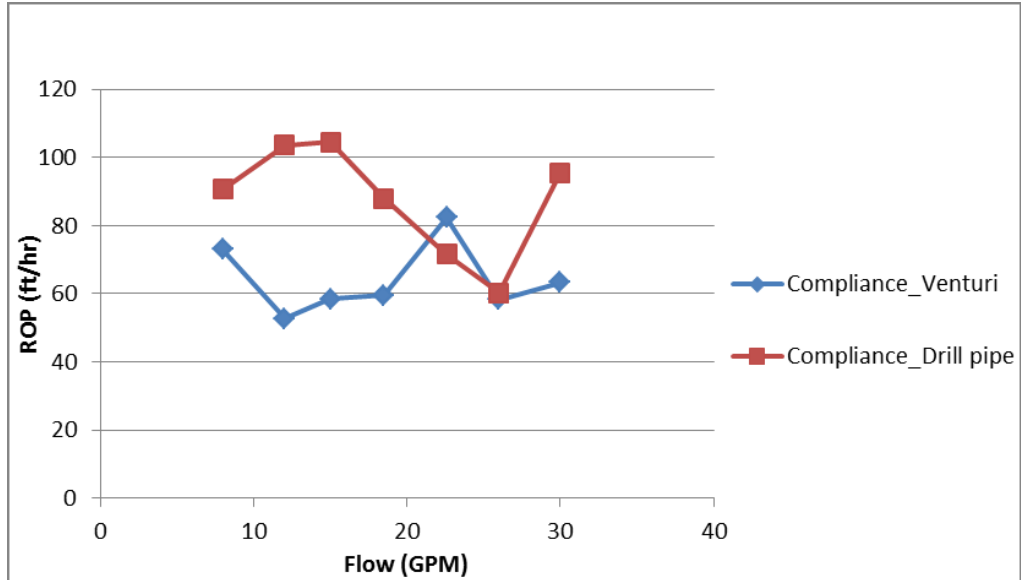


Figure 99. ROP of venturi versus drill pipe at high WOB with compliance.

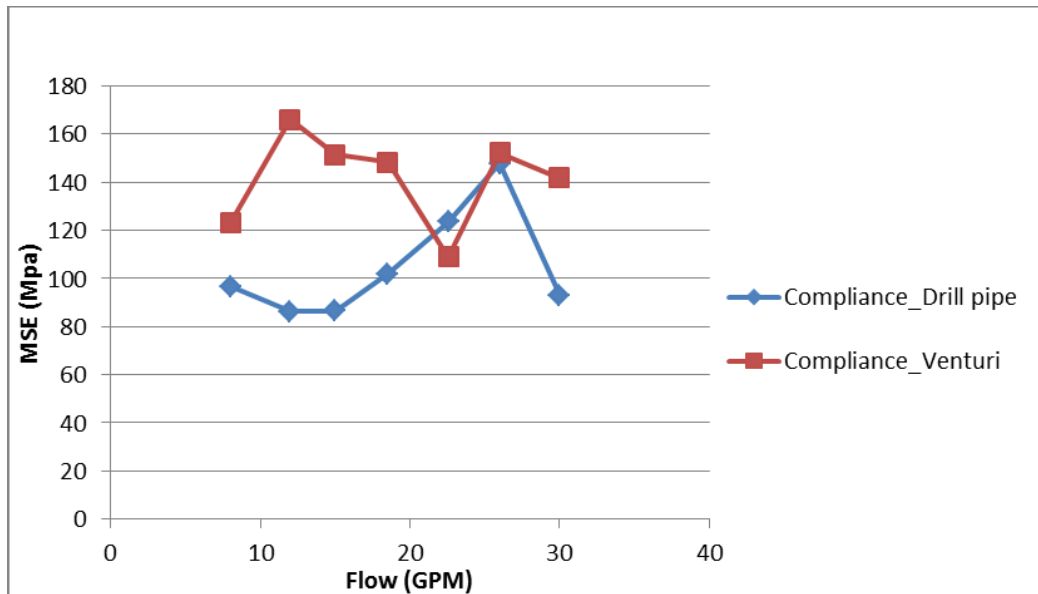


Figure 100. MSE of venturi versus drill pipe at high WOB with compliance.

Comparing the ROP and MSE values shows that inserting a venturi inside drill pipe did not improve the drilling efficiency even at higher flow rates and the drill pipe performance was better at the same conditions.

Comparing the pressure losses for the venturi insert with the drill pipe shows that the available pressure drop for the bit in the drill pipe is higher than the venturi insert.

Tables 5 and 6 show the calculation for bit pressure drop for both scenarios.

Table 5. Drill pipe bit pressure drop.

Drill pipe Bit Pressure Drop			
Q (gpm)	Bit_P (psi)	HP	HSI
8	32.44	0.15	0.10
12	72.99	0.51	0.34
15	114.04	1.00	0.67
18.5	173.47	1.87	1.26
22.6	258.88	3.41	2.30
26	342.64	5.20	3.50
30	456.17	7.98	5.38

Table 6. Venturi insert bit pressure drops.

Venturi insert Bit Pressure Drop			
Q (gpm)	Bit_P (psi)	HP	HSI
8	7.85	0.12	0.08
12	17.67	0.57	0.38
15	27.61	0.74	0.50
18.5	42.01	1.30	0.88
22.6	62.69	2.67	1.80
26	82.97	4.03	2.71
30	110.46	6.73	4.54

Figures 101,102 and 103 show the pressure drop calculation for both the drill pipe and the venturi insert. Figure 101 compares the bit pressure drop for venturi and the drill pipe. Figures 102 and 103 show the parasitic pressure drops and available pressure drop for drill bit.

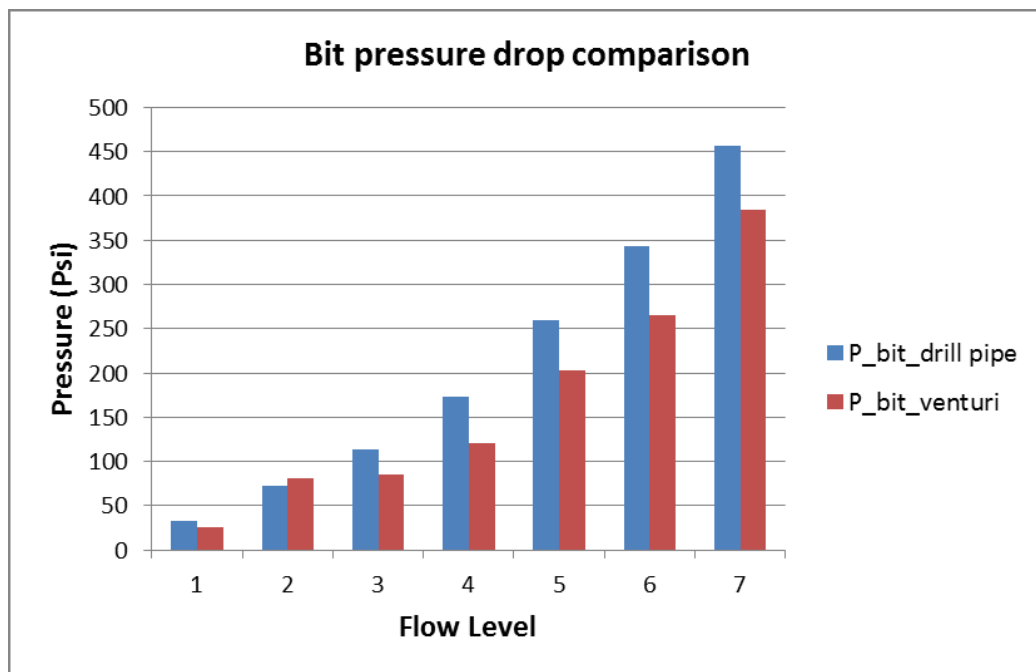


Figure 101. Bit pressure drop comparison.

Figure 101 shows that the pressure drop for the drill pipe is higher at all the flow rates and hence more energy was available for the drill bit. Since the overall pressure drop across the flow system is limited by the pressure capacity of the pump, the additional pressure across the venturi reduces the pressure drop across the bit and the corresponding bit hydraulic horsepower. This was confirmed from the corresponding pressure drop calculations, and agrees with the consistently better drilling efficiency of the smooth drill pipe configuration compared to venturi insert.

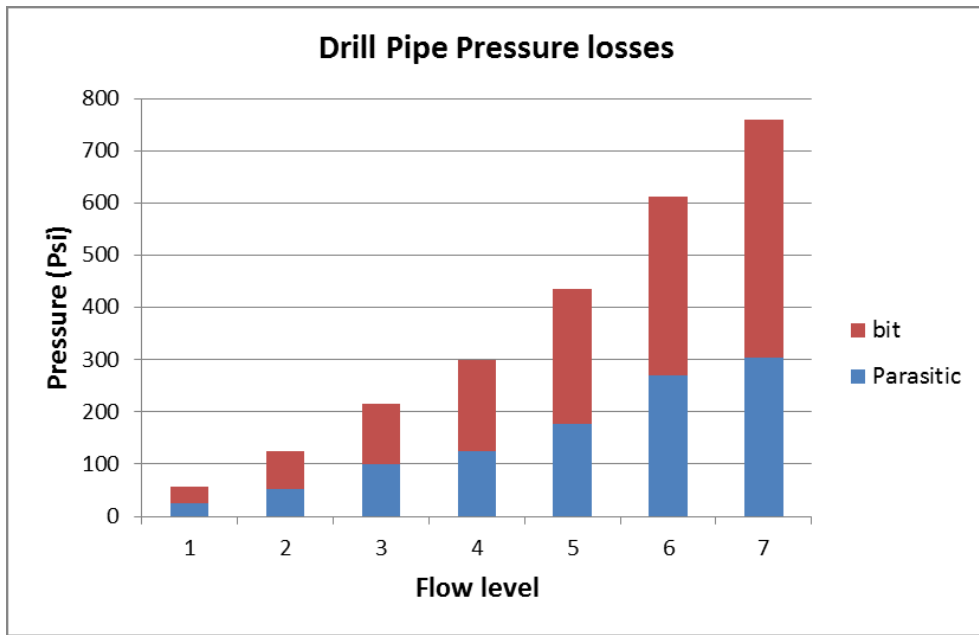


Figure 102. Drill pipe bit pressure drop and system pressure losses.

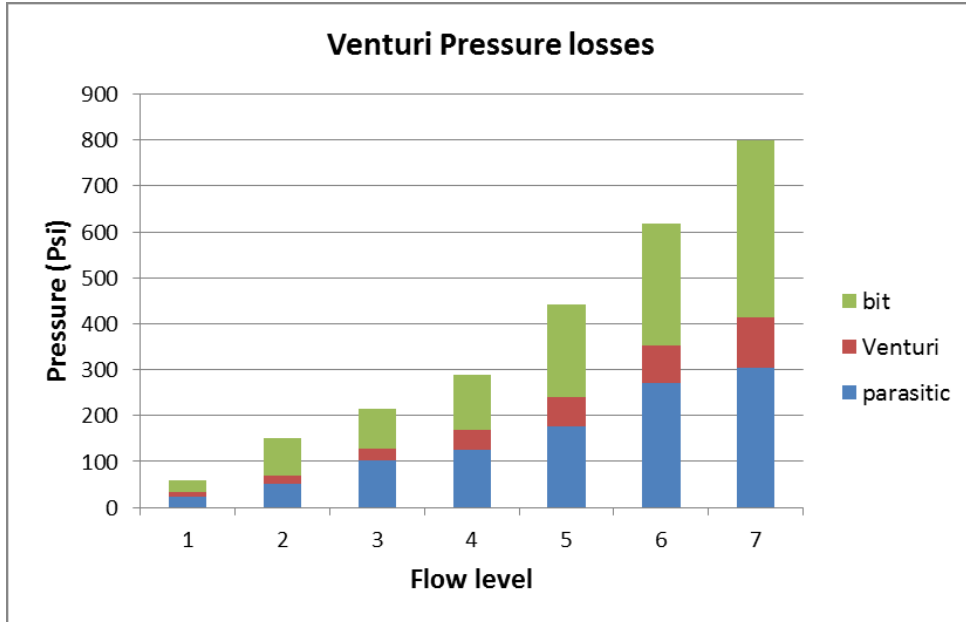


Figure 103. Venturi insert pressure drops.

Figure 104, shows the HSI versus flow rate for both the venturi insert and drill pipe.

HSI is defined as the bit hydraulic horsepower divided by bit area in square inches [2]:

$$HP_{bit} = \frac{\Delta P_{bit} * Q}{1714} \quad (21)$$

$$HSI = \frac{HP_{bit}}{A_{bit}} \quad (22)$$

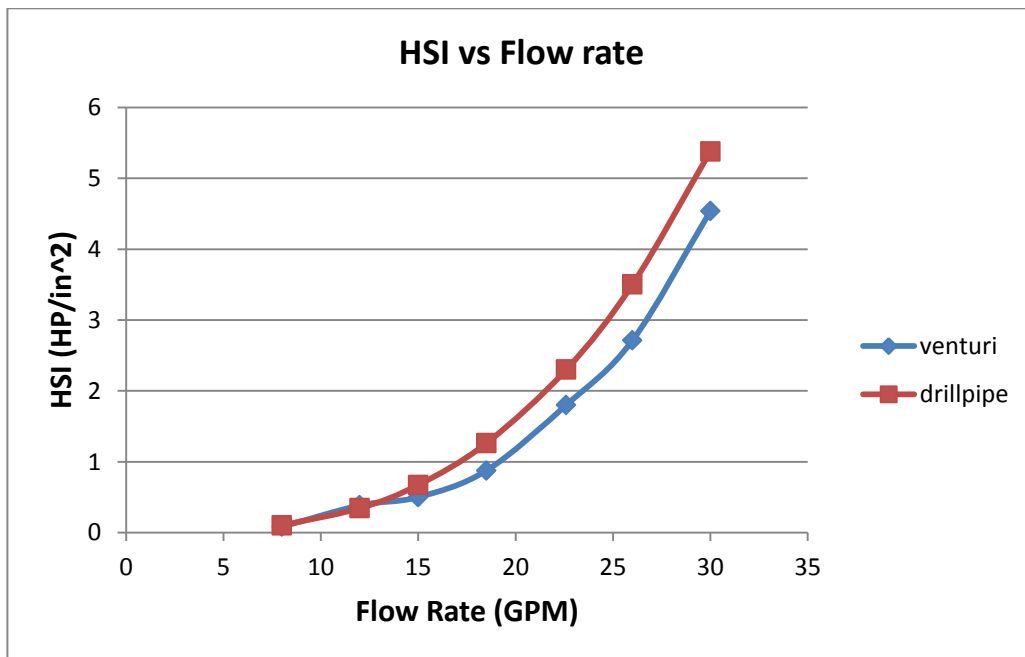


Figure 104. HSI versus Flow rate.

Figure 104 shows that the HSI for drill pipe is higher than HSI calculated for the venturi insert. By increasing the flow rate, pressure losses also increase in the system.

For both the venturi insert and drill pipe, inlet pressure time series in a time span of 2

seconds for each flow level (representing flow rates) are presented in Figures 105 and 106.

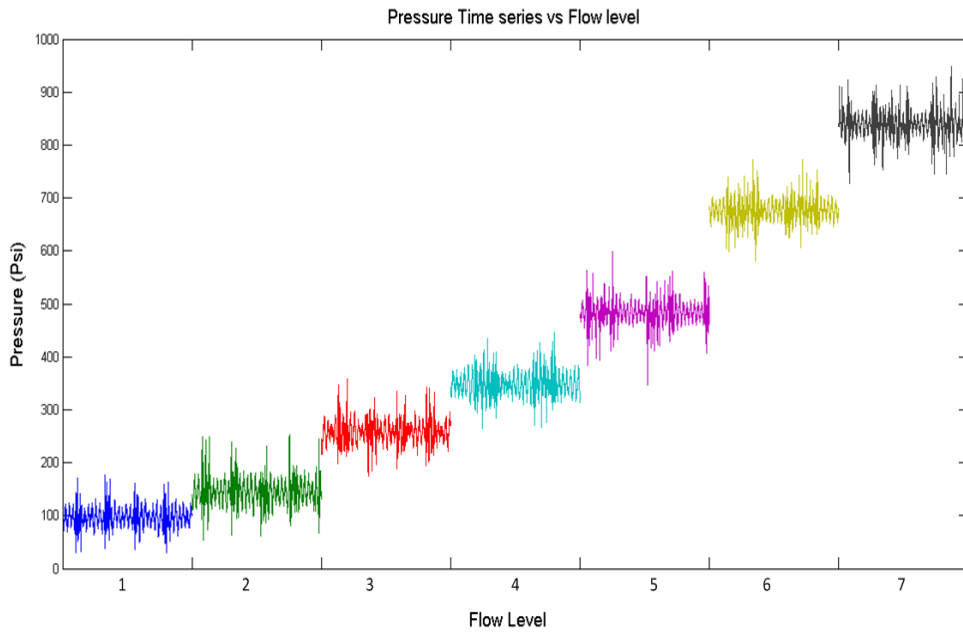


Figure 105. Drill pipe pressure pattern versus flow level.

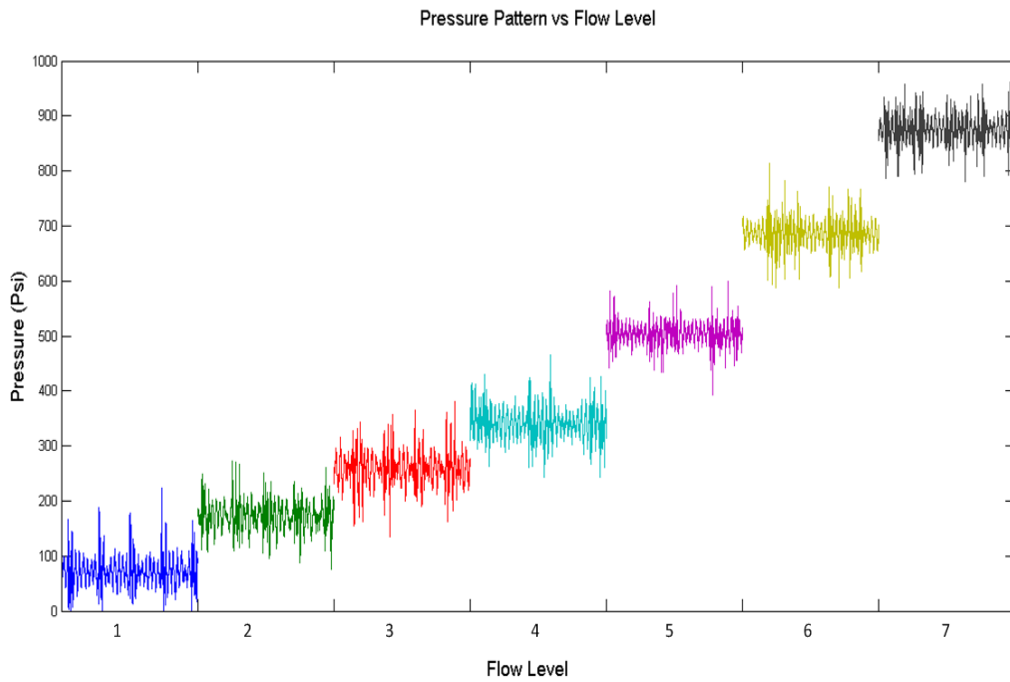


Figure 106. Venturi insert pressure pattern versus flow level.

The comprehensive analysis of the drilling data proved the effect of the compliant element in enhancing the penetration rate and reducing the MSE. This validates the idea that in order to increase the drilling efficiency with tools that generate pressure pulses or mechanical forces, a compliant element is necessary in order to convert these axial forces into displacement. Without the compliant element the forces generated will not act effectively and ROP will not increase. The pulse cavitation tool which was utilizing an 8 mm venturi inside the drill pipe failed to show any improvement with respect to the normal drill pipe.

Low WOB on the drill string even with the compliant element proved that high WOB is required for the compliant element to work efficiently. Low WOB produces low force amplitudes and considering the compliance of the compliant element, the displacement will be minute and hence drilling will not be efficient. Furthermore, the same conclusion derived from the drilling data with high back pressure. These experiments also showed that the displacement of the compliant element was very low.

5.5 Effect of compliance

Prior to the experiments, the effect of the compliant element and relationship between the applied load and the resultant displacement was determined. Figure 107 shows the displacement of the LVDT below the compliant element versus the applied load. The slope of the curve is the compliance of the compliant element in lb/mm. The compliance is 158.5 lb/mm or 700 N/mm.

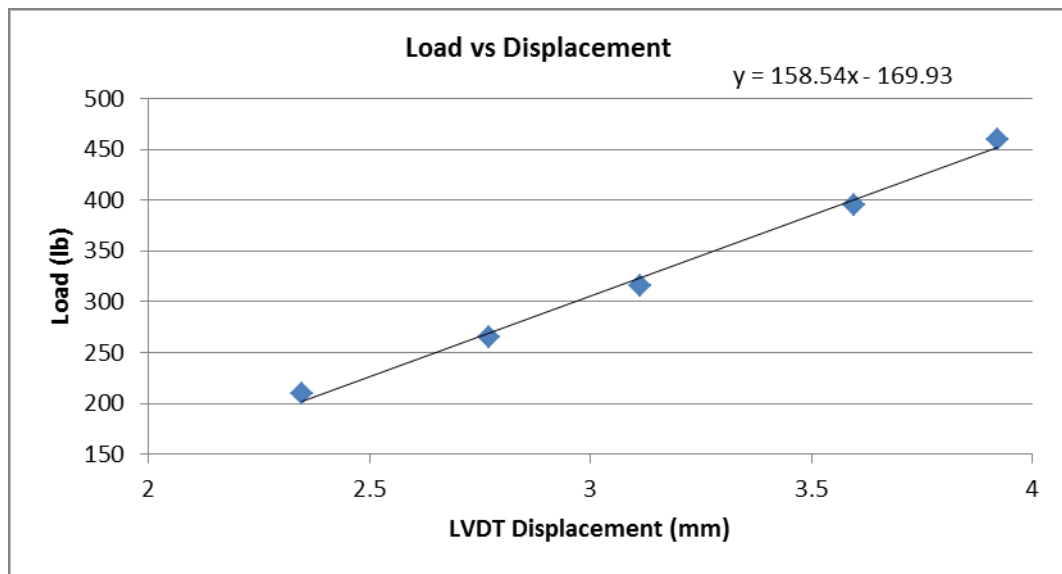


Figure 107. Applied load versus displacement of compliant element.

The typical pattern of the WOB and compliant element displacement is presented in Figure 108. This figure shows that at first the drill string and hence drill bit is off bottom. When the string is lowered down and the drilling process starts, there is a sudden change in both values. The change in displacement as shown in Figure 108 is from 2 mm to 6 mm, which agrees with the WOB data. WOB of 600 lbs. will produce 4 mm displacement if the compliance of the system is 150 lb/mm.

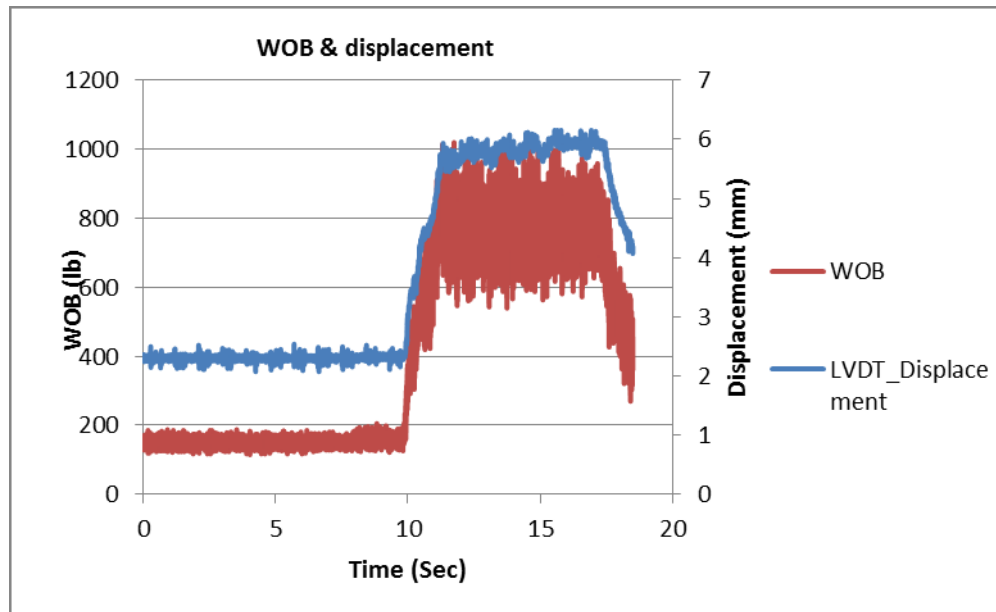


Figure 108. WOB and displacement before and while drilling.

In addition to the planned test, a set of experiments with varying WOBs at the flow rate of 15 USGPM was also done to investigate the effect of compliance in more details. The venturi insert with 4 different WOBs at 15 USGPM with and without compliance was tested. Figures 109 and 110 show the ROP and MSE respectively.

Figures 109 and 110 confirm that the displacement of the compliant element enhances the ROP and reduces the MSE for the same drilling conditions.

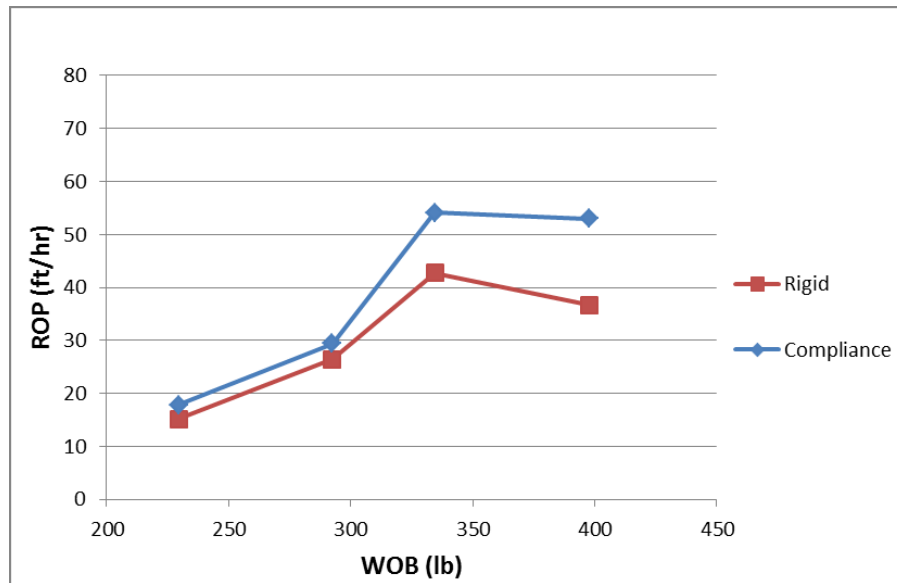


Figure 109. ROP of venturi insert with and without compliance.

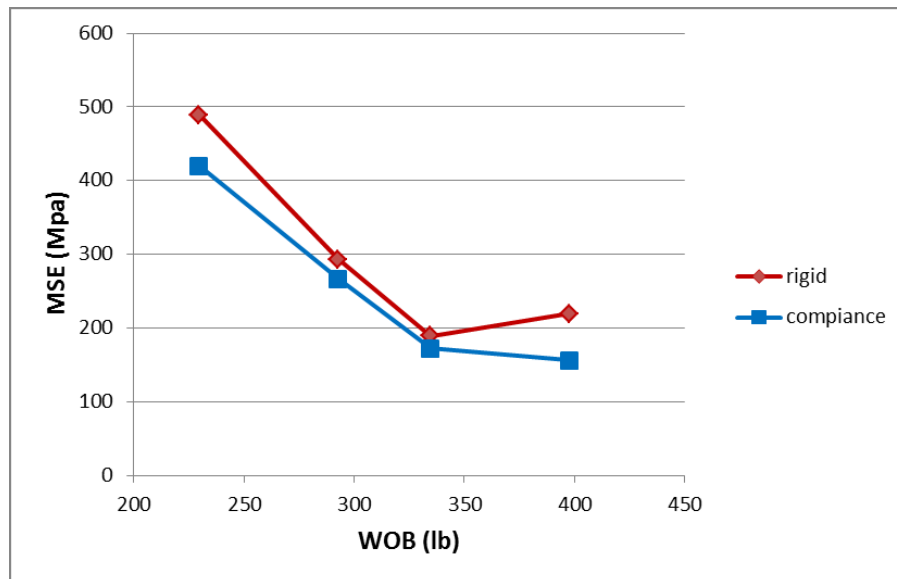


Figure 110. MSE of venturi insert with and without compliance.

Moreover, the times series of WOB for both the scenarios when the venturi was inserted and for smooth drill pipe, show that the average WOB of compliance tests is higher than the average WOB of rigid tests. For drill pipe at 18.5 USGPM and 22.6

USGPM the WOB data with and without compliance is shown in Figures 111 and 112.

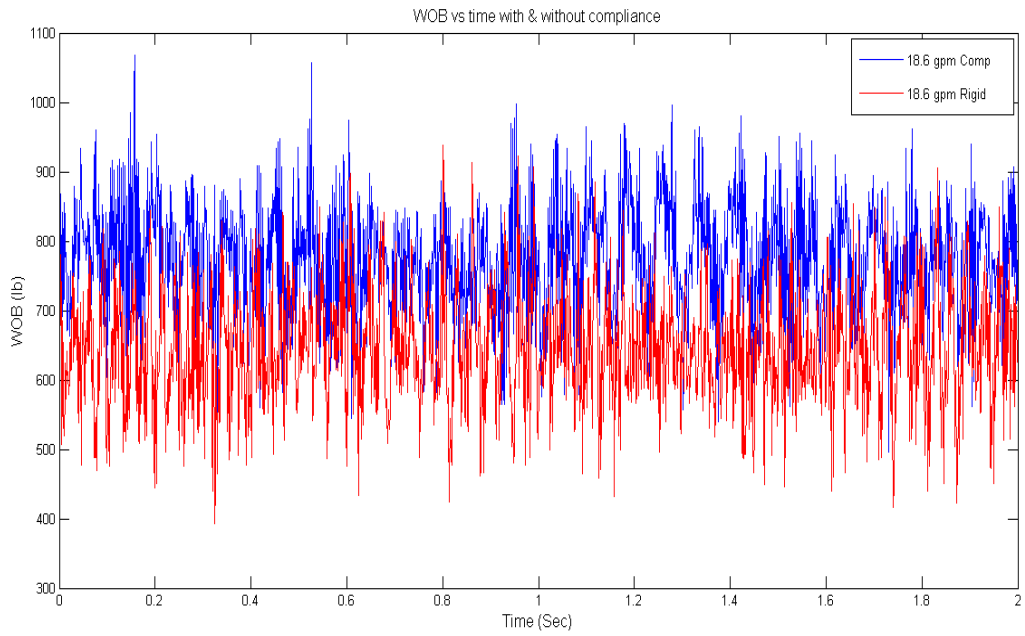


Figure 111. WOB comparison at 18.5 USGPM.

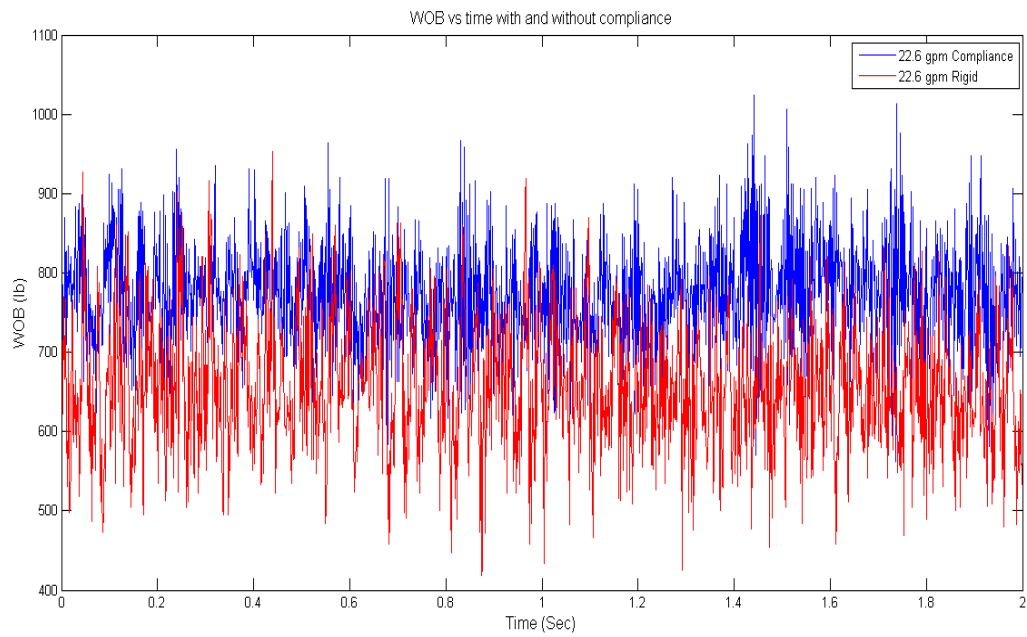


Figure 112. WOB comparison at 22.6 USGPM.

Comparing the displacement and WOB spectral analysis also shows the corresponding results. For displacement at 18.6 USGPM the dominant frequency is 13 Hz while for rigid the vibrations are relatively negligible with no clear dominant frequency. This is shown in Figures 113 and 114.

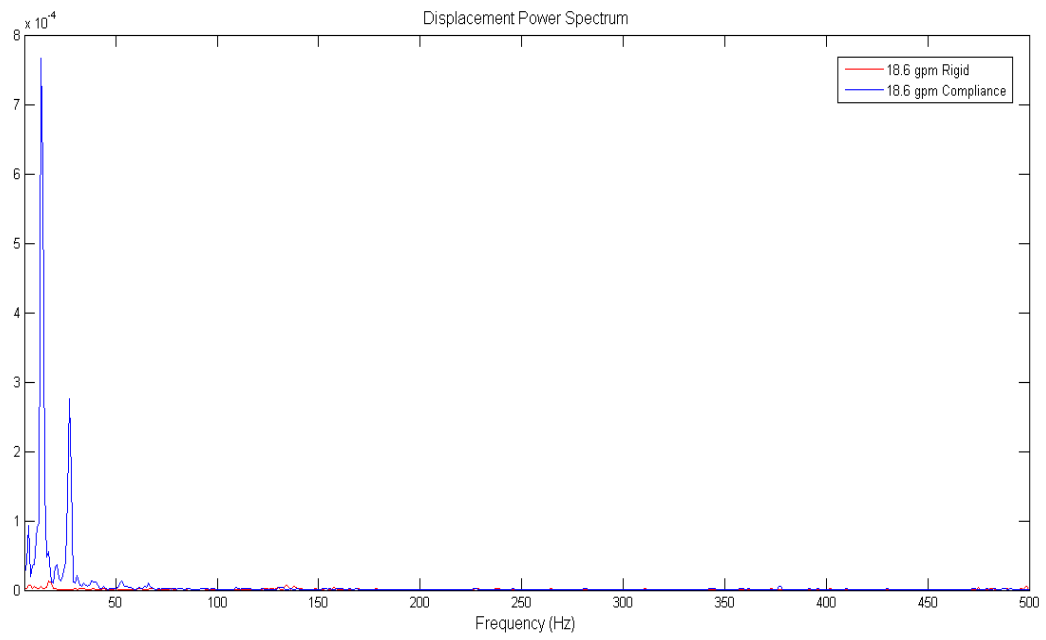


Figure 113. Displacement FFT at 18.6 USGPM with and without compliance.

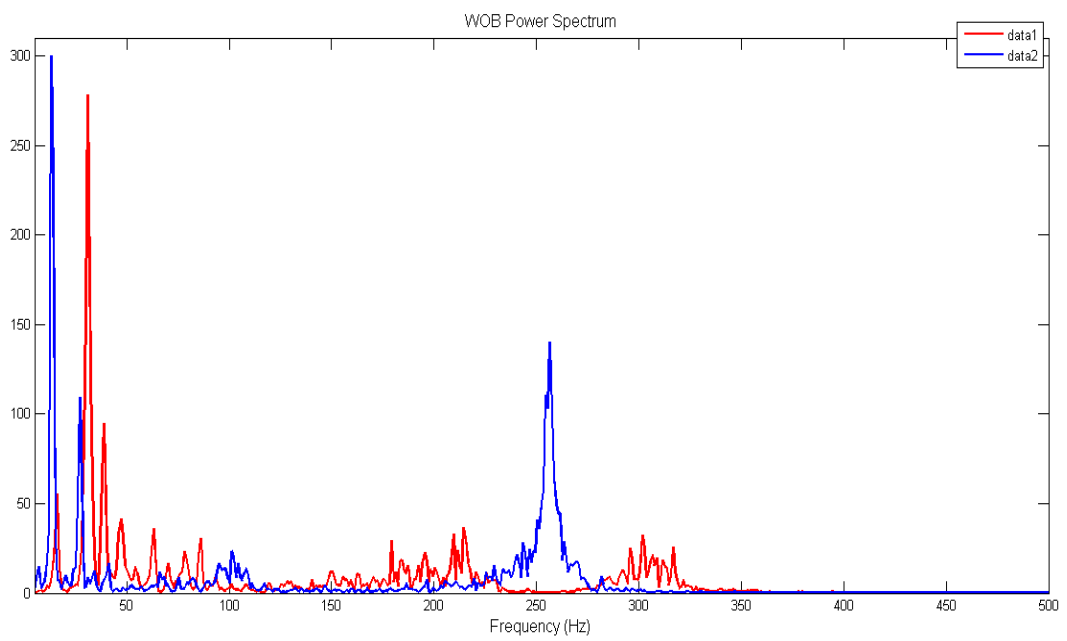


Figure 114. WOB FFT at 18.6 USGPM with and without compliance.

The comparison of the spectral analysis also demonstrated the effect of the compliance. The analysis shows that the equilateral triangular pattern used with rubber mounts has a specific vibration frequency of 13 Hz. For drilling with the drill pipe, the spectral analysis of the WOB and LVDT recording the displacement of the compliant plate are shown in Figures 115 and 116.

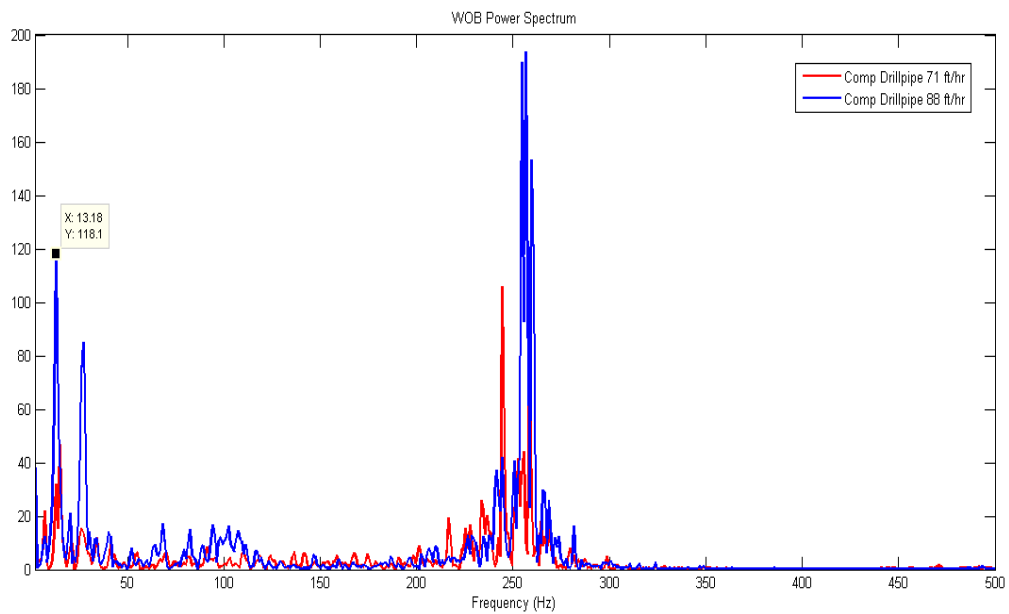


Figure 115. FFT analysis of load of drill pipe at 88 and 71 ft/hr.

The spectral analysis for the venturi insert also shows the increase of the ROP and decrease in MSE is due to the effect of the compliant element displacement. Figures 117 and 118 show the FFT analysis for load and displacement of venturi insert at 58 and 63 ft/hr.

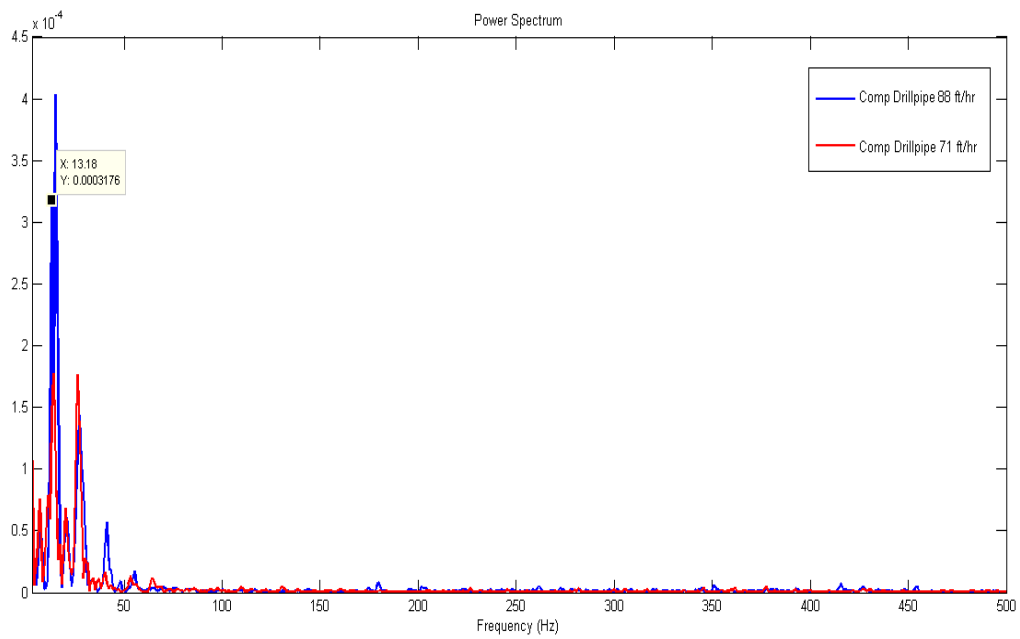


Figure 116. FFT analysis of compliance displacement at 88 and 71 ft/hr.

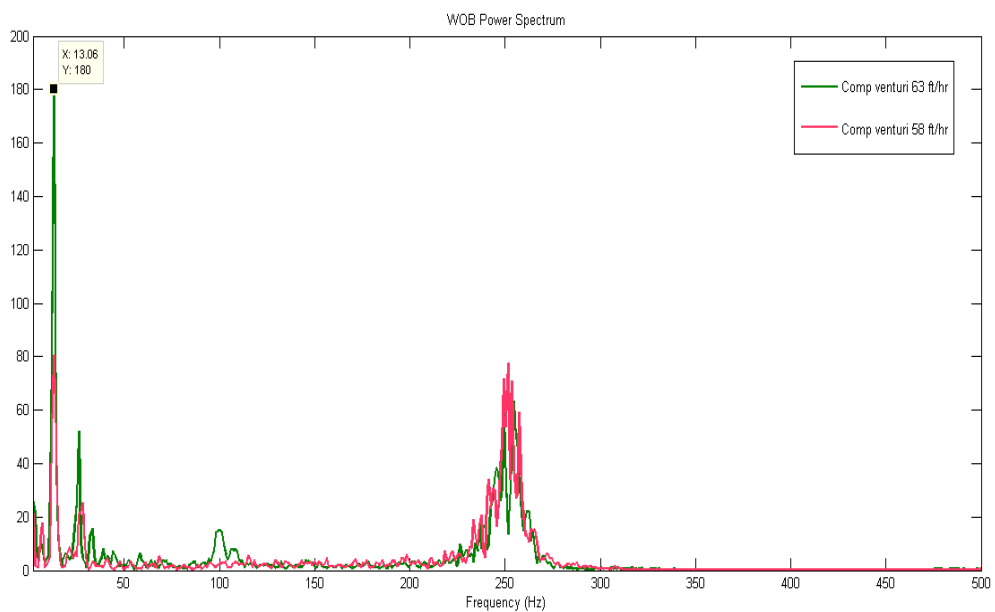


Figure 117. FFT analysis of load of venturi insert at 88 and 71 ft/hr.

Analysis shows that when the vibrations coming from the venturi insert or the drill pipe are around 13 Hz, the natural vibration frequency of the compliant element,

drilling efficiency goes higher. Looking at the spectral analysis shows that at both the low ROP and high ROP tests, the dominant frequency is 13 Hz, but when this frequency is intensified due to the vibration coming from the tools, the compliant element acts more efficiently and drilling is more efficient.

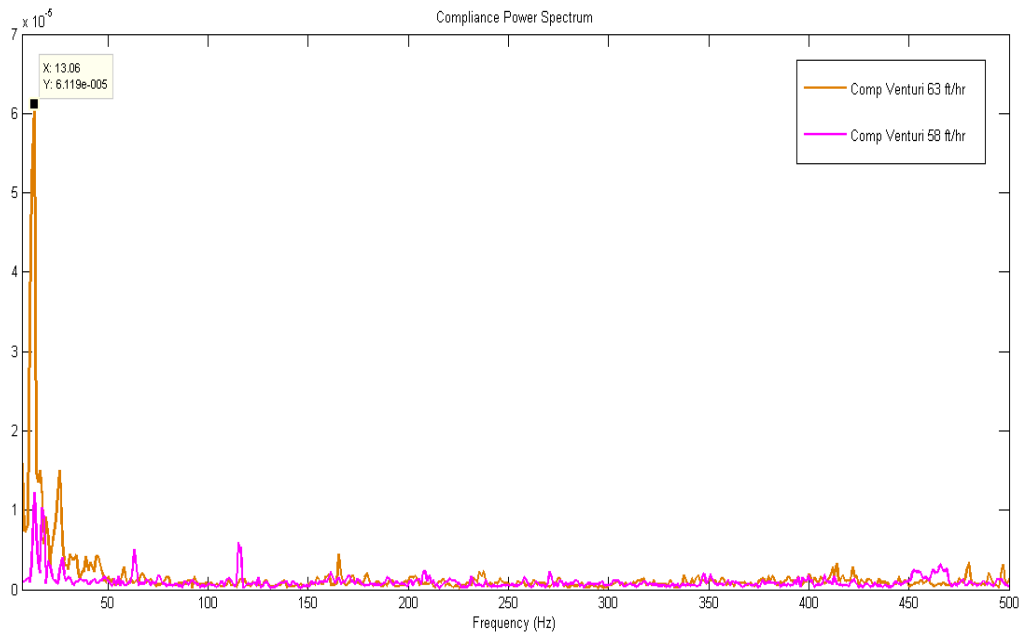


Figure 118. FFT analysis of compliance displacement of venturi insert at 88 and 71 ft/hr.

Analysis of the venturi behavior shows that after 15 USGPM, the cavitation is initiated and pressure pulses are produced. However, only at 22.6 USGPM that the tool is at its optimum performance, ROP goes higher. Comparing the compliance and rigid pattern, however, shows that the increase in drilling efficiency is due to the fact that these vibrations coming from the tool are matching the natural frequency of the compliant element and this is the reason why the tool is working better, while the ROP results for venturi with rigid pattern is lower. Comparing the ROP results of the drill

pipe with venturi, as discussed before, shows that even when the venturi is working at its best, still the drill pipe ROP and MSE values are better.

Since the purpose of this study was to see the effects of cavitation pressure pulses and axial compliance and the research did not intend to reach a specific value for either of the mentioned concepts, the error analysis was not included.

Also, due to the fact that this study was trying to compare the different sets of experiments, the existing error sources were present in both cases and this would not have altered the results of data analysis. Moreover, further investigations on studying the effects of axial compliance and cavitation pressure pulses with different configurations are being conducted and comparing the results and analysis of error sources will be more beneficial after the new experiments are conducted.

6. Conclusions

This chapter will summarize the results of the work done regarding the CFD analysis, tool tests and drilling experiments. The CFD analysis of three different venturis, tool tests regarding the pressure pulses and force vibrations produced, and the efficiency of the pulse cavitation tool in drilling is discussed. Moreover, the effect of the axial compliance in increasing the efficiency of the drilling process for both the drill pipe and drill pipe with venturi insert is discussed.

In Chapter 3, CFD simulations were done in order to investigate the cavitation initiation and behavior inside pulse cavitation prototypes.

In Chapter 4, the preliminary experiments were done in order to investigate the pressure pulses and force vibrations output of the pulse cavitation tool.

In Chapter 5, after conducting various simulations and preliminary flow tests with the prototypes, the effect of a pulse cavitation tool in drilling were sought. Furthermore, the effect of the axial compliance combined with the outputs of the pulse cavitation tool and drill pipe are investigated.

6.1 Summary of pulse cavitation simulations and flow tests

Simulation of the pulse cavitation tool with two different software packages, Flow3D and Autodesk CFD, showed that all the three sizes of venturis produce cavitation. The three different sizes were 4 mm, 8 mm, and 12 mm venturis. In preliminary flow tests, the 12 mm venturi showed better performance, since higher flow rates were available. However, with the 4 mm venturi the back pressure created, due to the parasitic pressure drops throughout the system due to the turbulent flow and the great pressure

drop across the venturi, restricted the flow range. Also the operational range of the pumping system was another factor limiting the flow range. The 12 mm venturi due to the fact that it was producing larger bubble clusters was performing better.

The simulations showed the fixed cavity growth until it became unstable and started to shed bubble clusters. Different features of the simulation software such as pressure pattern at a point during a certain time, pressure pattern along the tool axis in a time frame, cavitation vapor volume fraction, density, etc. validated inception of the cavitation phenomenon.

The physical experiments also recorded the force output of the system which agreed with the calculations done based on theories of fluid jet impacting on a plane. The pressure pulses patterns were in agreement with the simulations. By applying back pressure, intensity of the cavitation was reduced and the tool stopped performing efficiently.

This is also proved with the drilling data, that by applying back pressure, the tool lost its efficiency which makes it less useful to be used in downhole.

6.2 Drilling experiments and axial compliance

The drilling plan was focused on investigating the drilling efficiency sensitivity to both the effects of the cavitation and the axial compliance effect. For this reason, a drill pipe with and without an 8 mm venturi insert was tested. To detect the effect of cavitation, the flow range was chosen from lowest to highest possible achievable flow rate. The same flow range was chosen for both the drill pipe and the drill pipe with venturi insert. The high pressure drop across the venturi reduces the available pressure

drop across the bit, and this reduced the available energy that is needed across the bit. The HSI graphs for both the drill pipe and the drill pipe with venturi insert shows that HSI for drill pipe is higher.

Also, in order to see the effect of the axial compliance, 3 rubber mounts were used to make it possible for the synthetic rock sample held tight in the pressure cell to freely move axially. The compliant element which consists of the rubber mounts was in an equilateral configuration which is the configuration with higher axial displacement amplitude. The compliant element was implemented into the system to convert the force vibrations coming from the tools into displacement. An LVDT was located between the base plate and the compliant plate to record these displacements.

Comparing the drilling results for the drill pipe with venturi insert with and without the compliant element, showed that although at 22.6 USGPM the tool is cavitating at its maximum performance, these vibrations were enhancing the drilling efficiency only when there was compliance in the system.

The spectral analysis of the WOB and the displacement of the compliant plate show that each configuration has its own natural frequency and whenever the vibrations are intensifying these frequencies, the ROP and MSE values are enhanced. Comparing the WOB signals with and without compliance at different flow rates show that the WOB with compliance has a dominant frequency at 13Hz.

Also comparing two different drilling tests with compliance shows that the signals of WOB and compliant displacement have higher energy at the dominant frequency of 13Hz.

The comparison tests done with and without compliance with venturi insert at constant flow rate of 15 USGPM also showed that with compliance ROP and MSE values were enhanced due to the conversion of vibration forces into displacement.

Drilling experiments proved the effect of including a compliant system in order to convert the vibration signals to displacement and hence increase drilling efficiency. However, the compliant section needs to be tuned properly with the vibrations source to work effectively.

Although Cavitation at 22.6 USGPM with compliance had significant increase in drilling efficiency, however, due to the extra pressure drop caused by flow through venturi, the maximum available pressure drop across the bit is far from its optimum and this counteracts the cavitation benefits.

Bibliography

- [1] Center for the Advancement of Process Technology. (2012). *Fossil Fuels to Product*. Retrieved from Kentucky Department of Education Website:
<http://education.ky.gov/CTE/Documents/FossilFuelstoProducts.pdf>
- [2] Bourgoyne, A. T., et al. (1991). *Applied Drilling Engineering*, Richardson, TX: Society of Petroleum Engineers.
- [3] Mitchell, R. F., Miska, S. Z. (2011). *Fundamentals of Drilling Engineering* Richardson, TX: Society of Petroleum Engineers.
- [4] Bizanti, M. S., Blick, E. F. (1983). *Fluid Dynamics of Well-bore Bottom-hole Cleaning*. SPE-12888-MS. Paper Presented at Permian Basin Oil and Gas Recovery Conference, Midland, Texas.
- [5] Bakker T. W., Vladimir I. I. (2002). Cavitator for Effective Well Cleaning. SPE-75352, Paper presented at SPE Coiled Tubing Conference and Exhibition, Houston, Texas.
- [6] Franc, J. P., Michel, J. M. (2005). *Fundamentals of Cavitation*. Boston, MA: Kluwer Academic Publishers, Springer Science + Business Media, Inc.
- [7] Ozonek, J. (2012). *Application of Hydrodynamic Cavitation in Environmental Engineering*, London, UK: Taylor and Francis Group.
- [8] Brennen, C. E. (1995). *Cavitation and Bubble Dynamics*. New York, NY: Oxford University Press.

- [9] Stanley, C. (2012). *Experimental Investigation of Cavitation in a Cylindrical Orifice*. (Doctoral Dissertation). University of New South Wales, Australia.
- [10] Gogate, P. R., Pandit A. B. (2011). *Theoretical and Experimental Sonochemistry Involving Inorganic Systems*. New York, NY: Springer Science + Business Media.
- [11] Moran, M. J., et al. (2011). *Fundamentals of Engineering Thermodynamics*, U.S.A: John Wiley & Sons, Inc.
- [12] Pritchard, P. J. (2011). *Fox and McDonald's Introduction to Fluid Mechanics*. USA: John Wiley & Sons, Inc.
- [13] Hoselton, M. (2003, June 29). *Derivation of Bernoulli's Equation*, Class Lecture for Physics, Trinity Valley School, Fortworth, TX.
- [14] Cengel, Y. A., Cimbala J. M. (2006). *Fluid Mechanics: Fundamentals and Applications*. New York, NY: McGraw-Hill Science Engineering.
- [15] Stanley, C., et al. (2011). Periodic Cavitation Shedding in a Cylindrical Orifice. *Exp Fluids*, 51, 1189–1200.
- [16] Sou, A., Pratama, R. H., Ohashi, R., Sugimura, R. (2011). *Cavitation in a Nozzle with Asymmetric Inflow and its Effects on Liquid Jet*. Paper Presented at the 24th European Conference on Liquid Atomization and Spray Systems, Estoril, Portugal.

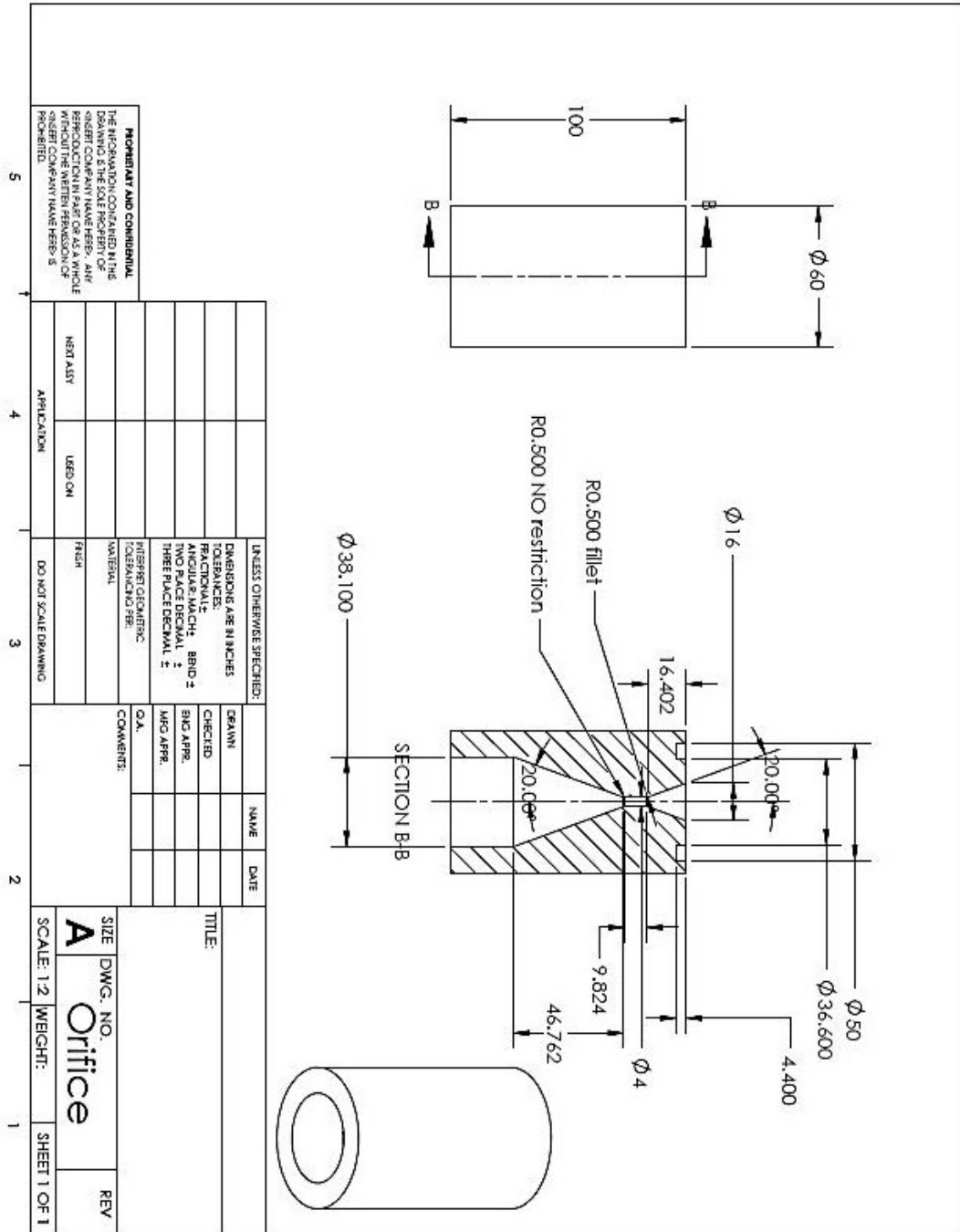
- [17] Raymond, D. W., et al. (2006). Development and Testing of a PDC Bit with Passively-Pulsating Cavitating Nozzles. *Geothermal Resources Council Transactions*, 30, 289-296.
- [18] Johnson, V. E., et al. (1984). *Research and Development of Improved Cavitating Jets for Deep-Hole Drilling* (DE-AC04-76DP00789). Albuquerque, NM: U.S. Department of Energy
- [19] Langeveld, C. J., Adil, F., & Samuel, R. (1992). PDC Bit Dynamics. SPE 23867, Paper Presented at the SPE/IADC Drilling Conference, New Orleans, LA.
- [20] Barnes, H. L. (1956). Cavitation as a Geological Agent. *American Journal of Science*, 254, 49-505.
- [21] Momber, A. W. (2003). Cavitation Damage to Geomaterials in a Flowing System. *Journal of Materials Science*, 38, 747– 757.
- [22] Spray, J. G. (1999). Shocking Rocks by Cavitation and Bubble Implosion. *American Journal of Science* 27: 695-698.
- [23] Grinspan, A. S., Gnanamoorthy R. (2009). Development of a Novel Oil Cavitation Jet Peening System and Cavitation Jet Erosion in Aluminum Alloy, AA 6063-T6. *Journal of Fluids Engineering*, 131, 1-8.
- [24] Versteeg, H. K., Malalasekera, W. (2007). *An Introduction to Computational Fluid Dynamics, The Finite Volume Method*. Essex, England: Pearson Education Limited.

- [25] Bakker, A. (2002). Lecture 6 - Boundary Conditions [PDF]. Retrieved from <http://www.bakker.org/dartmouth06/engs150/06-bound.pdf>
- [26] Eymard, R., et al. (2006). Finite Volume Methods. In P.G. Ciarlet, J.L. Lions (Ed.), *Handbook of Numerical Analysis* (pp. 713-1020). Amsterdam, The Netherlands: Elsevier Science.
- [27] Autodesk CFD Tutorials Retrieved from:
<http://help.autodesk.com/view/ASMECH/2014/ENU/>
- [28] Tu, J. Yeoh, G., Liu, C. (2006). *Computational Fluid Dynamics—A Practical Approach*. Oxford, UK: Butterworth-Heinemann.
- [29] Durgaiyah, D. R. (2004). *Fluid Mechanics and Machinery*. New Delhi, India: New Age International.
- [30] Franc, J. P., Michel, J. M. (1997). Cavitation Erosion Research in France: The State of The Art. *Journal of Marine Science and Technology*, 2, 233-244.
- [31] Khorshidian, H. (2012). *Phenomena Affecting Penetration Mechanisms of Polycrystalline Diamond Compact Bits*. (Master's Thesis). Memorial University of Newfoundland.
- [32] Gharibiyamchi, Y. (2014). *Evaluation and Characterization of Hydraulic Pulsing Drilling Tools and Potential Impacts on Penetration Rate*. (Master's Thesis). Memorial University of Newfoundland.

[33] Mohan, K., Adil, F., & Samuel, R. (2009). Tracking Drilling Efficiency Using Hydro-MSE, SPE 119421, Paper Presented at the SPE/IADC Drilling Conference and Exhibition, Amsterdam, The Netherlands.

Appendix A

4 mm venturi drawing



Appendix B

12 mm venturi drawing

